Development of a needle insertion end effector for robot assistance of ultrasound-guided regional anesthesia

Joshua Morse, B.Eng.

Department of Surgery

Division of Experimental Surgery

Faculty of Medicine

McGill University

Montreal, Quebec, Canada

August 2014

A thesis submitted to McGill University in partial fulfillment of the requirements of the degree of Master of Science

Acknowledgements

I would like to thank:

My supervisor, Dr. Thomas Hemmerling, for his uncompromising support and direction during my time in the Intelligent Technology in Anesthesia Group laboratory. His encouragement for my pursuit of graduate studies is directly responsible for the work presented in this thesis.

Our research associate, Dr. Shantale Cyr, for her assistance and the coordination of the studies over the last four years. I also thank her for her sage advice and for her support of my candidature for medical school.

Our beloved Italian research fellows, Riccardo Taddei, Nora Terrasini, and Marilù Giacalone, for their participation and assistance in the numerous research studies conducted over the last four years. Their many hours preparing studies, collecting and analyzing data, and writing manuscripts laid the groundwork for this thesis.

My fellow engineering graduate students, Mohamad Wehbe and Christophe Philippona, for their constant assistance and input at every stage of this project. Their complementary knowledge brought much needed technical support to this thesis.

Dr. Daniel Funk, for his mentorship, advice, and unceasing support. He is a source of unrelenting inspiration and is responsible for much of my success.

My family, for their continued love and support during my lengthy academic career.

Thank you all.

Table of Contents

List of Tables

List of Figures

Abstract

Ultrasound (US)-guided nerve blocks are routinely used to remove sensation from a particular area of the body. US guidance provides for a more accurate needle placement versus the traditional peripheral nerve stimulator-based approach, leading to an improvement in important outcomes including nerve block efficacy, block duration, and a reduction in the number of accidental intravenous punctures. As robotic devices offer a greater precision and accuracy than is possible with human dexterity, robot assistance could further improve these outcomes. The aim of this study was to develop a needle insertion end effector for US-guided nerve blocks which drives a needle linearly in close proximity to a mounted US probe. The needle insertion end effector was designed in SolidWorks and printed on a Replicator2 3D printer. Linear motion accuracy and precision were tested using three different linear measurement modalities. Mean error in needle placement accuracy was measured to be 0.041 mm with a standard deviation of 0.024 mm. This met the clinically acceptable goal of sub-millimeter accuracy.

Abrégé

Le bloc nerveux échoguidé est une procédure commune en anesthésie permettant la suppression temporaire des sensations dans une zone spécifique du corps. L'échographie permet de placer l'aiguille avec plus de précision, améliorant ainsi l'efficacité et la durée du bloc. Puisque les robots possèdent plus de précision que les êtres humains, l'assistance robotique pourrait encore améliorer la réussite de ces opérations. Le but de cette étude est de développer un système robotique pour guider une aiguille de manière linéaire grâce à la guidance échographique. Ce système robotique a été conçu avec l'aide du logiciel SolidWorks et imprimé en 3D en utilisant l'imprimante 3D Replicator2. Trois outils de mesure linéaire ont été utilisés pour testé la précision du système robotique. L'erreur moyenne de placement de l'aiguille était de 0,041 millimètres avec un écart-type de 0,024 millimètres. Ce niveau de précision a été considéré cliniquement acceptable.

Abbreviations

The abbreviations used throughout this thesis are presented below in Table 1.

Table 1: Abbreviations

Abbreviation	Definition
CT	Computed tomography
DOF	Degrees of freedom
LTA	Linear Testing Apparatus
MRI	Magnetic resonance imaging
PNS	Peripheral nerve stimulator
US	Ultrasound

Introduction

Nerve blocks are a common procedure of regional anesthesia used to temporarily remove sensation from a specific area of the body via the injection of a local anesthetic near or around a nerve. There are two common methods for performing nerve blocks: using a peripheral nerve stimulator or via ultrasound guidance.

Ultrasound guidance is known to improve the efficacy of nerve blocks when compared to peripheral-nerve-stimulator-based techniques for the localization of the nerve (Abrahams, Aziz, Fu, & Horn, 2009). In fact, ultrasound guidance leads to a higher block success rate, shorter procedural times, faster block onset times, as well as longer block durations, while at the same time lowering the risks of unintentional puncture of veins, versus peripheral-nerve-stimulator-based procedures as ultrasound leads to a better nerve localization (Abrahams et al., 2009). Taking this improved nerve localization and needle placement one step further, the use of robot assistance for needle placement could logically afford another increase in these same important clinical outcomes.

Robotic assistance in surgery is an area of active research with the goal of increasing the precision and control available to surgeons. Robotic assistance is used extensively in image-guided surgery procedures, including liver biopsies (Yo Kobayashi et al., 2010; Schreiner et al., 1997; Sun et al., 2006), renal procedures (Bzostek et al., 1997; D Stoianovici, Cadeddu, Demaree, Basile, Taylor, Whitcomb, Sharpe, et al., 1997), prostate biopsy or brachytherapy (Fichtinger et al., 2002; Fichtinger et al., 2008; Fischer

et al., 2008; Krieger et al., 2005; Patriciu et al., 2007; Dan Stoianovici et al., 2007), cholecystostomy (Hong, Dohi, Hashizume, Konishi, & Hata, 2004), neurosurgery (Ken Masamune et al., 1995), and spinal procedures (Corral et al., 2004; Hempel et al., 2003). Robot assistance is ideal for these applications because the robotic systems possess excellent geometric accuracy and very high precision. These same reasons make robot assistance a logical development for regional anesthesia, as nerve blocks require a high degree of accuracy.

A study by Sites *et al*. identified the five most block-quality-compromising behaviors of novice anesthesiologists during the performance of a block (Brian D Sites et al., 2007):

A. Failure to recognize the mal-distribution of local anesthetic
B. Failure to notice the intramuscular needle placement of the needle tip prior to injection
C. Fatigue
D. Failure to correctly correlate the sidedness of the patient with that of the ultrasound image
E. Needle visualization problems

This research aims to address several of these issues.

Operator fatigue (issue C) would be reduced because this robotic system will never fatigue and will allow a block to be performed using only one hand, which would reduce the fatigue of the anesthetist performing the nerve block procedure. The fourth and fifth

issues, related to recognizing the needle in relation to the ultrasound image and the ability to visualize the needle on the ultrasound feed, would be eliminated as the system would know exactly where the needle tip was and automatically and accurately place the needle tip at the target nerve location.

In addition to the increased accuracy and precision afforded by the use of a robot for needle placement, and an increase in safety due to a reduction in the chances of intravenous injection of local anesthetic, this system could have important consequences for regional anesthesia training. In order to investigate this hypothesis, a study was conducted to measure the impact of robot-assistance for learning ultrasound-guided nerve block needle guidance in simulation. This study concluded that robot assistance can lead to faster nerve block needle guidance skill acquisition, as well as decrease inter-subject performance variability and is presented in full in the chapter entitled Article 1 of this thesis (J Morse et al., 2014).

In the Background chapter of this thesis, important background information for regional anesthesia is presented. This chapter is followed by Article 1, a study published in the British Journal of Anesthesia that looks at the impact of robot assistance on learning regional anesthesia skills.

The Literature Review chapter provides an in depth analysis of the current state-of-the-art in needle drivers in the form of a literature review presented as a succinct overview of all of the articles which were found in the literature and their relevance to this thesis.

The System Components chapter presents the technical details for each component that was used in the construction of the needle insertion end effector that was developed for this thesis, as well as the process of selection that was followed for determining which components to include.

The chapter entitled ‘Design of the robotic needle driver’ presents the step-by-step procedure followed in the engineering of the needle insertion end effector, as well as a brief overview of the problems that were encountered during its design. This chapter also presents the derivation of the control equations used to calculate the necessary motor movements to correctly place the needle tip at the target coordinate.

The ‘System Testing’ chapter of this thesis outlines the testing methodology used to evaluate the linear motion accuracy and precision of the robotic needle insertion end effector. This chapter also presents the linear motion testing results.

The thesis ends with the Discussion and Conclusion chapter which outlines the impact that this research could have, discusses the test results, and recommends future work to be done with the system.

Background

This chapter presents background on regional anesthesia, as this thesis presents a needle driver intended for robot assistance in this field. Nerve blocks were first performed by using anatomical landmarks (i.e., physical parts of the anatomy that can be easily seen or felt by the physician, such as bones) as reference points for finding nerves (Zaky, Guirguis, & Nickels, 2013). The results of using anatomical references were not satisfactory, however, and so peripheral nerve stimulators were used in conjunction with them in order to help localize the nerve (Zaky et al., 2013). Problems persisted with the peripheral nerve stimulation approach, including unexplained block failures; these unexplained block failures are now understood through the use of ultrasound guidance (Zaky et al., 2013). Ultrasound guidance allows for an identification of the fascia and an easy verification of the spread of local anesthetic, something that is not possible with nerve stimulation (Zaky et al., 2013). Also, ultrasound guidance has been shown to be superior to nerve stimulation guidance in several important patient outcomes, including higher success rates, longer nerve block duration times, and reduced complications (Abrahams et al., 2009).

There are three steps in the process of performing an ultrasound-guided nerve block: first, the target nerve must be visualized using an ultrasound machine; second, a needle containing local anesthetic must be correctly inserted through the skin and into the target nerve; finally, the local anesthetic must be injected.

The task of correctly inserting the needle through the skin and into the target nerve is not trivial. In fact, it is reported to be one of the greatest problems that anesthesia residents face while learning regional anesthetic techniques (Brian D Sites et al., 2007). To help clinicians in this task, many companies are developing needle visualization enhancement technologies, including Braun Medical (Bethlehem, PA, USA), Pajunk Medical Systems (Tucker, GA, USA), and Havel's Inc. (Cincinnati, OH, USA) (Sviggum, Ahn, Dilger, & Smith, 2013). A study conducted by Sviggum *et al*. determined that clinicians prefer needles that have tips which are more easily identifiable on the ultrasound image (Sviggum et al., 2013).

Article 1

Comparison of success rates, learning curves, and inter-subject performance variability of robot-assisted and manual ultrasound-guided nerve block needle guidance in simulation

J. Morse[1], N. Terrasini[2], M. Wehbe[1], C. Philippona[1], C. Zaouter[2], Shantale Cyr[1 3], T.M. Hemmerling[1 3]

[1] Division of Experimental Surgery, McGill University, Montreal, Canada

[2] Department of Anaesthesia, University of Pisa, Italy

[3] Arnold and Blema Steinberg McGill Medical Simulation Centre, McGill University, Montreal, Canada

Contribution of Authors:

Joshua Morse: Manuscript preparation, study design, study participation, data analysis.

Nora Terrasini: Study participation, data analysis.

Mohamad Wehbe: Study participation.

Christophe Philippona: Study participation.

Cedrick Zaouter: Study participation.

Shantale Cyr: Study design, manuscript editing.

Thomas Hemmerling: Study design, manuscript editing.

Summary

Background

This study focuses on a recently developed robotic nerve block system and its impact on learning regional anaesthesia skills. We compared success rates, learning curves, performance times, and inter-subject performance variability of robot-assisted vs. manual ultrasound-guided nerve block needle guidance. The hypothesis of this study is that robot assistance will result in faster skill acquisition than manual needle guidance.

Methods

Five co-authors with different experience with nerve blocks and the robotic system performed both manual and robot-assisted, ultrasound-guided nerve blocks on 2 different nerves of a nerve phantom. Ten trials were performed for each of the 4 procedures. Time taken to move from a shared starting position till the needle was inserted into the target nerve was defined as the performance time. A successful block was defined as the insertion of the needle into the target nerve. Average performance times were compared using ANOVA. $P < 0.05$ was considered significant. Data presented as mean (standard deviation).

Results

All blocks were successful. There were significant differences in performance times between co-authors to perform the manual blocks, either superficial (P=0.001) or profound (P=0.0001); no statistical difference between co-authors was noted for the

robot-assisted blocks. Linear regression indicated that the average decrease in time between consecutive trials for robot-assisted blocks of 1.8 (1.6) s was significantly (P=0.007) greater than the decrease for manual blocks of 0.3 (0.3) s.

Conclusion

Robot assistance of nerve blocks allows for faster learning of needle guidance over manual positioning and reduces inter-subject performance variability.

Introduction

Robot assistance has been present in surgery for more than a decade, with robots such as the Da Vinci Surgical System (Intuitive Surgical, Inc., Sunnyvale, CA, USA) being commonly used today by surgeons in the fields of gynaecology and urology. The mechanical robots that provide this robot assistance have been shown to provide an increased precision of movements, improve patient outcome (Lau et al., 2012; Willis et al., 2012), and reduce perioperative morbidity (Ramsay et al., 2012).

Studies have demonstrated that surgical, robot-assistance skills are relatively easy to acquire by novices (Brinkman et al., 2013; Hanly et al., 2004). In fact, a study by Brinkman and colleagues in 2013 showed that more than half of the novices achieved expert-level proficiency with a robot assistance system after only 10 operations (Brinkman et al., 2013). Additionally, robot-assisted surgery has been found to help achieve shorter learning curves and better accuracy than manual or laparoscopic surgery (Heemskerk, van Gemert, de Vries, Greve, & Bouvy, 2007; Rashid, Kini, & Ind,

2010). A prospective study of robotic vs. laparoscopic surgery in 2006 concluded that not only does robot assistance in surgery lower the learning curve for both standard tasks and actual operations, but also that prior surgical knowledge (for open or laparoscopic procedures) is not necessary to learn how to perform robotic procedures (Kaul, Shah, & Menon, 2006).

While all of these studies focus on robot assistance in surgery, little research has been done on robot assistance in anaesthesia. This lack of research into robot assistance for anaesthesia is due to an absence of any such systems designed specifically for this field. As several studies have indicated a lowering of the learning curve for robotic vs. manual surgery, a similar trend could be expected for robot-assisted anaesthetic procedures. Having recently developed the first robot-assisted nerve block system (Magellan robotic nerve block system (J. Morse, Wehbe, Taddei, Cyr, & Hemmerling, 2013)) and tested it in patients (Hemmerling et al., 2013), we set out to compare the success and learning rates, performance times, and inter-subject performance variability of ultrasound(US)-guided, robot-assisted vs. US-guided, manual nerve block needle guidance in simulation on a nerve block phantom. The hypothesis of this study is that robot assistance will result in faster nerve block needle guidance skill acquisition than traditional, manual nerve blocks.

Materials and Methods

The Magellan robotic nerve block system used in this study is composed of a Tuohy standard nerve block needle mounted on a robotic arm (JACO robotic arm, Kinova Rehab, Montreal, QC, Canada) that is controlled via a software control centre and joystick. The graphical user interface for the system (the Magellan cockpit) features a view of the US video feed and a camera view of the needle insertion area (visible in Figure 1).

In this study, 5 co-authors (JM, CP, NT, MW, CZ) each performed 4 different US-guided nerve block needle placement procedures on 2 different nerves of an US nerve phantom (Blue Phantom Select Series Peripheral Nerve Block Ultrasound Training Model, Blue Phantom, Redmond, WA, USA) (Figure 2). This phantom features a superficial nerve at a depth of 1 cm and a profound nerve at a depth of 2.5 cm. It is made of a material that provides for realistic US image characteristics of human peripheral nerves and blood vessels. Half of the procedures were manual, while the other half were robot-assisted. Each procedure was repeated for 10 trials by each user and all procedures involved an "out-of-plane" nerve block where the needle is inserted perpendicular to the US beam.

The 4 procedures performed were a manual, US-guided nerve block needle placement of the superficial nerve; a manual, US-guided nerve block needle placement of the profound nerve; a robot-assisted, US-guided nerve block needle placement of the

superficial nerve; and a robot-assisted, US-guided nerve block needle placement of the profound nerve. Refer to Figure 2 for the identification of the superficial and profound nerves.

Each of the 5 co-authors had different experience in performing nerve blocks. One author (CZ) was an anaesthesiologist with less than a year of experience in regional anaesthesia; the other four co-authors were one anaesthesia resident (NT), a PhD candidate with a background in engineering (MW), and 2 undergraduate engineering students (JM, CP) without experience in performing nerve blocks. Experience levels in using the robotic system also differed: only 2 co-authors (JM, MW) had prior experience with the Magellan system, acquired during the engineering development of the system. As this study aimed to compare the success rates, performance time, learning rates, and inter-subject performance variability between robot-assisted and manual, US-guided nerve block needle guidance by novices, the data collected involved the placement of the needle into the nerve and ignored the important steps of properly turning on and using the US machine and probe, properly manoeuvring the US probe to find the target nerve, and identifying the target nerve on the US image: all of these tasks were performed by the senior author (TH) with many years of experience performing regional anaesthesia. The senior author was the only person to manipulate the US machine and probe during all trials and was responsible for indicating when the needle was successfully inserted into the target nerve. Also, he provided a demonstration of

proper handling of a needle for performing a manual, "out-of-plane" US-guided nerve block for each of the 5 co-authors conducting the procedures. This demonstration consisted of an explanation on how to properly hold and manoeuvre the needle, how to position the needle relative to the US probe, an approximate idea of how far from the probe and at what angle to insert the needle in order to correctly target a nerve centred on the US image, as well as how to properly visualize the needle on the US image. This senior author also provided a 5 minute, hands-on demonstration on how to control the robotic system to perform an "out-of-plane" robot-assisted, US-guided nerve block needle placement by demonstrating the controls of the joystick and performing a single successful block. The same demonstrations were made to each author.

The number of successful nerve block needle placements was recorded. A successful nerve block needle placement was defined as an attempt where the needle was inserted into the target nerve. The same starting position was used for each co-author for both robot-assisted and manual procedures. The time from the starting position till the needle was inserted into the target nerve was recorded as the performance time. The number of attempts required to perform the block needle placement was also recorded, where an attempt was defined as the insertion of the needle into the US phantom. Redirects of the needle while inside the phantom were not considered as a new attempt. Inter-subject performance variability was defined as the variance of the average performance times of each author.

Average performance times were compared using analysis of variance (ANOVA) in SPSS (IBM SPSS Statistics, IBM Corporation, Armonk, NY, USA). The performance times were analysed to compute the learning rates by calculating a trend line using linear regression in Excel (Microsoft Excel 2007, Microsoft Corporation, Redmond, WA, USA). The mean number of attempts per trial was compared using a Student t-test in Excel 2007. A *p*-value of less than 0.05 was considered as showing significant difference. Data normalization for mean performance times was made by bounding the data between the minimum and maximum mean times. Data are presented as mean (standard deviation). This was a pilot study to determine what effects robot assistance would have on learning rates of the needle guidance step of the ultrasound-guided nerve block procedure.

Results

All nerve block needle placements were successful for each of the 5 co-authors. The mean times to perform the manual, superficial nerve block needle placements and manual, profound needle placements for all 5 co-authors were 4.38 (3.10) s and 9.60 (12.26) s, respectively. The mean times to perform the robot-assisted, superficial nerve block needle placements and robot-assisted, profound nerve block needle placements for all 5 authors were 26.78 (13.02) s and 24.92 (15.24) s, respectively.

A significant difference in performance times between the 5 co-authors was found for both the manual, superficial nerve block needle placements (P = 0.001) and manual,

profound needle placements (P = 0.0001), while no significant difference in performance time was noted between the 5 co-authors for the robot-assisted procedures (for either the superficial or profound nerve).

The mean times of the 10 trials for the manual, superficial needle placements were 7.08 (6.04) s, 3.51 (1.32) s, 3.34 (0.91) s, 4.82 (0.76) s, and 3.11 (0.84) for JM, CP, NT, MW, and CZ, respectively. The mean times of the 10 trials for the manual, profound trials were 19.4 (23.61) s, 3.74 (0.86) s, 3.74 (1.59) s, 12.11 (4.59) s, and 9.05 (6.77) s, for JM, CP, NT, MW, and CZ, respectively.

The mean times (of 10 trials) for the robot-assisted, superficial needle placements were 23.01 (9.21) s, 22.99 (8.35) s, 26.76 (9.09) s, 27.18 (8.36) s, and 33.96 (22.94) s for JM, CP, NT, MW, and CZ, respectively. Similarly, the mean times for the robot-assisted, profound trials were 17.48 (5.83) s, 20.84 (14.98) s, 28.38 (11.79) s, 33.91 (25.53) s, and 24.00 (5.59) s, for JM, CP, NT, MW, and CZ, respectively.

The aggregate mean number of attempts per trial before succeeding for all 5 authors were 1.06 (0.13), 1.28 (0.30), 1.18 (0.08), and 1.1 (0.07) for the manual superficial, manual profound, robot-assisted superficial, and robot-assisted profound needle placements, respectively (Figure 3). There was no significant statistical difference in the average number of attempts per trial between manual and robot-assisted nerve block needle placements for either the superficial or the profound nerve.

The aggregate mean times for each of the 10 trials for all 5 co-authors are shown in Figure 4 for both the manual and robot-assisted, superficial nerve block needle placements and Figure 5 for both the manual and robot-assisted, profound trials. The equations on these graphs model the rate at which the performance time for the corresponding procedure changed from one trial to the next: a negative slope denotes a decrease in the time to perform a nerve block needle placement for each consecutive trial.

The average decrease in time between consecutive trials for all co-authors for robot-assisted nerve block needle guidance trials was significantly ($P = 0.007$) greater than the decrease seen for the manual procedures at 1.8 (1.6) s versus 0.3 (0.3) s, respectively.

As the performance time ranges between the robot-assisted and manual needle guidance trials differed, the data were also normalized and the trend lines re-calculated. Figure 6 illustrates that the magnitude of the normalized average decrease in time between consecutive trials for the robot-assisted procedures was greater than the manual procedures (for both the raw and normalized data).

Discussion

This study demonstrates that the use of a robot-assisted nerve block system can result in faster nerve block needle guidance skill acquisition. Robot assistance reduces the variability in nerve block needle guidance time between subjects, while maintaining

similar success rates and requiring a similar number of attempts before the needle was successfully placed.

The first forays into robot assistance in anaesthesia involved the use of the da Vinci Surgical System by Tighe and colleagues in 2010 for performing a nerve block in simulation on an US nerve phantom and a simulated fibre optic intubation on an airway trainer mannequin (Tighe, Badiyan, Luria, Boezaart, & Parekattil, 2010; Tighe, Badiyan, Luria, Lampotang, & Parekattil, 2010). Afterwards, specific robot-assistance systems were developed in our lab for both endotracheal intubation and nerve blocks: the Kepler intubation system (Hemmerling, Taddei, et al., 2012; Hemmerling, Wehbe, Zaouter, Taddei, & Morse, 2012) and Magellan robotic nerve block system (Hemmerling et al., 2013). Both of these systems have been used in pilot studies on patients that indicated the feasibility of robot assistance in anaesthesia.

When compared to laparoscopic surgery, robot assistance for prostatectomies has been shown to provide a shorter learning curve and a decrease in the number of mistakes for surgical novices (Rashid et al., 2010). In this study, users learned to perform nerve block needle guidance faster with the robotic system than they did manually. However, similar to the trend between manual and robot-assisted nerve blocks seen in this study, robot-assisted prostatectomies are known to take longer than their open (manual) counterparts (Menon, Tewari, Baize, Guillonneau, & Vallancien, 2002; Tomaszewski et al., 2012). Unlike the surgical operative times that take multiple hours, the nerve block

times are under half a minute whether they are robot-assisted or performed manually, making the difference in time a moot point. The increased time, which is due to the slower speed of the robotic arm, could actually provide for a more accurate and well planned approach of the needle.

This study demonstrates that the use of a robot-assistance system to perform nerve block needle guidance can reduce inter-subject variability for the time required to insert the needle into the target nerve. There is a high variability present in the amount of time it takes for anaesthesiologists to learn how to properly perform an US-guided nerve block (de Oliveira Filho, 2002; de Oliveira Filho et al., 2008). Hypothetically, combining the robot assistance evaluated in this study with automatic US nerve identification could further reduce this variability.

The reduction in variability between the rate of acquisition of the skill of inserting the needle into the target nerve seen in this study is possibly due to the use of a joystick as a control mechanism: while the skill to manipulate a needle and the associated anxiety or stress of inserting it through the skin of a patient may vary from person to person, the ability to understand how to manipulate a joystick may be shared more equally amongst the population.

Another important impact of using robot assistance for performing nerve blocks may be the reduction of fatigue: a study by Sites and colleagues of anaesthesia residents learning regional anaesthesia skills identified fatigue as one of the 5 greatest problems

faced while performing a nerve block (B. D. Sites et al., 2007). An important benefit of robotic systems is that they never fatigue (Moran, 2003) and their use has been shown to reduce operator fatigue (Renda & Vallancien, 2003; "Robotic-assisted minimally invasive surgery for gynecologic and urologic oncology: an evidence-based analysis," 2010): as robot-assistance systems developed for anaesthesia are analogous to their surgical counterparts, they could logically afford this same benefit to anaesthesiologists. There are several limitations to this study. The faster learning rate identified in this study is for only one part of a complicated and multi-stage procedure: the effect that robot assistance would have on the rate of acquisition of all of the necessary skills for performing nerve blocks is not quantifiable from the limited scope of this study. Another limitation of the study is that specific failure criteria, such as descending the needle beyond the nerve and/or entering a blood vessel, were not noted. Also, this study was conducted on a single US phantom and by a small number of people: the use of additional phantoms or cadavers and the inclusion of a greater number of volunteers would provide for a better dataset. Further testing of the Magellan system is planned on cadavers that will include a greater number of participants and will attempt to quantify the difference in learning curves for the entire nerve block procedure between robot-assisted and manual methods using the CUSUM model, a model commonly used for measuring the learning curve of anaesthetic and surgical procedures (Barrington,

Wong, Slater, Ivanusic, & Ovens, 2012; Carabuena, 2013; de Oliveira Filho, 2002; de Oliveira Filho et al., 2008; Jimenez-Rodriguez et al., 2012).

In conclusion, robot assistance decreases inter-subject performance variability and allows for faster learning of needle guidance versus traditional, manually performed nerve blocks.

Funding

No external funding was used for this study.

Declaration of Interests

None.

Figures

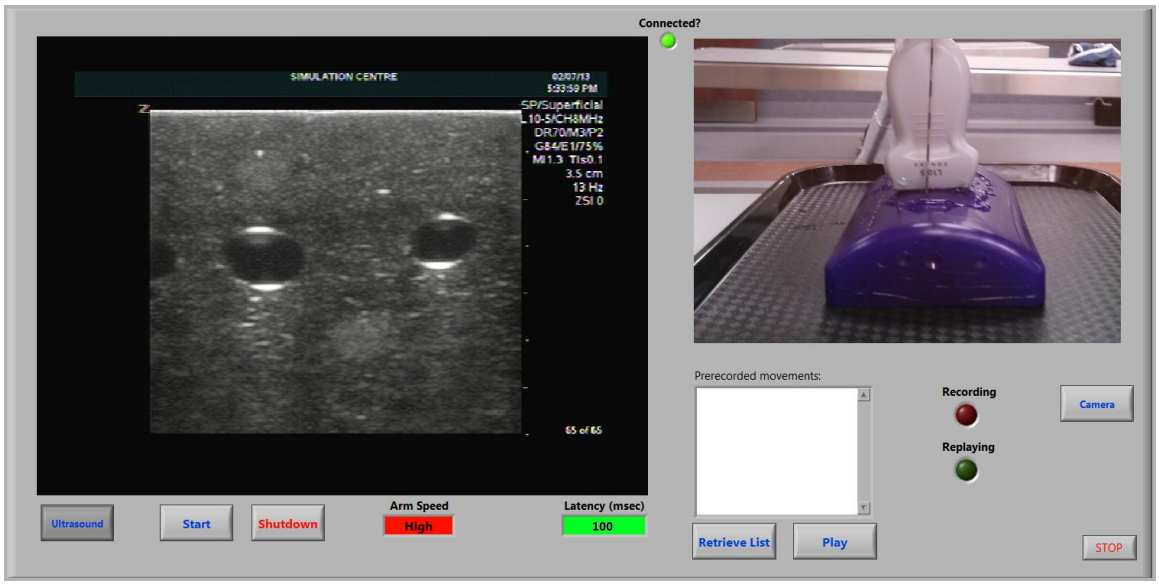

Figure 1: Magellan nerve block system cockpit

The cockpit of the Magellan robotic nerve block system featuring the ultrasound video feed on the left and needle insertion area on the right.

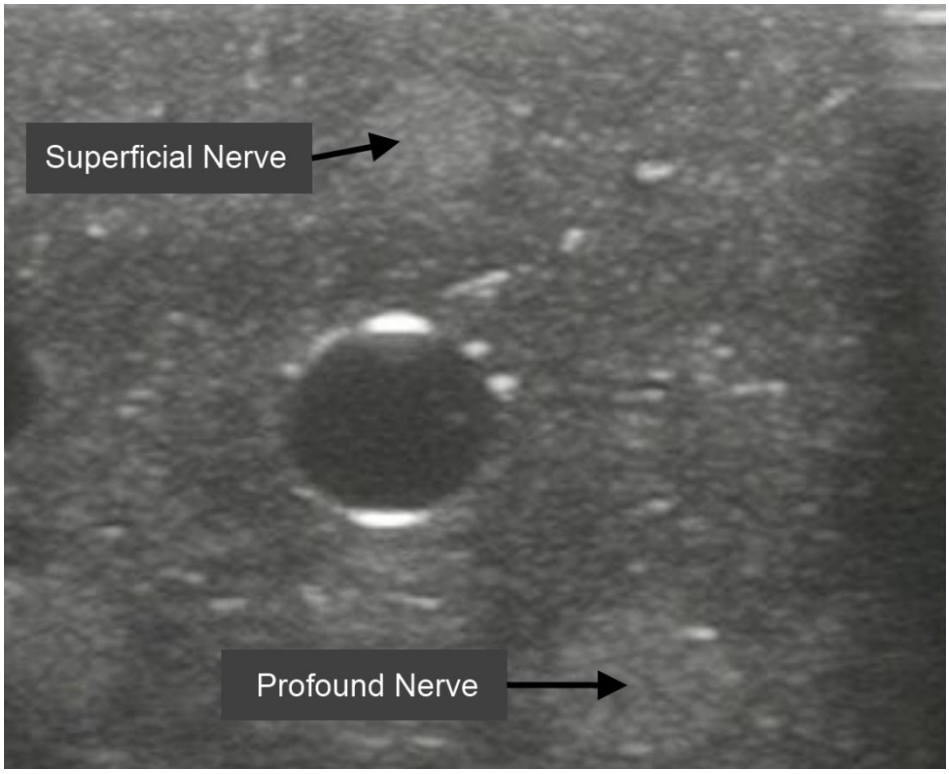

Figure 2: Ultrasound view of the phantom

The ultrasound view of the phantom detailing the two target nerves used in this study.

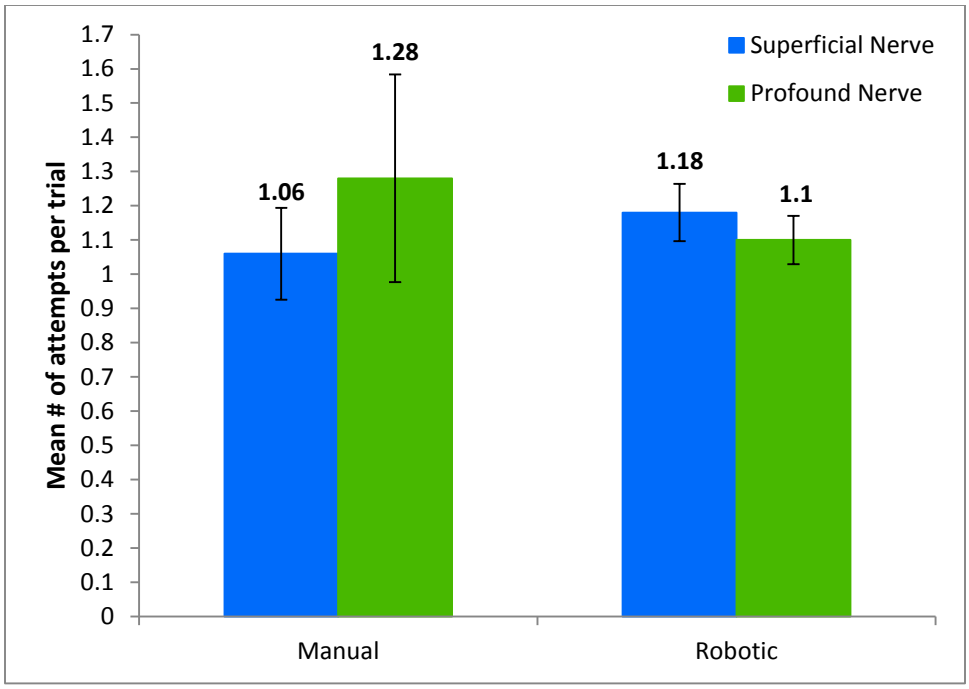

Figure 3: Average number of attempts per trial for each procedure

Average number of attempts per trial for each procedure (error bars represent standard deviation)

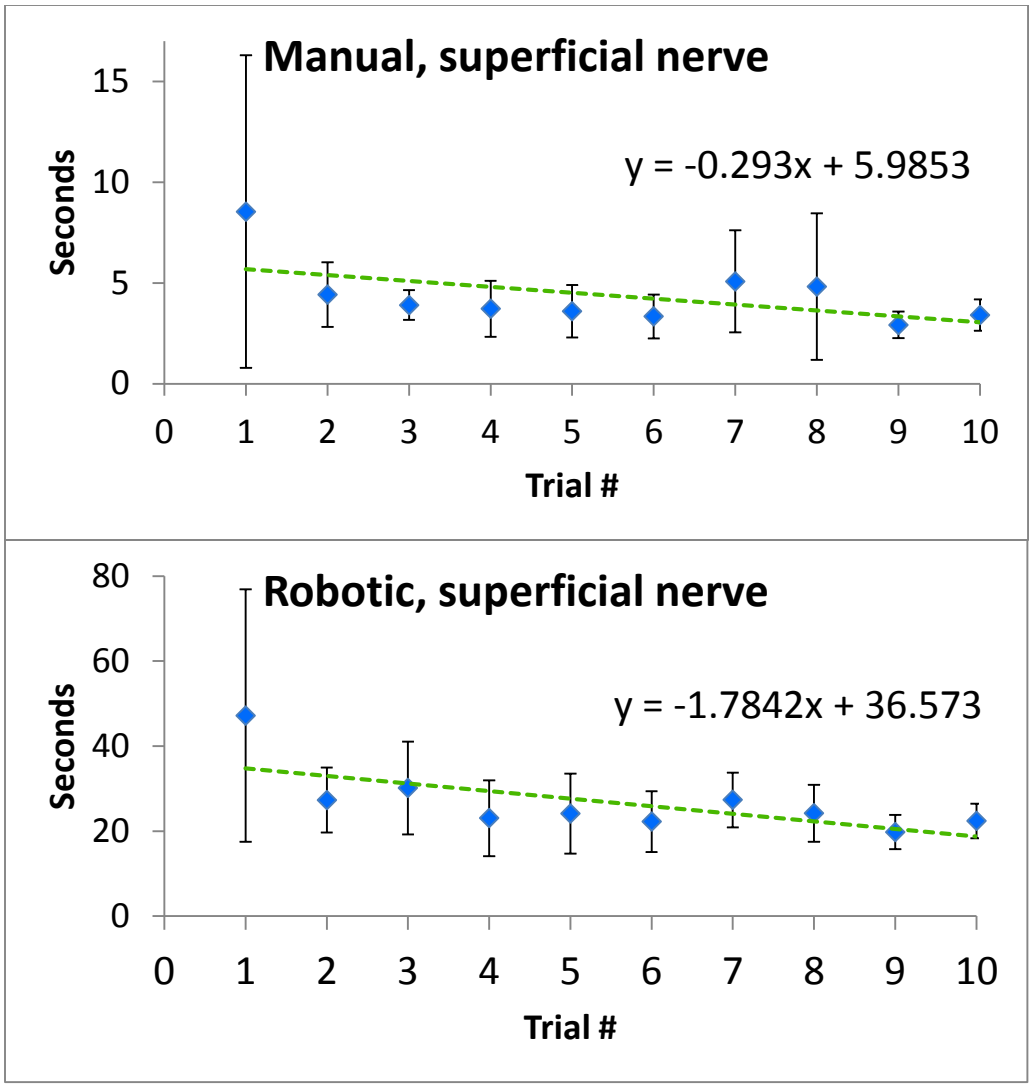

Figure 4: Mean time for each of the 10 trials for the superficial nerves

Mean times for each of the 10 trials for all 5 co-authors (error bars represent standard deviation) for manual nerve block of superficial nerve (top) and robot-assisted nerve block of superficial nerve (bottom). The dotted lines are the trend lines, shown with their corresponding equation.

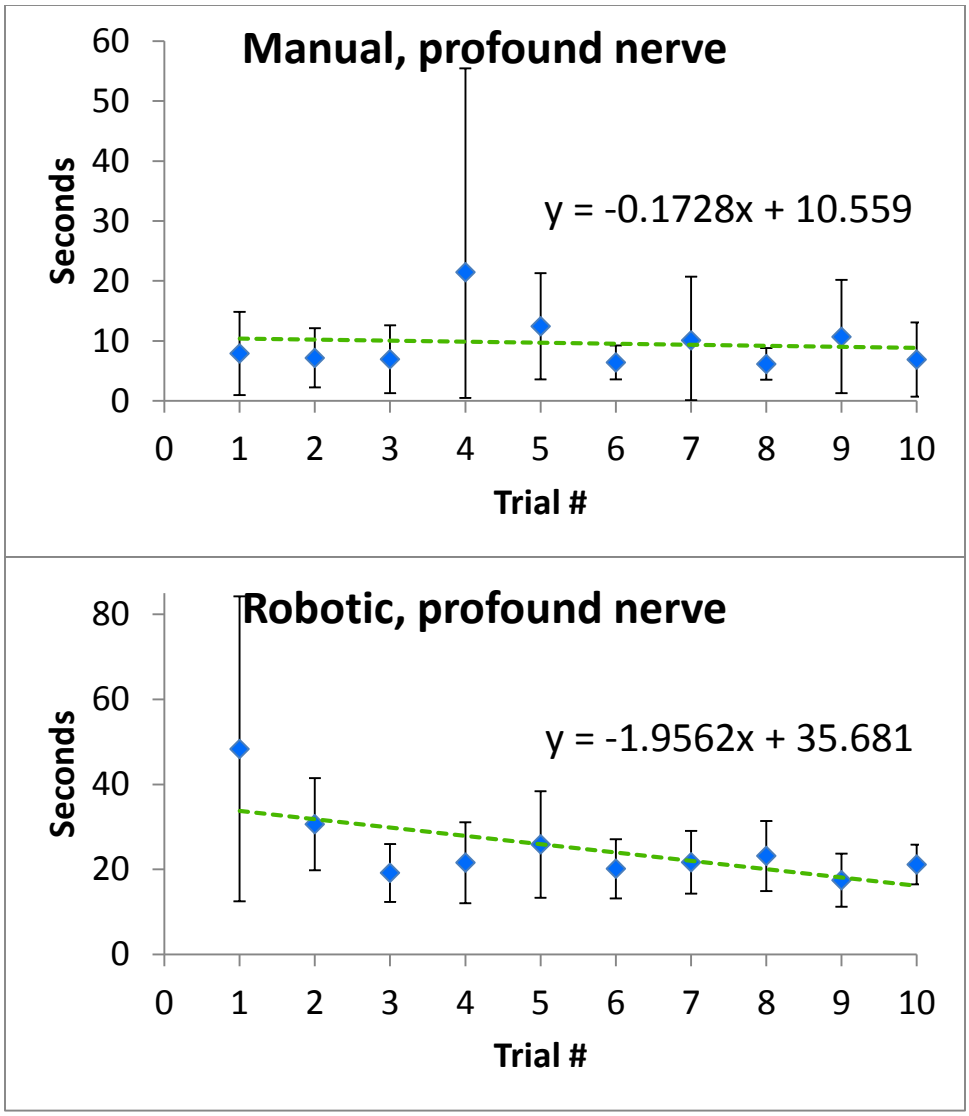

Figure 5: Mean times for each of the 10 trials for the profound nerve

Mean times for each of the 10 trials for all 5 co-authors (error bars represent standard deviation) for manual nerve block of profound nerve (top) and robot-assisted nerve block of profound nerve (bottom). The dotted lines are the trend lines, shown with their corresponding equation.

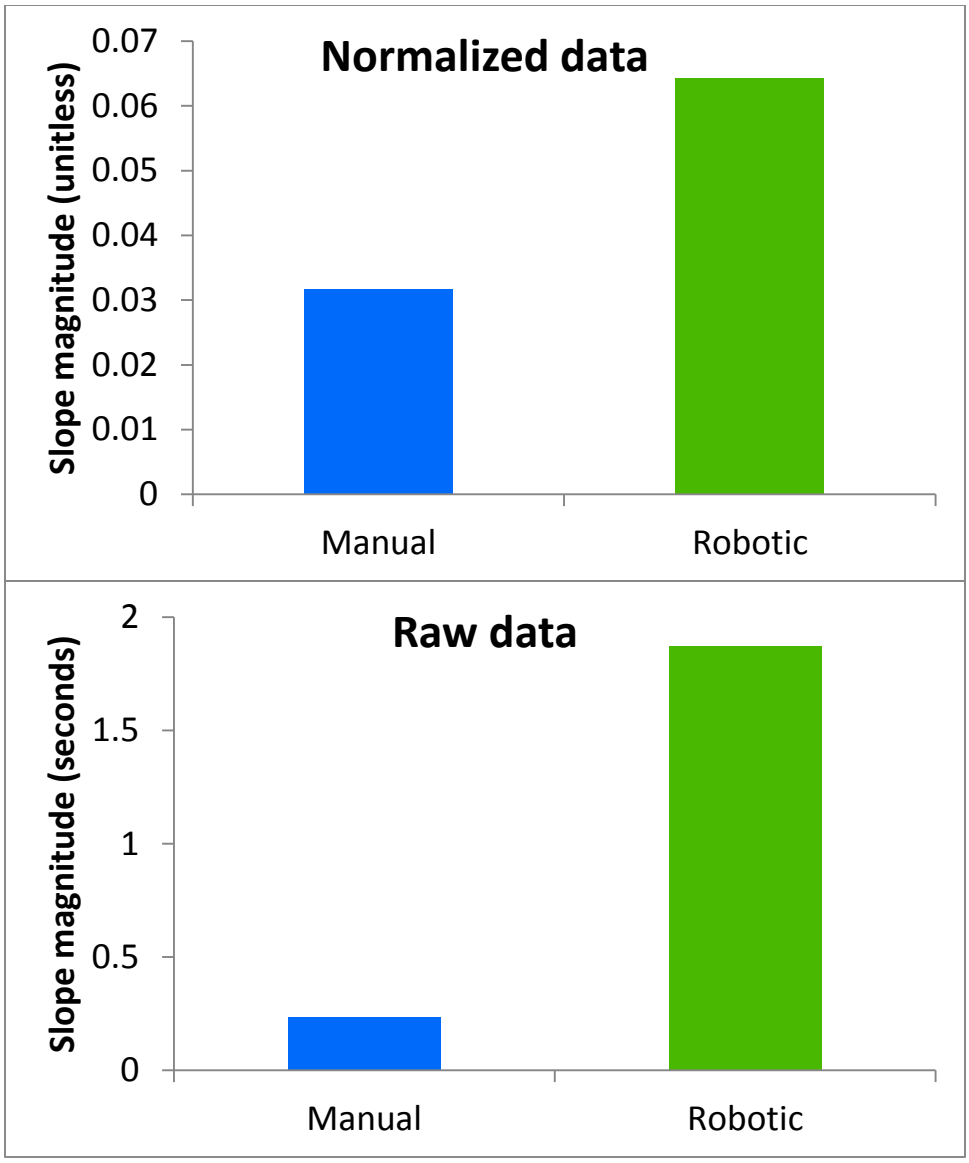

Figure 6: Mean magnitudes of the slopes of trend lines for both manual and robot-assisted trials

Mean magnitudes of the slopes of the linear trend line for manual and robot-assisted nerve block needle guidance trials, both for normalized data (top) and raw data (bottom).

Literature Review

This section gives a detailed overview of the 36 articles analyzed for the literature review of this thesis. The primary data collected included the image modality of the robotic needle driving end effector, any noted safety features, the number of degrees of freedom of the needle insertion mechanism, the motor mechanism powering the needle insertion, and the types of tests performed to determine the accuracy of the needle driving.

For completeness, exclusion criteria are also given for excluded articles.

A robot with improved absolute positioning accuracy for ct guided stereotactic brain surgery (Kwoh, Hou, Jonckheere, & Hayati, 1988)

This robot system does not feature a needle driver; as such it was not included in the review (Kwoh et al., 1988).

A telerobotic assistant for laparoscopic surgery (Taylor et al., 1995)

This robotic system does not feature a needle driver, and thus was excluded from the review (Taylor et al., 1995).

An automated system for precise percutaneous access of the renal collecting system (Bzostek et al., 1997)

This article presents a robotic needle driving system for CT-guided percutaneous renal procedures. This system uses the 3-stage LARS 7-DOF robot developed by IBM. It was developed using a custom 1-DOF injector end effector that used a rail slide mechanism

to maintain alignment and a ball screw and DC motor for driving action. The servos were controlled using a 486 PC (Bzostek et al., 1997).

The accuracy of the system was tested using an *in vitro* model where seven targets were given and the offset measured. The mean error was 0.43 mm and the max error was 0.68 mm (Bzostek et al., 1997).

Next, an *ex vivo* test was performed on two porcine kidneys. Five targets were chosen in the first kidney, eight in the second. 10 out of 12 successes succeeded. The first and third attempts failed. Successes were verified by contrast return through the needle (Bzostek et al., 1997).

Finally, an *in situ* cadaver test was undertaken. 2 of 4 puncture attempts were successful. The first attempt failed due to needle deflection (Bzostek et al., 1997).

No safety features specific to the end effector were described beyond inherently restricted joint velocities (Bzostek et al., 1997).

A system for percutaneous delivery of treatment with a fluoroscopically-guided robot (Schreiner et al., 1997)

This article presents a 1-DOF robotic needle driving system for CT-guided percutaneous liver procedures. The primary driving mechanism of the needle insertion phase consists of a ball screw driven by an encoded DC motor. A solenoid release mechanism is included which allows for modular injectors to be easily attached or removed. The needle is attached using a Luer lock connector (Schreiner et al., 1997).

The specific safety features in this prototype are not listed but the following safety criteria were deemed to be necessary in the final, clinical version (Schreiner et al., 1997):

1. Proper needle shape to minimize injury and deformation of the target organ
2. Rapid and automatic removal of the needle from the body of the patient in the case of a power failure
3. A readily available status update for the surgeon indicating the status of the injector (ready, armed, etc.)

In vitro tests were performed that measured the offset between target and actual coordinates when placing 1/8” diameter aluminum oxide spheres into a bowl of agarose gel. The gel was designed to mimic human tissue. In total, 12 trials were conducted that resulted in a mean error of 0.52 mm with a standard deviation of 0.21 mm (Schreiner et al., 1997).

Urology Robotics work at Johns Hopkins University

In 1997, Stoianovici *et al.* from Johns Hopkins University developed a needle driving mechanism, called the PAKY (Percutaneous Access of the KidneY) needle driver, attached to a 6-DOF passive manipulator arm for performing percutaneous procedures (specifically renal access). This needle driver is constructed of acrylic, has a low radiological profile, and is controlled via a joystick (D Stoianovici, Cadeddu, Demaree, Basile, Taylor, Whitcomb, Sharpe, et al., 1997).

The needle driving friction transmission converts the rotational motion of a drive shaft into the linear translation of the needle (D Stoianovici, Cadeddu, Demaree, Basile, Taylor, Whitcomb, & Kavoussi, 1997). Further work by this team in 1998 used the PAKY needle driving mechanism and a passive mounting arm, but added additional motors to provide 2 DOF of rotation of the needle to allow for robot-assisted needle placement (D Stoianovici, Whitcomb, Anderson, Taylor, & Kavoussi, 1998). A laser was also added to aid the surgeon for loading the needle properly into the needle driving assembly (D Stoianovici et al., 1998). The PAKY needle driver has undergone successful clinical testing (D. Stoianovici, 2001).

A detailed technical description of the PAKY needle driver's friction transmission was presented by Stoianovici *et al.* in 1997 (D Stoianovici, Cadeddu, Demaree, Basile, Taylor, Whitcomb, & Kavoussi, 1997). The transmission is non-backlash and converts the rotational motion of the primary motor into the translational motion of the needle. The main body of the needle driver is made from acrylic to be radio translucent. Needle injection is controlled via a joystick and is powered by a DC motor.

For safety features, the entire system and the needle driver are powered by batteries (eliminating access to high voltages). The operation of the needle is controlled via a push-button switch that is only temporarily on that is mounted on the joystick. The maximum needle insertion depth can be manually controlled by setting the initial position of the needle when mounted on the needle driver. The transmission will also

slip when overloaded, which limits the needle insertion force. This maximum force can be manually controlled via a dial (D Stoianovici, Cadeddu, Demaree, Basile, Taylor, Whitcomb, & Kavoussi, 1997).

The PAKY needle driver's accuracy was tested by in vitro experiments. These experiments took place in a porcine kidney suspended in agarose gel. 70 different attempts were made at completing a circuit between the needle and copper balls of varying diameter placed in either upper or lower poly calyx of the porcine kidney. A completed circuit meant that accurate needle placement occurred. Seven different copper balls, with diameters ranging from 3.0 to 12.5 mm, were used. Successful needle-ball contact was made in all of the 70 attempts (D Stoianovici, Cadeddu, Demaree, Basile, Taylor, Whitcomb, & Kavoussi, 1997).

AcuBot: a robot for radiological interventions (D. Stoianovici et al., 2003)

Stoianovici *et al.*, after using the PAKY robot in clinical tests, designed a revised robot named AcuBot in 2003. This revised robot used a revised PAKY needle driver as the end effector (D. Stoianovici et al., 2003).

The mentioned safety features of the AcuBot, not specific to just the needle driver mechanism, are its high geared axes which minimize both the motors' back-drivability and maximum speeds, gravity-balanced vertical motion which allow the robot to stop during a power outage, and minimal mechanical power (D. Stoianovici et al., 2003).

The control system of the robot features a watchdog process that will shut down the motors in the event of any faults. The watchdog checks for a fault every 100 ms. The robot also has dual encoders for each motor (D. Stoianovici et al., 2003).

The accuracy of the AcuBot system was tested in a cadaver study of perispinal nerve and facet blocks using a 22-gauge needle under biplanar fluoroscopy. Twelve 1-mm diameter metal balls were placed in a cadaver's lumbar spine from L1 to L4 and six nerve and six facet blocks were performed using these targets. The average error in needle placement position from target coordinate was found to be 1.44 mm with a standard deviation of 0.66 mm (D. Stoianovici et al., 2003).

System for robotically assisted prostate biopsy and therapy with intraoperative CT guidance (Fichtinger et al., 2002)

In 2002, Fichtinger *et al.* adapted the idea of a CT-guided needle driving robot presented by Stoianovici *et al.* for guiding the transperineal insertion of a needle into the prostate. This system is controlled via two joysticks and safety control switches. The needle driver mechanism was the same used in the PAKY robot (Fichtinger et al., 2002).

The accuracy of the complete robotic system was tested on phantom models. In the first experiment, a honeydew melon was used as a phantom. The results for this first experiment were an average orientation accuracy of 1° and average error between target and actual needle location of slightly more than 1.5 mm (Fichtinger et al., 2002).

The second involved the use of a commercially available prostate implant training phantom. The third experiment involved the use of a full-body plaster cast with an embedded prostate training model positioned so that the organs represented those of an average male body. Steel balls with a diameter of 2 mm were used as the targets for these two experiments. The average orientation error in the last two experiments was 1.6°, with an average error in position of the needle of 2.5 mm (Fichtinger et al., 2002). The authors noted that the primary cause of needle placement error is an interaction between the needle and the tissue. They recommend that the needle be placed perpendicular to the skin surface before insertion in order to minimize both trans-axial slippage and needle deflection during the insertion procedure. They also noticed that the accuracy of needle placement was related to the speed of the needle during insertion, with lower speeds resulting in higher accuracy (Fichtinger et al., 2002).

A new robotic system for visually controlled percutaneous interventions under CT fluoroscopy (Loser & Navab, 2000)

Another needle driver system developed for percutaneous procedures under CT guidance was developed by Siemens in 2000. This system is also designed to have an end effector with a low radiological profile and is constructed out of carbon fiber and acrylic. This needle driver allows for 2 DOF about the needle insertion area and is designed to be attached to a passive mounting arm. This robotic system can be

controlled manually using a joystick or automatically using an image recognition control scheme (Loser & Navab, 2000).

The accuracy of the complete CT-guidance needle driver system was tested in a phantom consisting of a 2 mm metal ball that was placed approximately 70 mm from the needle tip. Preliminary tests revealed an accuracy of 0.4 mm on average, though these results were not clinically relevant because they were in air and therefore there was no possible deflection of the needle (Loser & Navab, 2000).

Several pig organs were then used as phantoms. For these more clinically relevant tests, automatic alignment was made, and then the needle was manually moved forward in small increments. Intermittent CT fluoroscopy was used after each increment to assess the position of the needle. Over five different series, the average deviation between the target position and the actual needle position was 1.6 mm. The same metal bead size of 2 mm diameter was used in these tests (Loser & Navab, 2000).

This article does not present any particular safety features of the robotic system or the end effector (Loser & Navab, 2000).

System for robotically assisted percutaneous procedures with computed tomography guidance (K. Masamune et al., 2001)

This system uses the same friction transmission system described by Stoianovici *et al.* in 1998 (D Stoianovici et al., 1998). It was modified to have CT fiducial markers (K. Masamune et al., 2001).

Testing indicated an open-air error in placement of less than 1 mm for targets 5-8 cm from the fulcrum point. In a further test using a melon as a phantom with a 2-mm steel ball as a target, an error of 1.04 mm error was found with an orientation accuracy of 0.6° (K. Masamune et al., 2001).

CT-integrated robot for interventional procedures: Preliminary experiment and computer–human interfaces (Yanof et al., 2001)

This article presents a CT-guided robotic system for general percutaneous procedures. This system made use of a commercially available robotic arm and gripper, so it was not customized for the needle insertion procedure (Zaytran Magnum pneumatic gripper and 6-DOF FS-02N robotic arm from Kawasaki Robotics). As the end effector was not designed for needle insertion, it had some flaws such as a limited linear range. To get around this, the robot would release the needle and move back 2 cm in order to re-grip the needle (Yanof et al., 2001).

The combined system was tested in a porcine phantom model. An error of approximately 3 mm was found during the test in the position of the actual needle and the calculated position of the virtual needle, displayed on the CT image. The needle re-grip function was used twice during this test (Yanof et al., 2001).

No specific safety features for either the robot or the end effector were discussed in this article (Yanof et al., 2001).

Virtual remote center of motion control for needle placement robots (Boctor, Webster III, Mathieu, Okamura, & Fichtinger, 2004)

This article made use of the same friction transmission system described by Stoianovici *et al.* in 1997 (D Stoianovici, Cadeddu, Demaree, Basile, Taylor, Whitcomb, & Kavoussi, 1997). No additional safety features or tests of the accuracy of this end effector were noted (Boctor et al., 2004).

Robot control by fluoroscopic guidance for minimally invasive spine procedures (Corral et al., 2004)

This paper uses the AcuBot robot described by Stoianovici *et al.* in 2003 (D. Stoianovici et al., 2003). No further discussion of safety features or testing is provided (Corral et al., 2004).

An ultrasound-driven needle-insertion robot for percutaneous cholecystostomy (Hong et al., 2004)

This article presents a robotic needle driving system for US-guided cholecystostomy. The robot used in this article features a 5-DOF passive arm and a 2-DOF insertion phase. The end effector not only drives the needle, but also holds the US probe. The motor mechanism is a friction transmission, similar to the one described by Stoianovici *et al.* in 1997 (D Stoianovici, Cadeddu, Demaree, Basile, Taylor, Whitcomb, & Kavoussi, 1997). As a friction transmission, slippage is possible but manual insertion depth control is provided.

This system also incorporates an US image guidance algorithm to track intraoperative movement of the gallbladder in order to modify the needle path in real time (Hong et al., 2004).

The complete system was tested on a custom phantom model of the gallbladder that uses a water-filled rubber balloon with a diameter of 3 cm implanted in a graphite/gelatin gel. The case containing the phantom was placed on a linear actuator in order to model the movement of the gallbladder, with a range of motion consistent with respiratory motion. The tracking error of the distance in the actual position of the needle and the calculated, theoretical position was measured at several different speeds of gallbladder movement. The average error was 7.49 mm, with an error of 2.99 mm at a speed of 10 mm/s (Hong et al., 2004).

Additional tests were also performed on a porcine phantom. The error in the needle position in the hepatic portal vein was 1.95 mm (Hong et al., 2004).

A new robotic system for CT-guided percutaneous procedures with haptic feedback (Maurin et al., 2004)

This robotic system was designed for CT-guided percutaneous procedures and seeks to offer haptic feedback to the operator. The device is patient-mounted and has a 5-DOF passive arm and 2-DOF needle driving end effector. Force sensors between these two stages are used to provide force feedback. A parallel manipulator motor mechanism is used for controlling needle insertion (Maurin et al., 2004).

No safety features of the robot or end effector were described, nor were any tests mentioned (Maurin et al., 2004).

A new needle driver for minientry coronary artery bypass (Ohtsuka, Ninomiya, Nonaka, & Maemura, 2004)

This article features a manual needle driver meant for use in a coronary artery bypass surgery. It is not a robot end effector and is thus being excluded from this review (Ohtsuka et al., 2004).

Precision placement of instruments for minimally invasive procedures using a "needle driver" robot (Cleary et al., 2005)

This article describes clinical application of the AcuBot robot described by Stoianovici *et al.* in (D. Stoianovici et al., 2003). It does not describe any new safety features or technical detail of the needle driving end effector (Cleary et al., 2005).

Design of a novel MRI compatible manipulator for image guided prostate interventions (Krieger et al., 2005)

This robotic system is designed as a MRI-compatible transrectal needle manipulator. It has 2-DOF and can be used to manipulate either curved or straight needles. The system uses a lead screw based motor system (Krieger et al., 2005).

The accuracy of the system for needle placement was first tested on *in vivo* canine studies. The maximum needle displacement error for 4 different tests was 2 mm (Krieger et al., 2005).

In vivo clinical accuracy studies were also conducted. The average displacement error was 1.8 mm for 20 clinical trials (Krieger et al., 2005).

The system features manual insertion depth control as a safety feature (Krieger et al., 2005).

A novel end-effector design for robotics in image-guided needle procedures (Sun et al., 2006)

This end effector is designed for liver biopsies and takes into account respiratory muscle movements into the design. A gripper is mounted on the end of a stage featuring multiple DOF. Pneumatics provides the motor mechanism for the needle insertion. The ball and socket joints are manually set to align the needle with the insertion point and then the joints become rigid to drive the needle (Sun et al., 2006).

The system features a manual kill switch to allow for the system to be disabled in the event of an emergency (Sun et al., 2006).

The ability of the system to move in response to respiratory movements was tested in a bovine liver model, but not the accuracy of needle placement (Sun et al., 2006).

Design and validation of a robotic needle positioning system for small animal imaging applications (Waspe, Cakiroglu, Lacefield, & Fenster, 2006)

This article presents a RCM-based needle insertion mechanism with 3-DOF intended for image-guided procedures on small animals. The use of this robotic system on small animals presents unique requirements on the accuracy of the system: the goal for this

robotic system was an error of at most 100 μm. A parallel manipulator provides the motor mechanism for the needle driving end effector (Waspe et al., 2006).

The accuracy of the robotic system was tested in air using 10 targets. The maximum error in positioning in air was measured to be 119 + 18 μm, with an average error in the planes of the roll and pitch axes of the RCM system were 91 + 21 μm and 54 + 12 μm, respectively (Waspe et al., 2006).

Curved multi-tube device for path-error correction in a needle-insertion system (Terayama, Furusho, & Monden, 2007)

This robotic needle driving system was designed to drive a curve-needle and incorporates algorithms for modifying the trajectory of a needle based on real-time error detection. The image guidance is provided by an US probe that is mounted to the needle driver. The system features an outer tube that encompasses the inner, curved needle. Both are driven by separate ball-screw mechanisms. Another ball-screw mechanism allows for the setting of an angle between the axis of the needle and the ultrasound probe, thus the system has 2-DOF for the needle axis; however, a third motor allows for the curving of the needle, providing a total of 3-DOF (Terayama et al., 2007).

The purpose of the curved needle is to allow for the correction of the needle path due to needle deflection at the skin or organ membranes. They define the path error as the distance between the target point and the closest point of the needle trajectory to the

target. The necessary angle to curve the needle to correctly hit the target point is calculated by the software of the system using US image processing (Terayama et al., 2007).

The system was tested by performing 35 trials on a water phantom with a rubber-film membrane with a thickness of 1.0 mm. The average error between the target point and the needle tip, post-correction, was 2.3 ± 2.3 mm for all 35 trials, with a maximum error of 7.5 mm. For trials that limited the positions to those inside a region in the center of the ultrasound image (20 mm wide by 40 mm tall starting at a depth of 50 mm), the mean error was 0.9 ± 1.0 mm with a maximum of 2.6 mm (Terayama et al., 2007).

No specific safety features of the needle insertion phase of the system were mentioned in this article (Terayama et al., 2007).

Robotic assistance for ultrasound-guided prostate brachytherapy (Fichtinger et al., 2008)

This robotic assistance system is designed for manual needle insertion, and thus is excluded from this review (Fichtinger et al., 2008).

Robot-assisted biopsy using ultrasound guidance: initial results from in vitro tests (Kettenbach et al., 2005)

This robotic assistance system is designed for manual needle insertion, and thus this article is excluded from this review (Kettenbach et al., 2005).

MRI-Compatible Pneumatic Robot for Transperineal Prostate Needle Placement (Fischer et al., 2008)

This robotic assistance system is designed for manual needle insertion, and thus this article is excluded from this review (Fischer et al., 2008).

New real-time MR image-guided surgical robotic system for minimally invasive precision surgery (Hashizume et al., 2008)

This robotic system uses forceps as end effectors and thus does not contain a robotic needle insertion phase; thus, this article is excluded from this review (Hashizume et al., 2008).

Robotically assisted needle driver: evaluation of safety release, force profiles, and needle spin in a swine abdominal model (Shah et al., 2008), Does needle rotation improve lesion targeting? (Badaan et al., 2011), and Medical needle steering for lung biopsy: Experimental results in tissue phantoms using a robotic needle driver (Jienan et al., 2008)

This article presents a new robotic needle driver phase to be used with the AcuBot robot (see (D. Stoianovici et al., 2003)). The original AcuBot used the PAKY needle driver (see (D Stoianovici, Cadeddu, Demaree, Basile, Taylor, Whitcomb, & Kavoussi, 1997)). Clinical trials with the AcuBot in spinal nerve blocks identified possible improvements. This needle driver features three such improvements: a mechanism to spin the needle

during insertion, a quick release safety mechanism for the needle, and force sensors (Shah et al., 2008).

The needle rotation mechanism was proposed in order to help lower insertion forces. The quick release safety mechanism can be manually triggered or activated in the event of the force on the needle rising above a certain threshold. The force of the needle is measured by the included force sensors (Shah et al., 2008).

The motor mechanism driving the needle insertion uses rotary joints to create linear motion using a crank, rod, and pin system. This allows for a more compact mechanism compared to traditional translational slider systems as these mechanisms are usually longer than their range of motion, and thus have drivers that are longer than the needle they handle (Badaan et al., 2011).

The quick release mechanism and force sensing of this robotic needle driver was tested, in combination with the AcuBot system, in a swine model using an 18 gauge 15 cm needle. 16 injections were made with the robotic system mounted directly above the insertion area. Incisions were made in the porcine skin to facilitate needle insertion, necessary due to the thicker skin as compared to humans. 16 insertions were performed, 14 in the liver and 2 in the lung. In these tests, the automated quick release mechanism failed 4 times. Two of these failures were due a premature release of the needle before reaching the proper depth; in the other 2 trials, the needle was not released at all. The data obtained also demonstrated that a significant reduction of

required force for accessing the lung or liver of a swine was observed during an insertion when the needle was rotated (Jienan et al., 2008).

Evaluation of efficacy of four laparoscopic needle drivers (Ramani et al., 2008)

This article is about four laparoscopic needle drivers that are used for manual needle insertion during laparoscopic surgeries. As they do not contain robotic end effectors, this article is excluded from this review (Ramani et al., 2008).

Towards a teleoperated needle driver robot with haptic feedback for RFA of breast tumors under continuous MRI (Kokes et al., 2009)

This article presents a 1-DOF robotic needle driver for radiofrequency ablation (RFA) of breast tumors under MRI that features haptic feedback via force sensors. The system makes use of a hydraulic needle driving mechanism, with the non-MRI compatible hydraulic pieces designed to lie outside of the MRI field and transferring the hydraulic pressure via lines to a MRI-compatible hydraulic cylinder within the field (Kokes et al., 2009).

This hydraulic, robotic needle driver was tested for its tumor targeting ability in a phantom breast model under continuous MRI. The test succeeded both in reaching the tumor and in functioning properly during RFA. This test (along with associated MRI image quality and force sensor measurements) verified the system's ability to function properly in the MRI field (Kokes et al., 2009).

Visual vein-finding for robotic IV insertion (Brewer & Salisbury, 2010)

This article does not detail the robotic end effector used, and thus this article is excluded from this review (Brewer & Salisbury, 2010).

The ACUSITT ultrasonic ablator: the first steerable needle with an integrated interventional tool (Burdette et al., 2010)

This article describes a steerable needle and not a robotic needle insertion end effector and thus this article is excluded from this review (Burdette et al., 2010).

Development of an integrated needle insertion system with image guidance and deformation simulation (Yo Kobayashi et al., 2010)

This article presents a 3-DOF robotic needle insertion system that features US image guidance and an organ deformation simulation that allows surgeons to optimize the insertion path of the needle. The driving mechanism for the needle insertion end effector is a “flexible rack” that transfers power from a remote actuator to a ball screw shaft that drives a flange which provides the translation of the needle (Yo Kobayashi et al., 2010). The needle insertion end effector and physical liver model were tested in *an in vivo* experiment on a live porcine liver. A target (inferior vena cava of the liver) was chosen which was clearly visible on the US image. The target was manually found using the US probe, the needle mounted on the end effector was locked in place above the target, and the GUI of the system and the accompanying liver deformation model was used to calculate a path for the needle. This path was then used by the system to insert the needle at 5 mm/s. During the insertion, the forces were measured via integrated force

sensors. The needle successfully reached the target of the liver. The obtained force data also showed that their liver model accurately modeled the forces during needle insertion (Yo Kobayashi et al., 2010).

Toward robotic needle steering in lung biopsy: A tendon-actuated approach (Kratchman, Rahman, Saunders, Swaney, & Webster III, 2011)

This article presents a manually steerable needle for lung biopsy. As it lacks a robotic end effector for needle insertion, this article is excluded from this review (Kratchman et al., 2011).

Design of a robotic tool for percutaneous instrument distal tip repositioning (Walsh, Franklin, Slocum, & Gupta, 2011)

This article presents a 3-DOF robotic end effector that allows for the steering of a needle in a limited volume after insertion. The system is designed to be compatible with CT machines and the translation and rotation are accomplished via stepper motors attached to lead screws. The curving of the needle is accomplished through the translation and rotation of a primary cannula via a guide screw and the translation of an inner stylet (Walsh et al., 2011).

The accuracy of the system was tested in open air position tests where the measured translation and rotation of the needle was measured as compared to the commanded value. Ten trials were taken of the translation of the primary cannula screw-spline with a measured value of 5.01 ± 0.02 mm versus a commanded distance of 5 mm. Ten trials of

the rotation of the cannula screw-spline were also performed, with a command of 5 degrees resulting in an average rotation of 4.97 ± 0.22°. The translation of the stylet was commanded to be 5 mm over 10 trials with an average result of 4.96 ± 0.06 mm. These results demonstrate the sub-millimeter and sub-degree accuracy of the system in open air (Walsh et al., 2011).

Design and Control of a 1-DOF MRI Compatible Pneumatically Actuated Robot with Long Transmission Lines (Yang, Tan, McMillan, Gullapalli, & Desai, 2011)

This article presents a 1-DOF pneumatic actuator designed to drive a needle under MRI guidance. All non-MRI compatible materials are placed in a control room and therefore outside of the MRI field. Long transmission lines are used to transfer the pneumatic pressure to the actuator. As the use of a pneumatic actuator in the presence of the MRI field using long transmission lines brings many technical obstacles to overcome for providing sufficient control for needle placement, three different controllers were designed and tested. The pneumatic actuator contains a force sensor that can be used to provide haptic feedback to the surgeon. They designed a 3D, MRI-compatible fiber-optic force sensor for this purpose. The methodology and design of this force sensor, as well as the three individual controllers, are presented in detail in this article (Yang et al., 2011).

The controllers were first tested in simulation. After this, they were tested in phantom experiments to test for 1-mm placement accuracy under MRI guidance. For these

experiments, each individual controller was commanded in turn to move to 25.4, 50.8, 76.2, and 101.6 mm and then back to 50.8 and 0 mm. Before returning to 0 mm when returning from the 101.6 mm position, the controllers were given step commands of 1 mm from the 50.8-mm location in order to verify if the needle could be accurately placed with a resolution of 1 mm. Force profiles during these experiments demonstrated the effective control of each controller over the entire motion path, while varying degrees of friction were present. The data also demonstrated that the robotic system has an accuracy of less than 1 mm. They determined that one of their controllers provided for a better performance because it had a more uniform response and fewer oscillations (Yang et al., 2011).

No specific safety features of the robotic needle driver were discussed in the article (Yang et al., 2011).

"MRI Stealth" robot for prostate interventions (Dan Stoianovici et al., 2007)

This article presents a novel robotic system designed for transperineal, percutaneous prostate procedures under MRI guidance. The title of this robotic system is MrBot Robot. The system has 5-DOF of freedom for orienting the needle and 1-DOF for needle insertion. The system features very accurate depth control by using two stages for needle insertion: a fixed-depth insertion phase that always extends to the full stroke of this phase. The needle insertion depth is controlled by setting the linear position of

the needle driving phase via a pneumatic piston and linear actuator (Dan Stoianovici et al., 2007).

In meeting the unique needs of developing a robotic system for MRI guidance, this article describes a custom pneumatic motor and fiber-optic encoder that are both MRI compatible. Two of the encoders are used on each motor, providing dual encoder positioning. The custom motor had a linear step of 55 μm and a maximum speed of 16.6 mm/s (Dan Stoianovici et al., 2007).

The system was first tested for positioning accuracy by mounting it on the table of a CNC vertical machining center and using a coordinate measuring probe to record positions. 125 samples were taken with the robot moving 10 mm between each measurement. The normalized position error for these 125 trials was 0.315 ± 0.143 mm. The repeatability of the system was then tested in open air by having the system move to the same position for 317 trials. The normalized error in these trials was 0.076 ± 0.047 mm. Similar repeatability measurements were also taken using an optical tracking system, which had a much lower resolution than the CNC machining center and probe. The measurements with the optical system were taken inside of a 1.5 T MRI scanner and showed a normalized repeatability error of 0.060 ± 0.032 mm, demonstrating that the robotic system is unaffected by the presence of the MRI field. Further image-guided tests and image-based measurements (of even lower resolution than the optical

tracking system) showed mean position errors of 0.72 ± 0.36 mm (Dan Stoianovici et al., 2007).

Image compatibility tests of the system were then taken in X-Ray, CT, Closed and Open MRI, and Ultrasound. The system was shown to be compatible with each imaging modality (Dan Stoianovici et al., 2007).

Magnetic resonance imaging compatible robotic system for fully automated brachytherapy seed placement (Muntener et al., 2006)

This article presents a different end effector for the MrBot robot that was designed to allow for MRI-guided brachytherapy seed placement. This end effector has 4-DOF, 3 used to place the brachytherapy seeds and manipulate the needle and 1-DOF for needle insertion (Muntener et al., 2006).

A safety feature of this system is that the motors will lock on any malfunction, limiting movement during an error to one step of the motor (0.055 mm) (Muntener et al., 2006).

The motion accuracy of the system with the new end effector was tested using an optical tracker in air. The system was commanded to position the needle at 8 extreme points of the intended work area in 20 different series of trials. Similar trials were performed inside of an MRI scanner. For these basic accuracy tests, the average error in position was 0.076 ± 0.035 mm. It was noted that the position error was consistently around 0.050 mm after a warm-up phase of cycles was completed with the system. Inside the MRI field, the average error in position was 0.060 ± 0.032 mm. The increase

in accuracy inside of the MRI field was noted to be due to an unrecorded series of warm-up trials while the robot was adjusted inside of the MRI scanner (Muntener et al., 2006).

The accuracy of the system for brachytherapy was demonstrated using a sausage phantom model for deploying steel balls. For these trials, a sausage was embedded in a clear gel. Stainless steel seeds were then placed at pre-determined positions via completely automated movements of the robotic system. CT scans were then taken to measure the location of the placed seeds. The mean seed placement error was 0.72 ± 0.36 mm over 125 trials (Muntener et al., 2006).

The accuracy of the system was then measured in a 7T MRI scanner using the MRI scanner to calculate the distance moved and compare to the distance commanded. Thirty trials were made and the average error was 0.047 ± 0.053 mm (Muntener et al., 2006).

This robotic end effector and the MrBot robot were further tested in another article that also presented three different image registration methods (Patriciu et al., 2007).

Development of an MRI-compatible needle insertion manipulator for stereotactic neurosurgery (Ken Masamune et al., 1995)

This article describes a 6-DOF robotic system designed for MRI-guided neurosurgery. The needle insertion end effector has 1-DOF. Ultrasonic motors were used because they are made of non-magnetic materials and operate correctly within an MRI field.

Optical rotary decoders were used to provide feedback for closed-loop position control. Non-metallic components were used throughout, with aluminum drive shafts for the primary translational axes (X, Y, and Z axes) and rubber belts for longitudinal movement and needle insertion (Ken Masamune et al., 1995).

The system was initially tested for accuracy in positioning repeatability by commanding the motor to move to a given position 10 times for each axis and recording the error. The largest error was for the Y-axis which had an average positioning accuracy of 51.8 ± 39.7 μm, demonstrating the sub 1 mm accuracy of the system (Ken Masamune et al., 1995).

A phantom study experiment was then conducted to test the operation of the system inside of an MRI field. A watermelon was selected as the phantom as it has similar water content to that of the human head and is well visualized on a MRI image. A seed of the watermelon was selected as the target and the same procedure for determining the insertion path was followed as for manual stereotactic neurosurgery. The robotically driven needle was found to be within 3.3 mm of the target. This large error was described to be mainly due to the limited image resolution of MRI (Ken Masamune et al., 1995).

An MRI-compatible surgical robot for precise radiological interventions (Hempel et al., 2003)

This article presents a robotic system developed for MRI-guided spinal procedures. It features a 1-DOF pneumatic needle insertion mechanism and makes use of ultrasonic motors for actuators. The safety features include dual encoders for each motor and a watchdog process (Hempel et al., 2003).

The system was tested for both MRI-compatibility and needle placement. It was found that the actuators were MRI-compatible if placed at least 0.5 m from the isocenter of the MRI field. For needle placement, tests were made in a porcine phantom to measure both needle deflection and needle accuracy. The authors reported that almost all needle placements were within 1 mm of the target. The data were presented in a scatterplot (Hempel et al., 2003).

Tracking and position control of an MRI-powered needle-insertion robot (Bergeles, Qin, Vartholomeos, & Dupont, 2012) and MRI-powered actuators for robotic interventions (Vartholomeos, Qin, & Dupont, 2011)

This article presents a novel MRI-compatible needle insertion system that makes use of the magnetic field to drive the needle, and is constructed from MRI compatible materials. The prototype was constructed using LEGO components because they are a fast and easy way to prototype MRI-compatible mechanical systems (Bergeles et al., 2012).

The system was tested on both porcine and chicken phantoms. For the chicken phantom, a closed-loop, MRI-powered needle insertion attempt was made into a

chicken breast for a target depth of 10 mm. The closed-loop controller stopped the MRI field, and thus the driving of the needle, when the depth of the needle was 9.95 mm. A swine heart was punctured with the needle driver in order to verify that sufficient force could be created by the MRI field; a sufficient force of 1 N was generated by the MRI field (Vartholomeos et al., 2011).

Development of a needle insertion manipulator for central venous catheterization (Y. Kobayashi et al., 2012)

This article describes a robotic needle insertion mechanism developed for performing ultrasound-guided central venous catheterization. It has 3 DOF, two provided by a parallel-bar RCM module and a one by a ball-screw for needle insertion. No specific safety features were mentioned in the article. The US probe for guidance was mounted directly on the end effector (Y. Kobayashi et al., 2012).

The system was tested for needle accuracy in water. Fifteen different positions and orientations were tested and the maximum error during these placement tests was 0.96 mm, with an average of 0.40 mm. In a puncture experiment, a central-venous-catheterization training phantom was used which confirmed that the robotic system could be manually controlled to accurately place the needle tip within a blood vessel in a single trial (Y. Kobayashi et al., 2012).

Coaxial needle insertion assistant with enhanced force feedback (De Lorenzo, Koseki, De Momi, Chinzei, & Okamura, 2013)

This article presents a system designed to provide haptic feedback for manual needle insertion. As it is not a robotic needle driver, it is being excluded from this review (De Lorenzo et al., 2013).

A novel approach to the design of a needle driver with multiple DOFs for pediatric laparoscopic surgery (Fujii, Sugita, Ishimaru, Iwanaka, & Mitsuishi, 2013)

This article presents a manual needle driver for laparoscopic surgery. As it is not a robotic needle driver, it is being excluded from this review (Fujii et al., 2013).

Design and in vivo evaluation of a robotized needle insertion system for small animals (Goffin et al., 2013)

This article presents a robotic needle insertion system for small animals. However, it does not describe the needle driver and thus this article is excluded from this review (Goffin et al., 2013).

Development of a Needle Driver with Multiple Degrees of Freedom for Neonatal Laparoscopic Surgery (Ishimaru et al., 2013)

This article presents a manual needle driver. As it does not describe a robotic needle insertion system, it is excluded from this review (Ishimaru et al., 2013).

Use of puncture force measurement to investigate the conditions of blood vessel needle insertion (Yo Kobayashi et al., 2013)

This article does not describe a robotic needle driving system and thus is excluded from this review (Yo Kobayashi et al., 2013).

A novel manipulator for percutaneous needle insertion: Design and experimentation (Bassan, Patel, & Moallem, 2009)

This article presents a robotic system for performing percutaneous prostate procedures, specifically brachytherapy. The robotic system can perform translation of the ultrasound probe, as well as insertion and rotation of the needle. The drive mechanism for the robotic needle driver stage makes use of a cable-based differential drive transmission and features several safety features including back-drivable joints and dual encoders for motors (Bassan et al., 2009).

The system's needle placement accuracy was tested first in air and resulted in a maximum error of 1.06 mm. Next, the system's accuracy was tested in agar phantoms at 14 different target points. The average error was 1.45 mm for these trials, with an average insertion depth of 75.78 mm (Bassan et al., 2009).

Development of the needle insertion robot for percutaneous vertebroplasty (Shinya Onogi et al., 2005) and Vertebral robotic puncture for minimally invasive spinal surgery: puncture accuracy evaluation for vertebral model (S Onogi et al., 2009)

This article presents a robotic needle insertion system for performing percutaneous vertebroplasty under CT-guidance. In order to perform this procedure, the needle must puncture cortical bone of the vertebra, necessitating a large insertion force compared to other needle insertion systems. The robot has three stages, two for translational positioning and the third for needle insertion which has 2DOF, one for rotation and one

for linear insertion. The system features a safety feature where the needle driving mechanism is automatically detached from the actuator if a large and unsafe force is applied to the needle (Shinya Onogi et al., 2005).

The robotic system was first tested for needle positioning using optical tracking in air to measure the error between target and actual needle positions. These tests showed sub-1-mm accuracy for all translational movements and sub 0.5 degree accuracy for all orientations. Testing of the safety release mechanism demonstrated that excessive forces would correctly detach the needle. Final testing under CT-guidance of the complete system was made on injection trials in a commercial vertebra model. These trials had an average position error of 0.81 ± 0.40 mm, with an orientation error of 0.20 ± 0.26 degrees (Shinya Onogi et al., 2005).

Further commercial testing was made by the authors in 2009, demonstrating puncture accuracy of 1.46 ± 0.80 mm for needle tip placement and 1.49 ± 0.64 degrees for needle orientation (S Onogi et al., 2009).

A robot-assisted system for minimally invasive spine surgery of percutaneous vertebroplasty based on CT images (Ju, Zhang, An, Pei, & Xing, 2008)

This robotic system aligns the needle robotically for manual insertion. As it does not contain a robotic needle driver, this article is excluded from this review (Ju et al., 2008).

Innomotion for percutaneous image-guided interventions (Melzer et al., 2008)

This article presents a robotic system that is used for robotically aligning a needle for manual insertion. As it does not contain a robotic needle driver, it is excluded from this review (Melzer et al., 2008).

Development of a robotic FD-CT-guided navigation system for needle placement—preliminary accuracy tests (Tovar-Arriaga, Tita, Pedraza-Ortega, Gorrostieta, & Kalender, 2011)

The robotic system presented in this article is excluded from this review because it is used for needle alignment only, needle insertion is made manually (Tovar-Arriaga et al., 2011).

System Components

This section details all of the individual components used in the project. The needle driving end effector is composed of the components listed in Table 2 below.

Component selection process and criteria

The motor, gear, drive spindle, primary encoder, and motor controller were selected because they are manufactured, configured, and calibrated at the factory to function properly together. The secondary encoder was chosen based on its price, size, and compatibility with the motor controller. The motor controller was selected because it supports dual encoders, which will save a considerable amount of software development time. The manufacturer of these components has provided motors for other similar systems, such as the da Vinci Surgical System, which provides some confidence as to the quality and support provided by Maxon Motors.

The motor specifications were chosen carefully after the speed and torque requirements were known. These steps are covered in detail in the Motor selection process section of this thesis.

Table 2: Components of the needle driving end effector

Components	Manufacturer	Part Number	Description
Needle insertion motor	Maxon Motors	118730	RE16 DC motor. 4.5 W. 12 V. Nominal speed of 12000 RPM. Nominal torque of 4.26 mNm.
Gear train and spindle	Maxon Motors	424233	M6 metric spindle with 19:1 gear ratio. Recommended input speed of 12000 rpm.
Primary encoder	Maxon Motors	201940	Rotary encoder with 512 counts per turn.
Secondary encoder	Quantum Devices, Inc.	QD145	Rotary optical encoder with 1024 counts per turn.
Motor controller	Maxon Motors	347717	EPOS2 50/5 digital positioning controller. Supports dual encoders.
Linear rail	Anaheim Automation	CPC-MR3MN	3 mm x 8 cm miniature linear rail.
Linear rail	Misumi Corporation	SSEB6-100	5 mm x 10 cm miniature linear rail.
Secondary motor	Robotis Corporation	Dynamixel AX-18a	DC servo motor. 12V with a no load speed of 97 rpm. 254:1 gear reduction and encoder built in.
Secondary motor controller	Robotis Corporation	USB2Dynamixel	USB controller for AX-18a motor.

Hardware used

The third-party hardware devices that were used to design the needle driving end effector are listed below in Table 3. This table also describes the reason that each hardware device was used.

Table 3: List of third-party hardware used

Device	Manufacturer	Purpose
Replicator 2 3D Printer	MakerBot	3D printer used to print all of the custom plastic components in this project.
NEX-5N Digital Camera	Sony Inc.	Digital camera used for linear motion accuracy and precision testing.
Polaris Optical Tracker	Northern Digital Inc.	Infrared optical tracker used for linear motion accuracy and precision testing.
500-196-30 Absolute AOS Digimatic Caliper	Mitutoyo Corporation	Digital caliper used for linear motion accuracy and precision testing.

Software used

The third-party software programs that were used in the design of this project are listed below in

Table 4. This table also lists the publisher and purpose that each application was used.

Table 4: List of third-party software used

Application	Publisher	Purpose
SolidWorks 2013	Dassault Systemes	3D design software. Used for the design of all 3D models used in this project.
Rhinoceros 5	Robert McNeel & Associates	3D design software. Used to convert the SolidWorks models to STL format so they could be 3D printed.
Makerware 2.3	MakerBot	Printed the STL files of the 3D designs on the MakerBot Replicator 2 3D printer.
EPOS Studio	Maxon Motors	Motor controller development software.
Visual Studio 2010 Professional	Microsoft	Development environment used to create the software control system.
Paint.NET	dotPDN LLC	Image editing software used for analysis of images taken during system testing.
Excel 2013	Microsoft Corporation	Data storage and analysis.
MATLAB 2014a	The Mathworks, Inc.	Data analysis and graphing.

Design of the Robotic Needle Driver

Motor selection process

This section details the selection process for the motor of the robotic needle driver end effector. In order to select the proper motor, the torque, speed, weight, and size requirements must first be determined.

The weight and size requirements are fairly straightforward: the smallest and lightest motor possible is desired that will provide the required torque and speed to perform a peripheral nerve block. These physical dimension requirements are due to the need to mount the motor on a robotic arm in an operating room and in close proximity to an ultrasound probe. The lighter and smaller the motor, the less strain that will be placed on the robotic support system and the easier it will be to incorporate the ultrasound probe support into the needle effector.

According to the book *A Comprehensible Guide to Servo Motor Sizing*, the motor selection has the following five steps (Voss, 2007):

1. Defining the objectives for the motor's motion
2. Defining the mechanical components which meet these motion objectives
3. Estimating the motor's duty cycle (motion profile)
4. Calculation of the load (torque and speed requirements)
5. Selection of the motor which meets the load requirements

The goal of the first step is to outline the motion requirements for the system (Voss, 2007). For this robotic needle driving end effector project, the emphasis of the linear translation of the needle is on the positioning accuracy and repeatability over all other criteria (such as velocity accuracy). The needle will be in a predominantly vertical position when the linear translation of the needle is made. The desired linear speed of the needle is 1 cm/s for the performance of a nerve block. The deepest nerve in the target ultrasound phantom is located approximately 3.5 cm below the surface, so a maximum insertion depth of 5 cm should be sufficient.

The second step is the primary selection of the mechanical components of the system which will meet its motion requirements (Voss, 2007). The possible linear mechanical systems include linear actuators, friction drive transmissions, and lead screws, as outlined in the literature review section of this thesis. In order to focus on simplicity, a lead screw based system will be used.

Motor force and motion profile estimation

The third step in the motor selection process is the estimation of the motor's motion profile (Voss, 2007). An initial literature review for needle insertion force modeling resulted in a first order approximation of 5-7 N for the insertion force, based on two studies that measured maximum needle insertion forces for either the prostate or liver (Abolhassani, Patel, & Moallem, 2007; Okamura, Simone, & O'Leary, 2004).

A trapezoidal motion profile will be estimated for torque calculation purposes, due to the shape of a curve presented in a published figure of needle insertion force into a liver (Abolhassani et al., 2007).

The peak force necessary is expected as the needle punctures the skin, after which the force will be constant equal to the cutting force of the soft tissue. The force required will then go to 0 N when the needle is at rest (for the period of injection). A similar motion profile is expected for the removal of the needle, though with a maximum force of lower magnitude than the initial puncture.

Motor speed estimation

As part of the fourth step of the motor selection process, the motor speed needs to be estimated (Voss, 2007). In order to calculate the desired maximum velocity of the motor, it is first necessary to determine the maximum linear translational speed of the needle. The maximum linear speed of the needle is desired to be around 1 cm/s for the purpose of inserting a needle for the performance of a peripheral nerve block. Assuming a lead screw with a pitch of 1 mm, each revolution of the screw will result in the linear translation of this distance. As a result, 10 revolutions per second are necessary to meet this speed.

Thus, a motor that can rotate at 60*10 = 600 rpm would be capable of achieving the desired translational speed for the needle, assuming no gear is present. Assuming a gear ratio of 20, a speed of 600*20 =12000 rpm would be necessary to move the

spindle nut, and therefore the needle, at a linear speed of 1 cm/s. This is a normal nominal operating speed for small DC electric motors, and thus a good candidate for a first order speed estimate for the motor for the needle driving end effector.

Motor torque estimation

In addition to the motor speed requirements, the torque requirements for the motor must also be estimated as part of the fourth step of the motor selection process (Voss, 2007). The following is a simple formula used to calculate the load torque for a lead screw (Voss, 2007), where F is the maximum force applied by the motor (measured in N), p is the pitch of the lead screw (in m), and e is the efficiency of the lead screw.

$$T = \frac{\mathrm{F} * \mathrm{p}}{2 * \pi * e}$$

For the sake of estimation, we will assume a lead screw pitch of 1 mm/revolution (p = 0.001 m), a maximum force of 7 N (from the Motor force estimation section of this thesis, above), and an efficiency of 40%. These values give a torque estimate of 2.79 mNm, calculation shown below.

$$T = \frac{7\ \mathrm{N} * 0.001\ \mathrm{m}}{2 * \pi * 0.4} = \frac{0.007\ \mathrm{Nm}}{2 * \pi * 0.4} = 0.00279\ \mathrm{Nm} = 2.79\ \mathrm{mNm}$$

This estimate ignores the forces of friction and gravity, but should be sufficient to roughly estimate the motor requirements.

Prototype design process

The first model of the robotic needle end effector was designed as a test base to incorporate the linear rail; motor, gear, and spindle assembly; and optical encoder. This

initial design is shown in Figure 7 below. This design did not include a force sensor as it was designed to test the motor and mechanical assembly features and not provide the full functionality of the complete system.

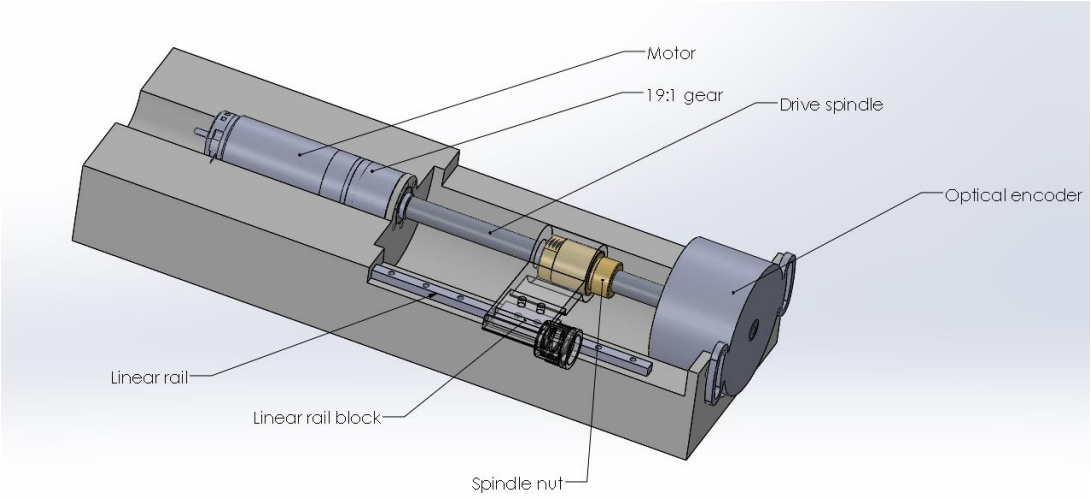

Figure 7: Initial base for primary end effector components

In order to connect the nut of the spindle mechanism to the linear rail and also hold the needle, a simple adapter was designed that featured a male Luer lock, a common locking mechanism found on needles. This adapter design is shown transparent in Figure 7 above and in detail in Figure 8 below.

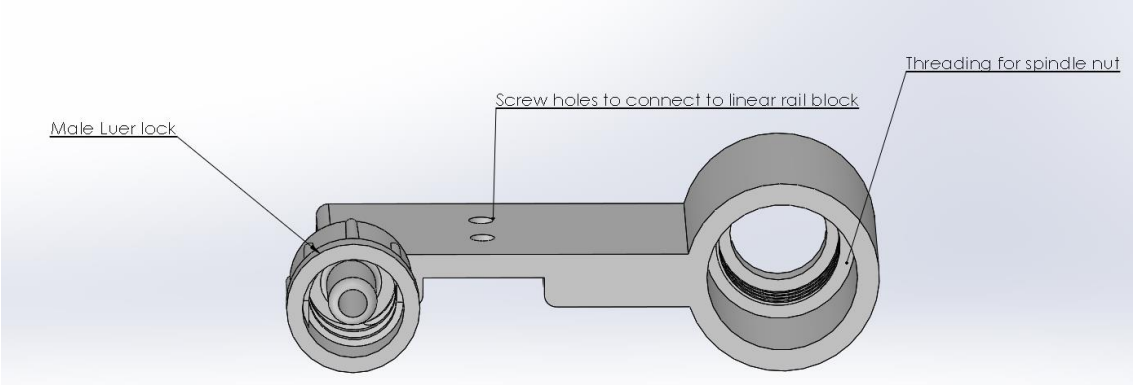

Figure 8: Initial needle connector

This adapter design worked well for converting the rotation of the motor spindle to the linear translation of the needle. However, the Luer lock adapter was quickly identified as a source of a design problem due to the need for a sterile environment. A 19G Tuohy needle with a female Luer lock was originally planned as the needle for this robotic needle insertion end effector. An example of this needle is shown below in Figure 9.

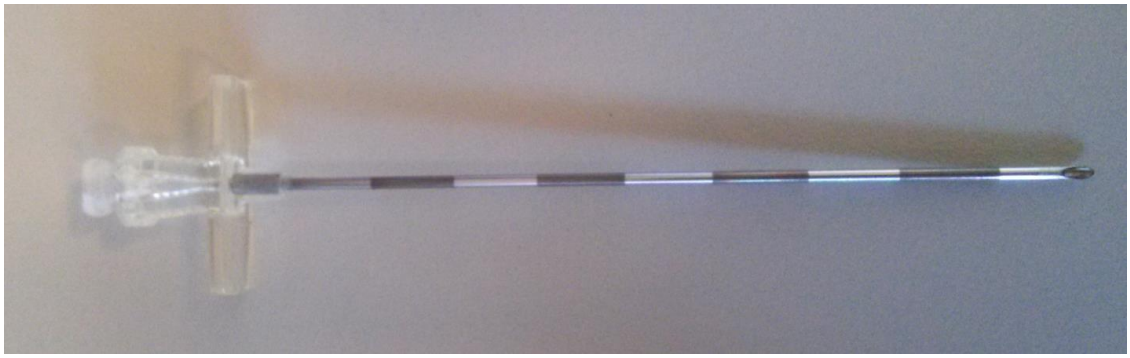

Figure 9: Example of 19G Tuohy needle with female Luer lock

In order to improve the sterility of the system, the intended needle for use was changed to a 9 cm 21G insulated peripheral nerve block needle, an example of which is seen below in Figure 10. This needle type features an integrated IV line, keeping the solution for injection inside the needle at all times.

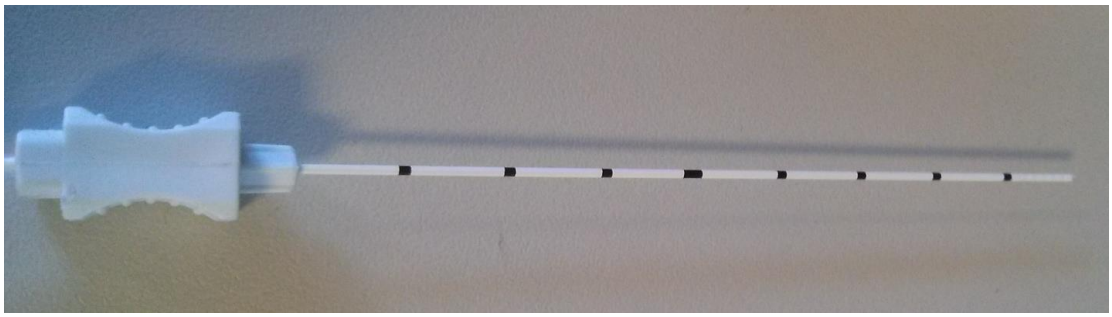

Figure 10: Example of 21G insulated peripheral nerve block needle

As the solution stays inside the IV line and needle, an adapter which holds the needle by the plastic piece but does not touch the needle itself would keep a sterile environment for injection.

A clamping mechanism needed to be designed for this needle, as the plastic connector was designed to be held by hand and was not of a standard type. The size of the connector was measured by hand and a clamping mechanism was proposed that would hold the needle by this plastic piece and not come in contact with the needle itself. An image of a 3D print of this initial clamp mechanism for this needle type is shown below in Figure 11. The plastic sheath of the needle can be removed before the injection takes place, helping to preserve the sterility of the procedure.

Figure 11: Initial clamp design for 21G insulated peripheral nerve block needle

At this point, a design change was made to move the optical encoder from the far end of the motor spindle to be placed and moved along with the spindle nut. This would add additional mass to the spindle nut and help stabilize the drive spindle as it rotates. The linear rail would also be moved to be placed directly along the spindle axis.

To this aim, the design of a new connector piece was made to translate the rotational movement of the nut into the translational movement of the needle that will also support the large optical encoder. A prototype piece to test the sizing and hole layout was designed and printed. This initial design is illustrated below in Figure 12.

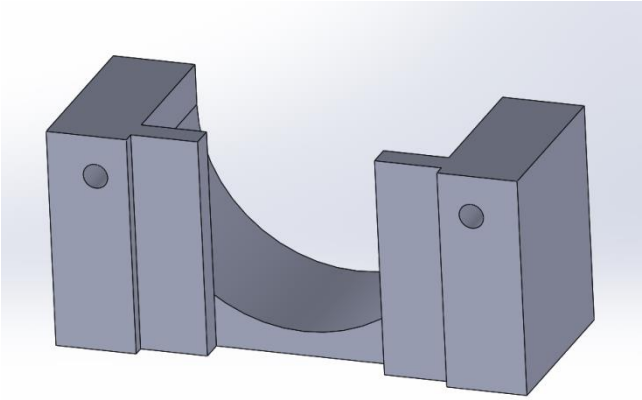

Figure 12: Initial design of mount for optical encoder

This design was 3D printed at this stage in order to verify the proper sizing of the receptacle area for the encoder and also the proper alignment of the screw holes for connecting the encoder. The results are shown below in Figure 13.

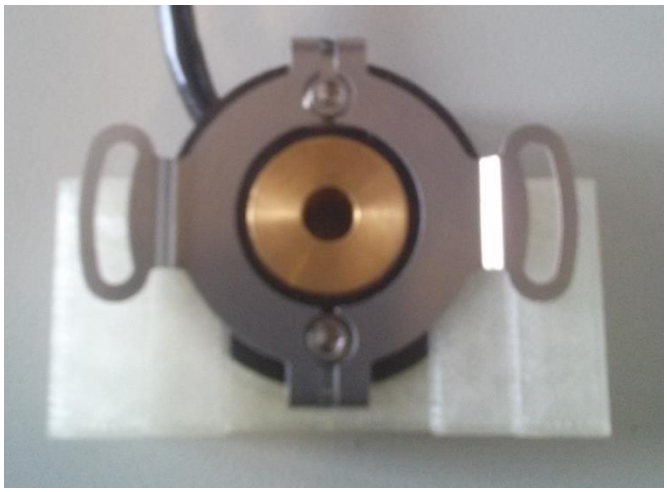

Figure 13: Initial 3D print of mount for optical encoder, shown with encoder

The next step was to expand this design to include holes for mounting this piece to the block of the linear rail, as well as a connector for both the spindle nut and needle. The concept for this piece is illustrated below in Figure 14.

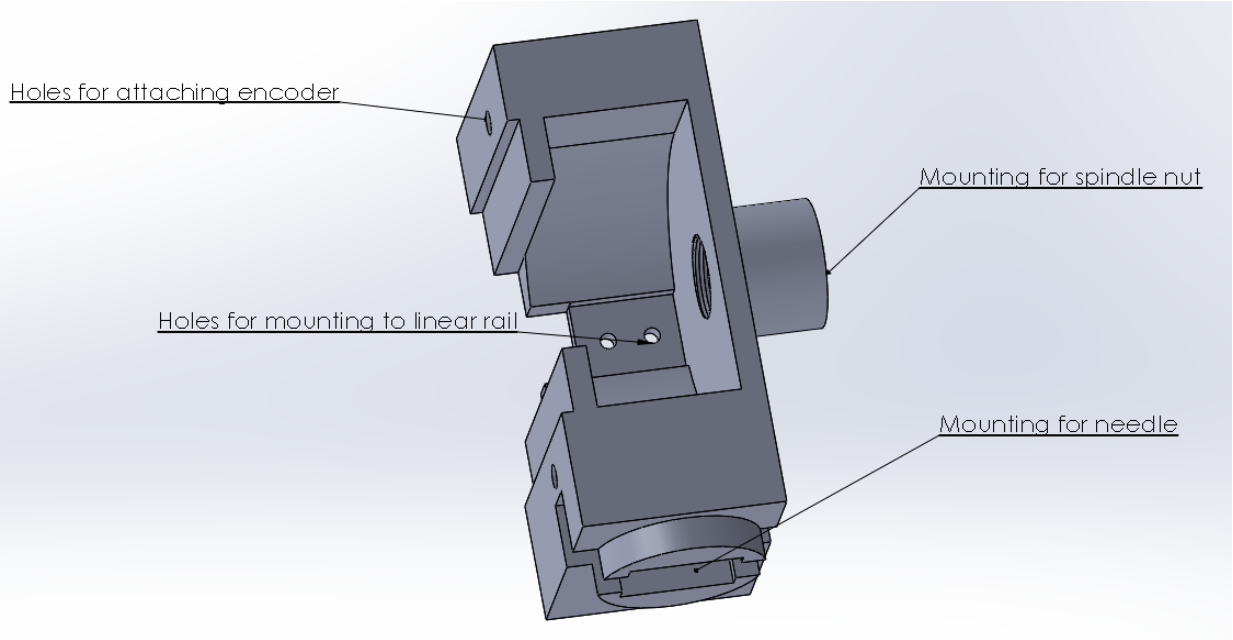

Figure 14: Concept 3D design for mobile optical encoder and needle mount

The prototype model for the needle insertion end effector at this stage is illustrated below in Figure 15.

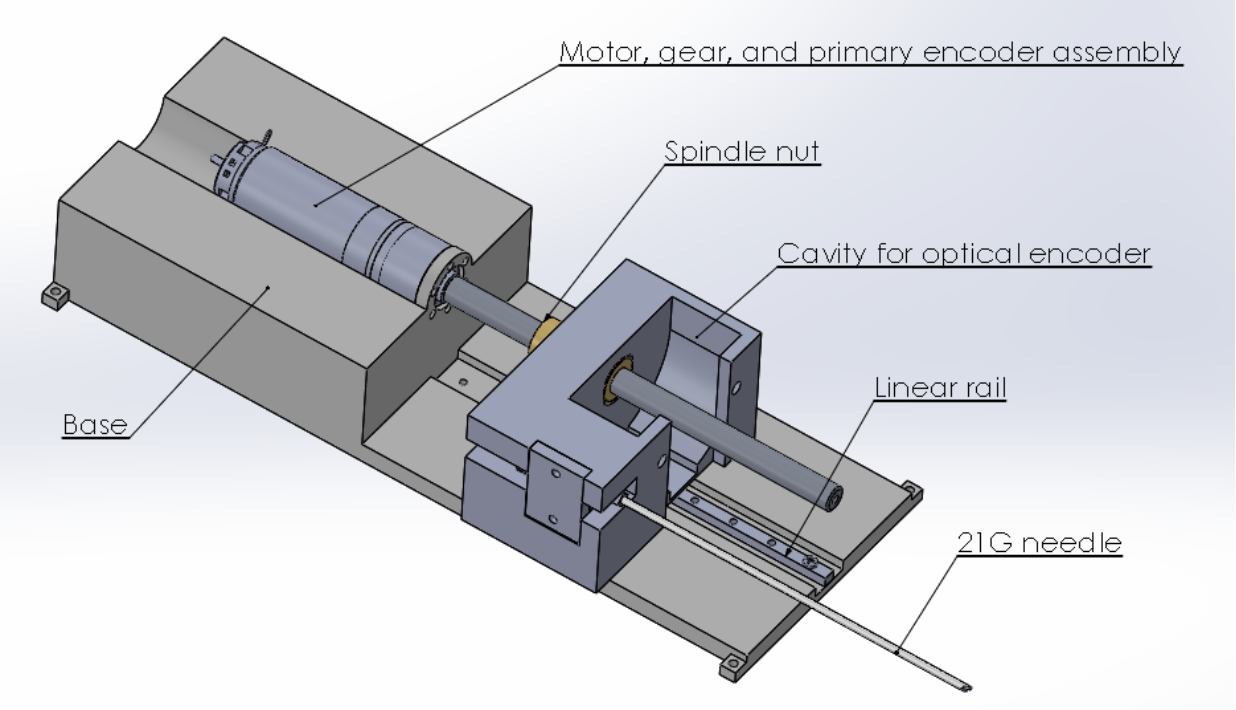

Figure 15: Prototype featuring mobile optical encoder

At this stage, another design revision was needed because the optical encoder functions by detecting the rotation of the spindle. An incorrect assumption that the secondary QD145 optical encoder functioned by “seeing” the rotation of the spindle was made. The encoder actually functions by sensing the rotation of its metallic inner core. The QD145 optical encoder has two small screws that are tightened onto the spindle itself. If, as in this design, the encoder translates with the spindle nut, the optical encoder would not function properly.

In order to stabilize the spindle, while also reducing the mass at the insertion end of the device near where an ultrasound probe will be resting in a future design revision, the optical encoder will be mounted directly in front of the drive spindle. This new design is illustrated in Figure 16 below.

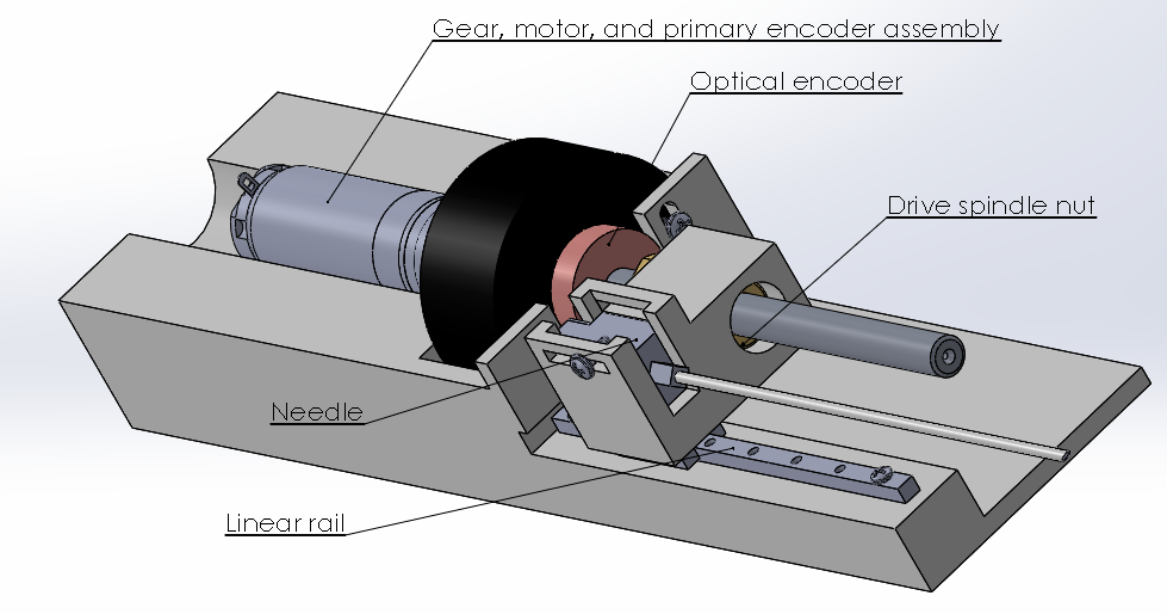

Figure 16: Prototype with a stationary optical encoder mounted near motor

This design allows the optical encoder to function appropriately by staying stationary. It also allows for the maximum insertion depth allowed by the current linear rail of 5 cm. Any deeper insertion depths would require a new linear rail.

When this design was printed, a design flaw was identified which prevented the assembly of the prototype. Also, the height of the linear rail block/needle adapter interface was not accurate in the model, although it was level in the 3D design. In Figure 17 below, the motor screws are labeled. If the motor is put in place on the base and screwed in, the spindle extends and prevents the QD145 optical encoder from being put into place. If, on the other hand, the optical encoder is screwed to the base first, it would not be possible to screw the motor into place. This figure also labels the interface between the needle adapter and linear rail block: in the 3D model, the interface is at the appropriate height and level. In the printed model, there is an offset.

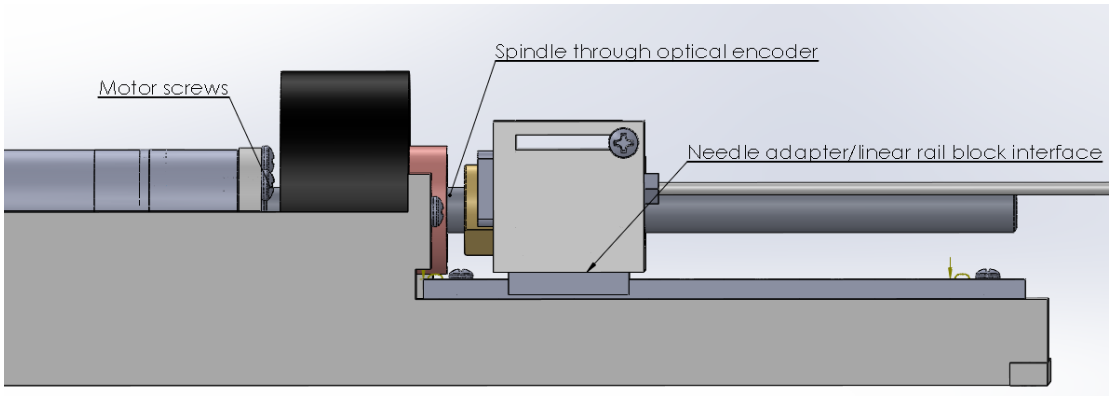

Figure 17: Illustration of assembly design issues

In order to address these problems, the design was revised to have a two piece base. The motor mounting part will be connected to a second piece upon which both the QD145 optical encoder and linear rail are mounted. This modular design will allow the prototype to be assembled. The assembly is illustrated in the following figures.

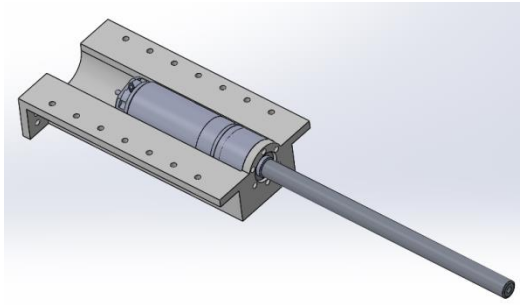

Figure 18: Motor mount of modular base prototype

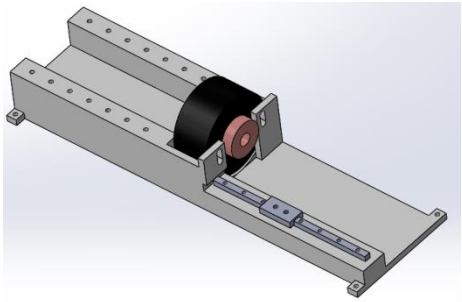

Figure 19: Linear rail mount of modular base prototype

Figure 18 shows the first step in the assembly process, the mounting of the motor, gear, and spindle assembly to the base motor mount. Figure 19 details the second step, the mounting of the optical encoder and linear rail to the second part of the base. The third assembly step is illustrated below in Figure 20 and involves the insertion of the spindle

through the hole in the QD145 optical encoder and the connection of the two base parts via multiple screws.

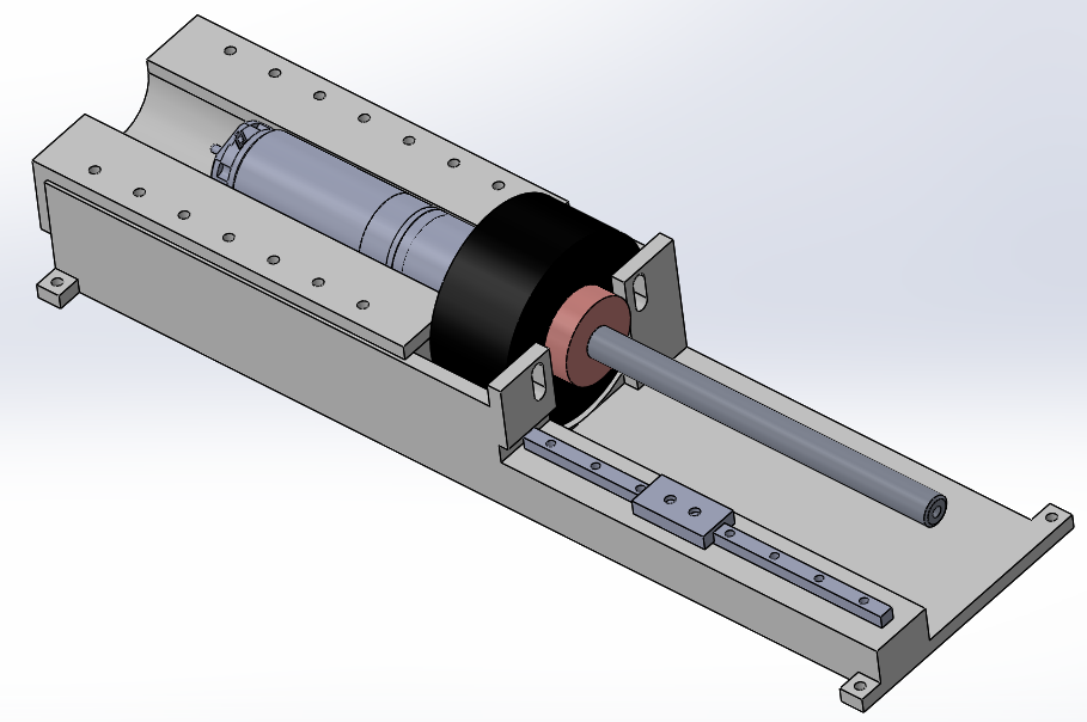

Figure 20: Modular base prototype assembled

In the initial 3D printing of this design, the screw holes shown on the top of the motor base in Figure 20 did not align correctly with their corresponding holes in the primary base (the larger part of the base located beneath the motor, illustrated in Figure 19). This was caused by the improper mating of the rear surface of the primary base with the back surface of the motor base. The design of the motor base was therefore modified to increase the length of the overlap area between the motor and primary bases. The revised motor base design also included a wider support for the motor mounting, as the printed component was very fragile. This version of the motor base is shown in Figure 21.

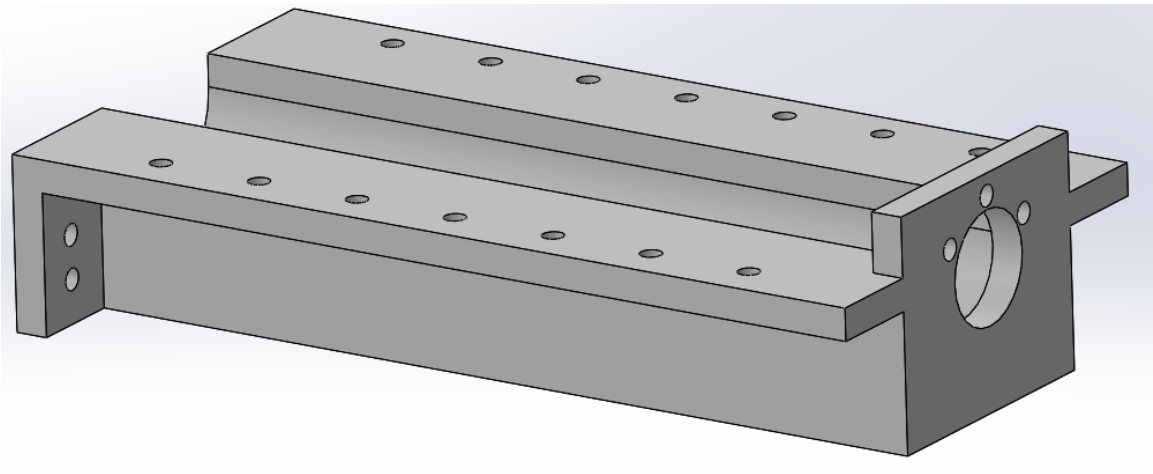

Figure 21: Motor base modified for better mating with the primary base and enhanced durability of the motor mount

At this point, all of the components of the robotic needle driver were assembled and test needle insertions were made in an ultrasound nerve phantom, after a software library was written to provide motor control. With a functional needle insertion mechanism, the design needed to be modified to allow for the clamping of an ultrasound probe to the needle driver and for the angle between the ultrasound probe and needle to be changed.

During the initial designs for incorporating a second motor and an ultrasound probe clamp, it was evident that the distance between the needle driver and the ultrasound probe would be too great if the QD145 secondary encoder was used: for this reason, future designs would not incorporate the secondary encoder.

As the finished needle insertion end effector will mount an ultrasound probe in close proximity to the needle, the possible orientations of the needle and ultrasound probe in

relation to one another needed to be considered. Also, the calculation of the range of depths at which nerves could be targeted needed to be calculated.

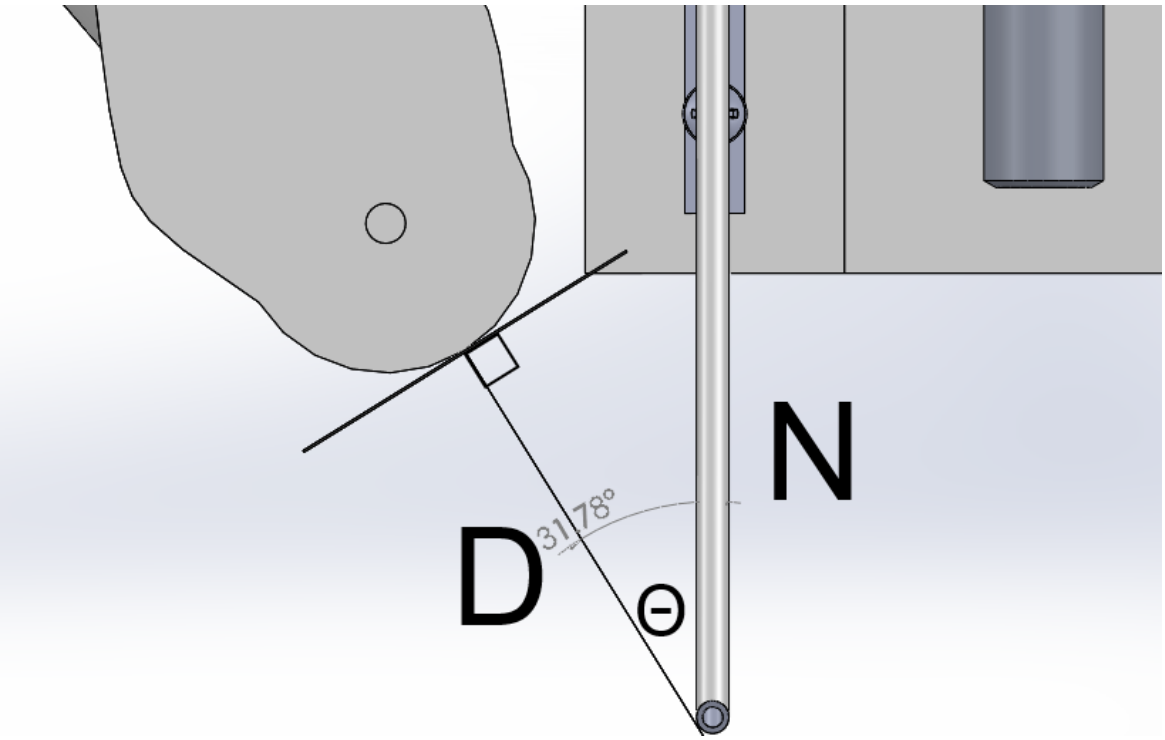

Figure 22: Orientation of needle and ultrasound probe during insertion

In Figure 22, the orientation of the needle and ultrasound probe can be seen. In this figure, a right triangle is illustrated, with the hypotenuse labeled N for the needle and the other, longer side of the triangle labeled as D, with the angle between these two sides labeled as theta (Θ). Using trigonometry, it can be shown that:

$$\cos\theta = \frac{D}{N}$$

Then, solving for D, the distance from the tip of the ultrasound probe to the tip of the needle, where we assume the target nerve to be, we have:

$$D = N * \cos\theta$$

When the target nerve is identified on an ultrasound image, it will need to be placed in the center of the ultrasound image. Then, the distance from the top of the ultrasound image to the target needle insertion coordinate (such as the center of the identified nerve) will be measured. This would represent D in the above equations. Then, the system has two parameters that it must choose, the angle between the ultrasound probe and the needle (Θ) and the depth at which to insert the needle (N). The physical dimensions of the system place limits to both of these variables. For example, if the needle cannot be driven more than 6 cm and the possible angles of deflection are between 10° and 35°, the needle could hit a nerve at a maximum depth of 5.9 cm with Θ=10° and 4.9 cm with Θ=35°. For example,

$$D = 6\ \text{cm} * \cos 10° = 5.9\ \text{cm}$$

With an understanding of how the ultrasound probe and needle need to be positioned in relation to one another, the design was heavily modified to incorporate the necessary changes. This modified design is shown in Figure 23.

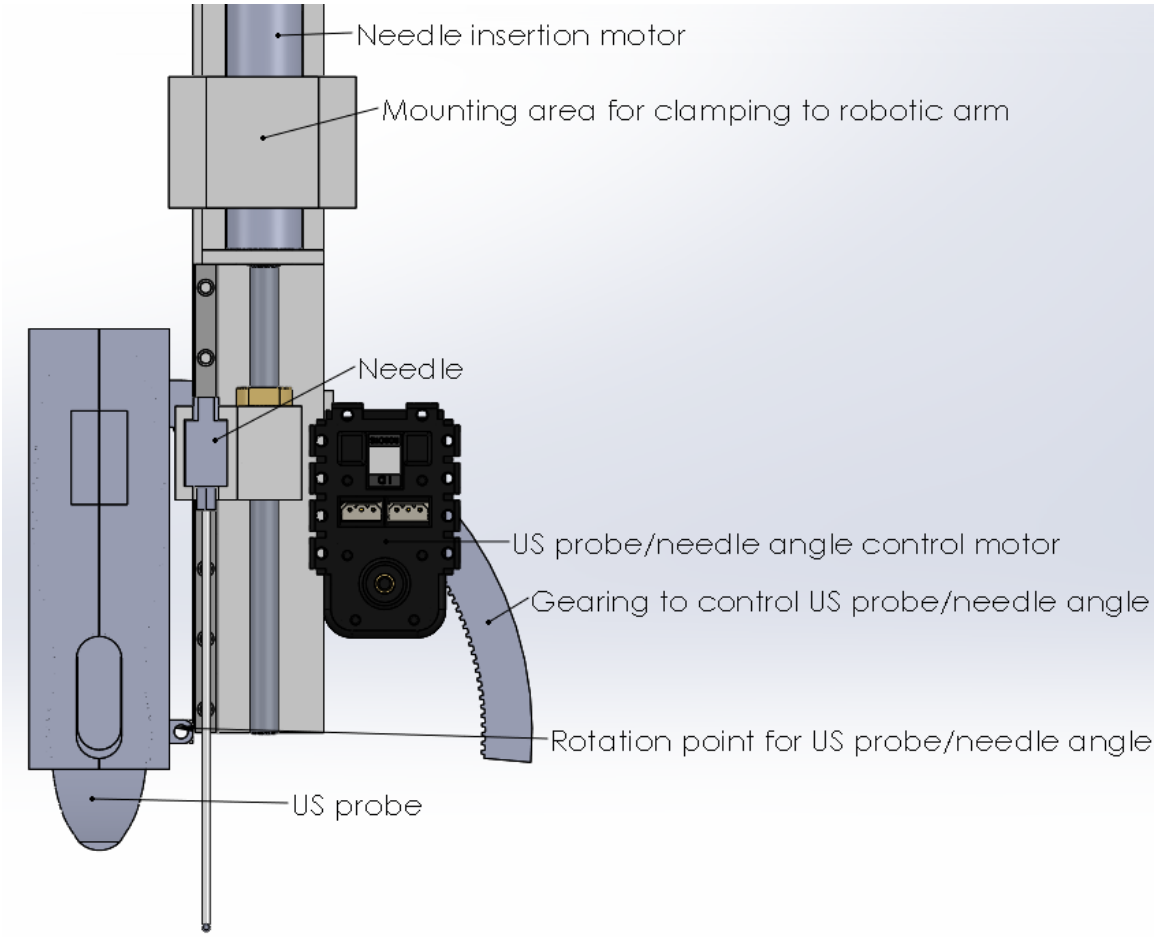

Figure 23: Initial design incorporating ultrasound probe and needle insertion mechanism

In this design, the angle between the US probe and the needle is controlled using a servo motor attached to a custom gear head and an extended geared arm which is connected to the US probe clamp (shown in detail in Figure 24). The custom gearing is very fine, with a space between gears of 0.5 mm. This was found to be the smallest possible gear teeth that could be reliably printed with the Replicator 2 3D printer used to create the custom pieces used in this prototype.

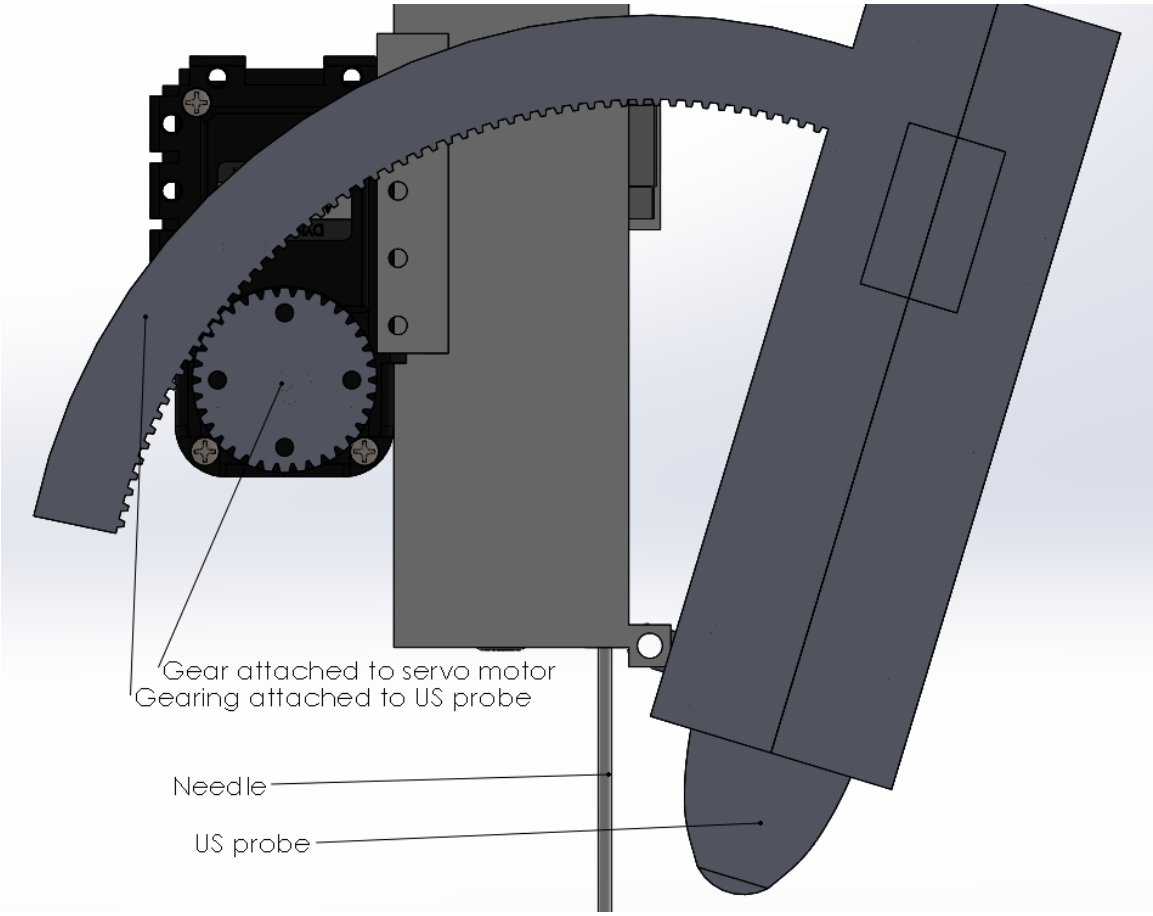

Figure 24: Detail of angle control mechanism

Test pieces of this design were printed in order to verify the sizing of the needle mounting clamp and the compatibility of the gear teeth. Before the entire prototype was printed and constructed, however, it was evident that there was a serious design flaw: when the angle control motor rotates, the US probe would move and not the needle because the needle driver is attached to the robotic arm (via the mounting area detailed in Figure 23). The design thus needed to be modified to mount the US probe to the robotic arm, and not the needle driver. Another design issue that was encountered was that the half of the US probe mounting clamp that contained the large gearing arm

(shown in Figure 24) could not easily be printed on the 3D printer. As a result, the design was modified to allow the gearing arm to be printed separately and then screwed to the US probe clamp. This revised design had the added benefit that the gearing could be easily modified or replaced without the necessity of re-printing the US probe clamp. One other design modification made at this time was a change in the linear rails. The new linear rail, manufactured by Misumi Corporation and listed in Table 2, is 10 cm long (i.e., 2 cm longer than the previously used linear rail) and thus allowed for deeper needle insertions.

When this revised design was printed, several problems were encountered. These include: the screw holes for mounting the linear rail to the motor base were too large, insufficient clearance for the screws to attach the needle holder to the linear rail, and the gear for the AX-18a secondary motor was too small (i.e., the teeth of the gear did not stay in contact with the gearing on the articulated arm). The greatest problem, however, was that insufficient support was provided between the motor base and ultrasound probe clamp assembly. A design iteration was then made to correct these flaws in the model.

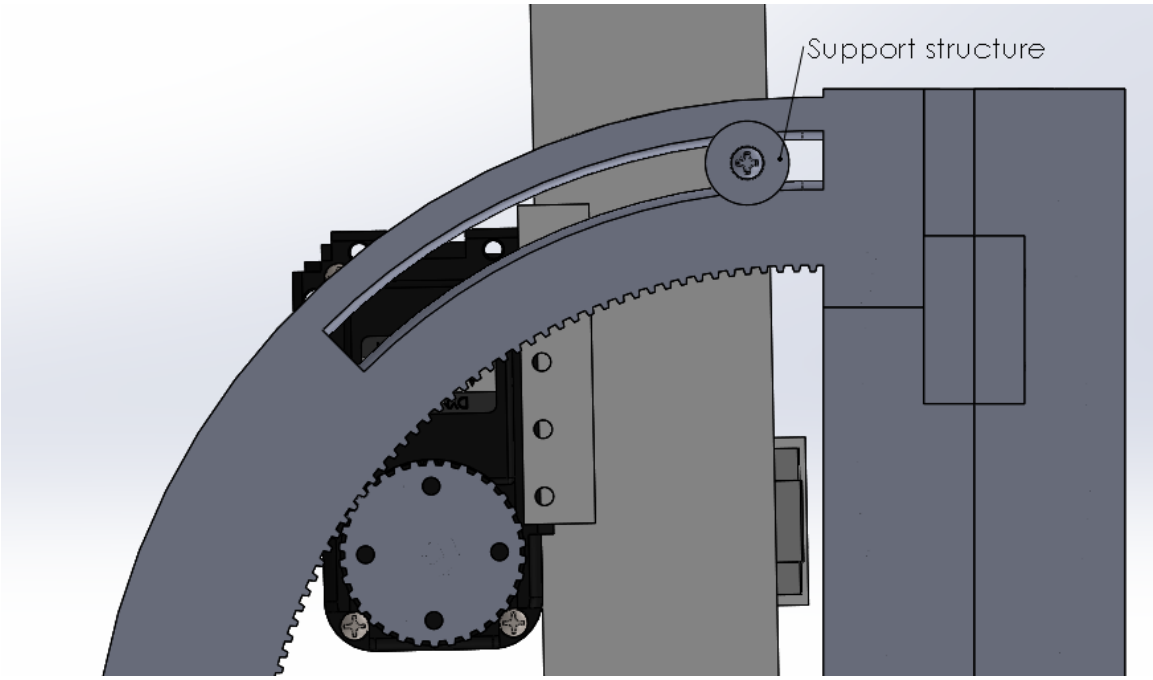

Figure 25: Front view of improved support between ultrasound probe and needle driving mechanism

Figure 25 illustrates the modifications made to the design, namely the inclusion of a support structure between the needle insertion mechanism assembly and the articulated gearing arm. This new support structure adds an additional connection point between these two structures and also adds a physical limit to the rotational range between them. A side view of the improved support structure is shown in Figure 26. The revised design also addressed the issues with screw hole sizes and modified the size of the round gear mounted on the secondary motor.

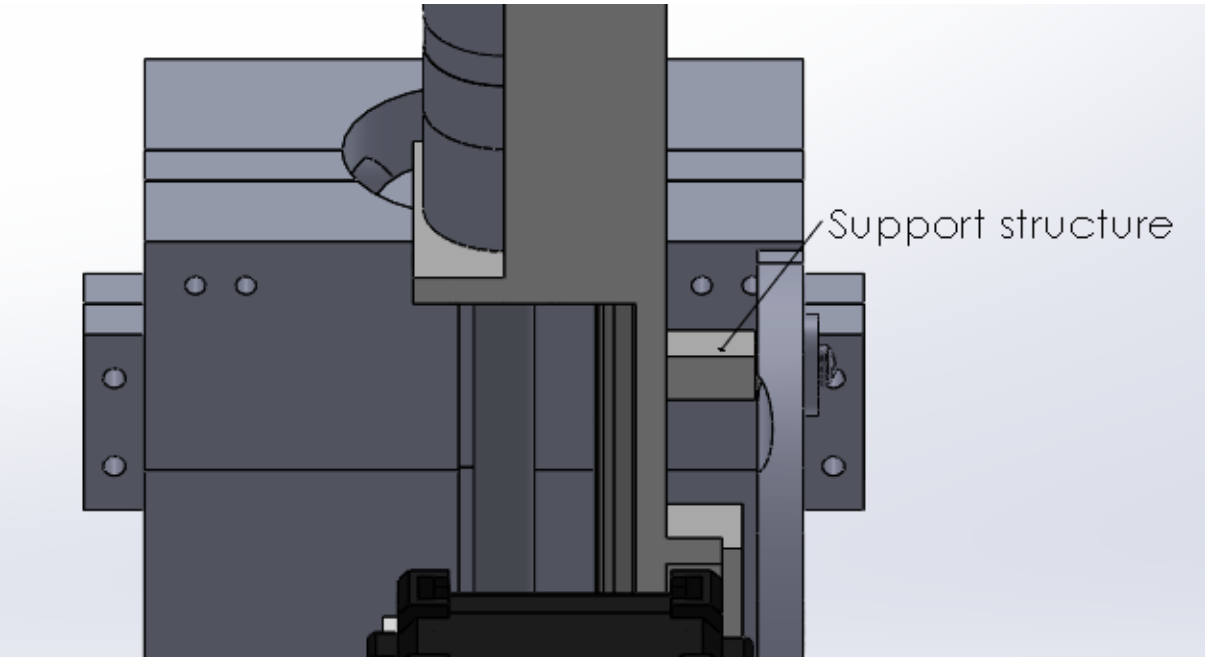

Figure 26: Side view of improved support between ultrasound probe and needle driving mechanism

After this revised design was printed on the Replicator2 3D printer, it was found to that the two geared surfaces were not compatible. As these geared surfaces were custom designed in SolidWorks, the process of revising the gearing until they were compatible would likely be lengthy and so a search was made for commercially available gears that could be incorporated into this design. The gears that were commercially available were not mountable on the angle control motor (AX-18a), however, without modification. Thus, a new design was created that would not use gears. This design is illustrated in Figure 27.

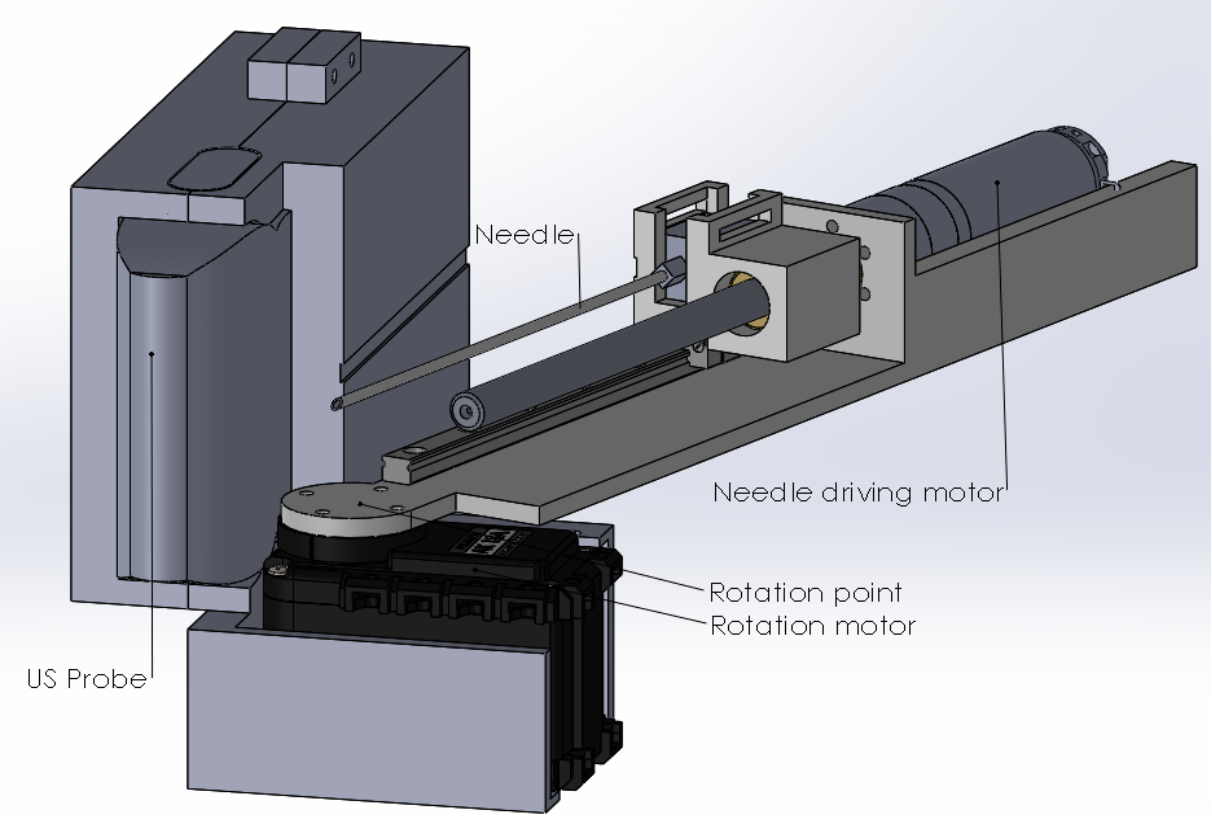

Figure 27: Design of needle driver and ultrasound probe angle control without gears

This revised design has the needle driver rotating directly upon the AX-18a motor. This design was fully functional after it was 3D printed.

Design problems encountered

Throughout the entire design process, several design problems were encountered, sometimes at multiple points. The types of design problems were related to tolerances, improper assumptions, issues preventing proper assembly, and the capabilities of the prototype 3D printer. This section details examples of each type of design problem and how it was addressed.

Engineering tolerances are permissible limits to the variation of the dimensions in a mechanical system. During the design process of the robotic needle driver, tolerances created problems at many different times. An example is in the design of the mounting mechanism for the needle: when the cavity for holding the needle was first designed in SolidWorks, it was designed to the exact outer dimensions of the mounting surface of the needle. After a 3D print of the first test piece to hold the needle was made, it was evident that the needle would not fit into the designed cavity. A revised design was made that removed 0.1 mm from each dimension and this resulted in a tight fit between the needle and the adapter. This tolerance was then used at every interface between parts for the custom 3D designs used in the project.

Improper assumptions also led to many issues in the design process. For example, at one phase of the prototyping of the robotic needle driver, the QD145 optical encoder was intended to be mobile and attached directly to the spindle nut in order to add stability to the drive spindle. The possibility of this design decision lied in the incorrect assumption that the optical encoder worked by seeing the rotation of the drive spindle. However, the QD145 optical encoder actually operates via the rotation of its metallic inner section and not the direct seeing of the spindle rotation. In order to accomplish this, two screws are tightened against the spindle from the inner metallic core of the encoder. These screws cause the metal section of the encoder to rotate in turn with the

spindle. Once this was known, the prototype design had to be changed to keep the QD145 stationary.

Issues that prevented proper assembly of the prototype were also encountered. An example of these issues was in a prototype design which had the QD145 optical encoder located directly in front of the mounting holes for the motor, gear, and spindle assembly. If the motor assembly was mounted to the base first, the spindle prevented the QD145 optical encoder from being attached to the base (as the spindle needs to be inserted directly through a hole in the encoder). If, on the other hand, the optical encoder was attached to the base first, it would be impossible to screw the motor to the base as the encoder would be in the way. These assembly step problems were encountered numerous times and were always fixed by slight changes in the prototype design.

The capabilities of the MakerBot Replicator 2 3D printer also caused problems during the design process. For instance, the printer had a difficult time printing surfaces with a thickness of less than approximately 3 mm. For this reason, all surfaces of the custom 3D models designed for this project were kept to a minimum thickness of 3 mm. This design strategy resulted in a drastic reduction in the number of failed 3D printings.

Needle insertion control

The design of the needle driver imposes physical constraints on the control equations for this robotic system. Figure 28 depicts important physical dimensions overlaid on the needle driver.

The needle driving mechanism is connected directly onto a motor mounted directly to the US probe clamp (labelled as Rotation point in Figure 27). As the needle rotates about this point, the angle labeled θ in Figure 28 changes. At each angle, there is only a single place where the needle will intersect the plane of the US beam which emanates from the bottom of the probe.

The user of this system will know the depth of the nerve in the US video feed. This distance is represented as Nd in Figure 28. This value, as known by the clinician performing the nerve block, is the ideal variable upon which to control the motors for driving the tip of the needle into the nerve. Two parameters need to be calculated in order for this to happen: the angle between the US probe and the needle (represented by θ in Figure 28) and the distance to drive the needle forward. These two parameters specify the movement necessary for the two motors of the system. The derivation of the equations necessary to solve for these two values given the nerve depth in the US image is provided below.

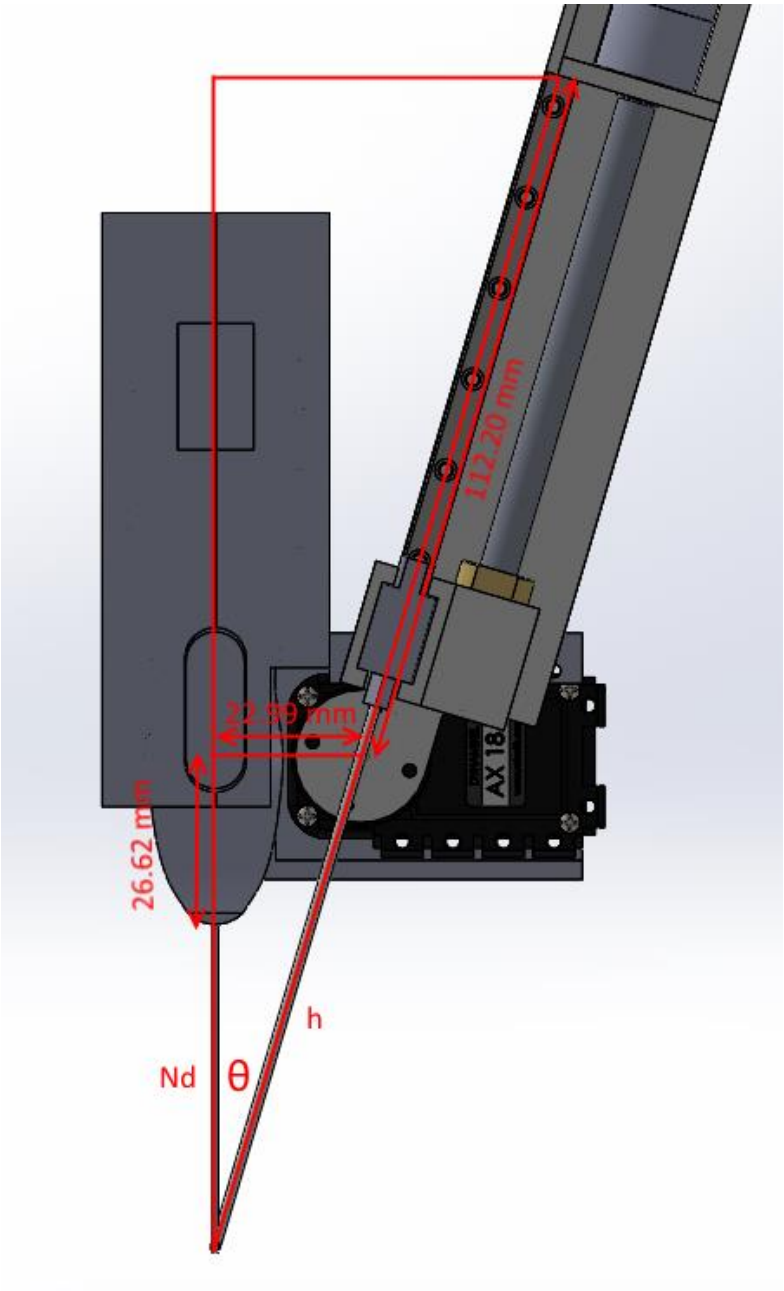

Figure 28: Illustration of a few physical dimensions of the needle driver

Using the definition of tangent on the lower triangle shown in Figure 28, it can be shown that:

$$\tan\theta = \frac{22.99\ mm}{26.62 + N_d\ mm}$$

Solving this equation for θ, we have:

$$\theta = \tan^{-1}\frac{22.99}{26.62 + \ \mathrm{N_d}} \ (\mathrm{E1})$$

Similarly, using the Pythagorean Theorem on the lower triangle depicted in Figure 28, it can be shown that:

$$(26.62 + N_d)^2 + \ 22.99^2 = h^2$$

Solving this equation for h, we have:

$$h = \ \sqrt{(26.62 + N_d)^2 + \ 22.99^2} \ (\mathrm{E2})$$

Knowing then the length of the needle is 114 mm and the distance from the point of rotation to the base of the needle in its fully retracted position is 112.20 mm, we can then calculate the necessary distance, I_d, to move the needle forward as:

$$I_d = (112.2 + h) - \ 114 \ \mathrm{mm} \ (\mathrm{E3})$$

Now, using equations E1 and E3, we can solve for the movement necessary for the rotational motor (i.e., θ) and for the movement necessary for the needle driving motor (i.e., I_d).

System Testing

In order to evaluate the accuracy and precision of the needle driver developed in this thesis, tests were conducted on a precision-machined Linear Testing Apparatus (LTA) developed by Gerard et al. in order to quantify the error in tool placement for image-guided neurosurgery (Gerard & Collins, 2014). The LTA features a 500 mm x 500 mm plate with a 10x10 grid of holes separated by 50.00 mm, milled with a 0.005 mm tolerance. Therefore, the position of any device mounted to the LTA is known within 50.00 ± 0.005 mm in both the horizontal and vertical directions. The LTA also features precision-milled aluminum rods, milled with a tolerance of 0.01 mm and available in lengths that vary by 10 cm, which allow tools, such as cameras, to be mounted and positioned precisely in relation to the mounting grid. The LTA, its spacing rods, and its tool mounting platform are featured in Figure 29.

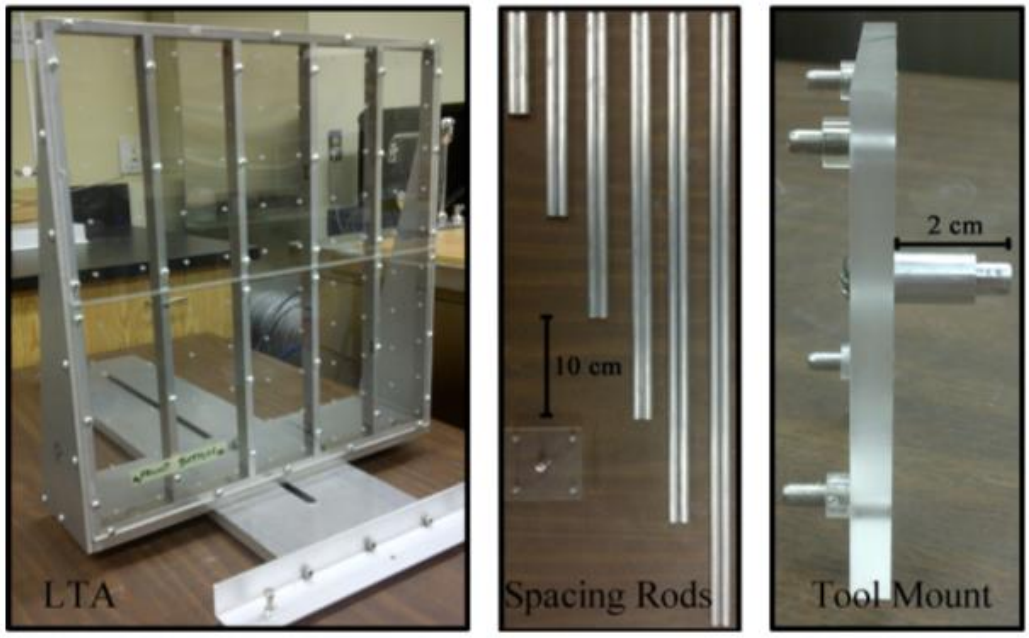

Figure 29: Illustration of the Linear Testing Apparatus (Gerard & Collins, 2014)

For the tests of the accuracy and precision of the needle driver, the needle driving mechanism was mounted onto the LTA using the supplied tool mount. A 30 cm spacing rod was then used to mount a digital camera (Sony NEX-5N, Sony Corporation, Tokyo, Japan) with a lens with an adjustable focal length (18-55 mm). This 16.1 megapixel camera has a resolution of 4912x3264 pixels, a 23.4x15.6 mm CMOS sensor, and a lens with an adjustable focal length (18-55 mm). This setup is shown in Figure 30.

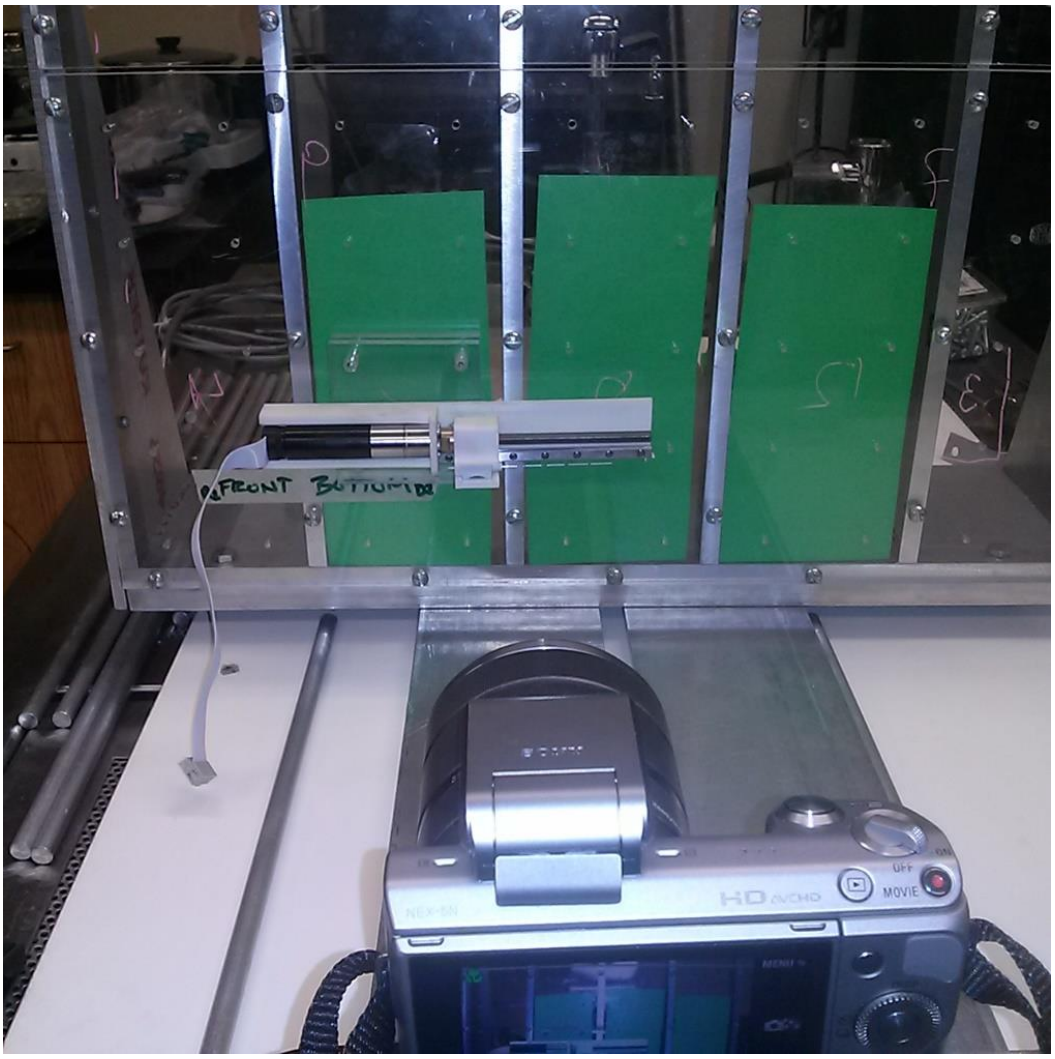

Figure 30: Set up of needle accuracy and precision testing using Linear Testing Apparatus and Sony NEX-5N digital camera

A planar aluminum sheet was used to place the lens of the camera perpendicular to the mounting plate of the LTA. As the needle is mounted parallel to the needle driver, which is itself mounted parallel to the plane of the mounting plate of the LTA, this also means that the camera lens was mounted perpendicular to the needle and needle driver.

This camera was used to take still frames of the needle after specific movements. Two different types of movements were conducted in order to test the accuracy and precision of the system: trials of moving the needle in distances of 10 mm were conducted, followed by trials of repeatedly moving the needle two specific distances (5 and 6 cm). The repeatability trials were conducted at three different motor speeds in order to quantify any effect on accuracy that the motor speed might have. The chosen speeds were 10,000 rpm, 7,500 rpm, and 2,500 rpm. The movement trials (in increments of 10 mm) were all conducted at 10,000 rpm. 20 measurements were made for both the movement trials and the repeatability trials (10 measurements at 5 cm, 10 measurements at 6 cm).

These same trials were then repeated using a Polaris infrared optical tracker (Northern Digital, Waterloo, Ontario, Canada) as the measuring device. For the optical tracking trials, a position marker with three reflective markers was zip tied to the needle adapter and its change in position between consecutive trials was recorded.

After the analysis of the images and optical tracker data, it was found that a third measurement device should be used due to noise and measurement bias present in

both other measurement modalities. The reasoning behind this is explained in detail in the Results section of this chapter. For this reason, a Mitutoyo digital caliper (500-196-30 Absolute AOS Digimatic Caliper, Mitutoyo Corporation, Kawasaki, Japan) with a resolution of 0.01 mm was used to repeat all of the measurements.

Still frame image analysis methodology

For the analysis of all images taken using the Sony NEX-5N digital camera, Paint.NET (dotPDN LLC) was used. To measure the distance between consecutive images, the reference image was opened as a layer with an opacity of 50%. A region containing the spindle and the needle adapter was then cut from the second image and imported as a layer above the opaque reference layer. The two layers were then overlaid so that the threads of the drive spindle were perfectly aligned. The translation of the spindle nut was then measured. An example of image analysis is shown in Figure 31, where the red line is 562 pixels in length.

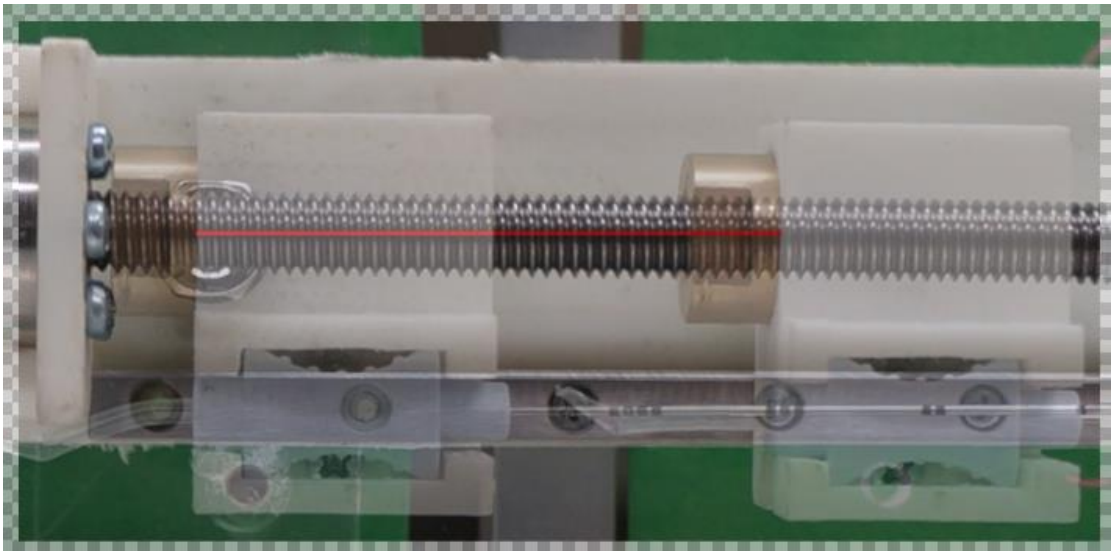

Figure 31: Example of image analysis for linear accuracy and precision testing

The conversion from pixels to distance was facilitated by the fact that each thread on the spindle drive is 1 mm apart. In the reference image, the distance between each thread was measured over 10 threads and averaged to be 14 pixels. Thus, the distance of 562 pixels in Figure 31 is 562/14=40.142 mm.

Linear needle driving accuracy and precision testing results

The results for the movement trials using both the Sony NEX-5N digital camera and the Polaris optical tracker are presented in Table 7 in Appendix 1. The repeatability results for the measurements made at 10,000 rpm, 7,500 rpm, and 2,500 rpm are listed in Table 8,

Table 9, and Table 10, respectively, for both camera and optical tracker trials. The means and standard deviations for all trials are presented below in Table 5.

Table 5: Means and standard deviations of needle placement error from linear motion testing

	Camera	Optical Tracker
	Mean (SD) (mm)	Mean (SD) (mm)
Movement trials @ 10,000 rpm	0.161 (0.098)	0.106 (0.077)
Repeatability trials @ 10,000 rpm	0.164 (0.106)	0.462 (0.090)
Repeatability trials @ 7,500 rpm	0.157 (0.100)	0.445 (0.064)
Repeatability trials @ 2,500 rpm	0.161 (0.106)	0.447 (0.068)

The boxplot in Figure 32 graphically depicts the needle position error from the movement trials. In the boxplots presented in this thesis, the red lines represent the median, the top and bottom of the blue box represent the 25th and 75th percentiles, respectively, and the whiskers extend to the farthest data elements which are not considered outliers. Outliers are shown as red crosses.

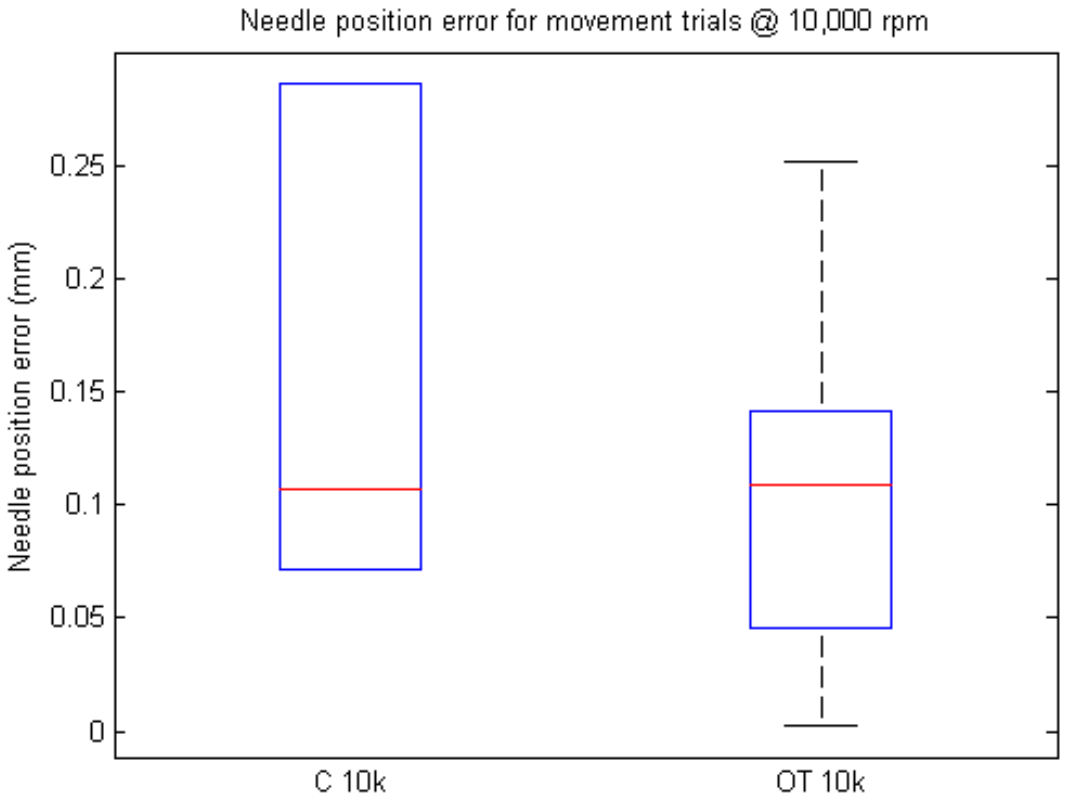

Figure 32: Boxplot of needle position error at 10,000 rpm

The boxplot in Figure 33 details the median and interquartile range of needle position errors for the repeatability trials at 10,000 rpm, 7,500 rpm, and 2,500 rpm. Camera trials are denoted with C and optical tracker results are labeled with OT. The motor speeds for the corresponding box are indicated as 10k, 7.5k, and 2.5k for 10,000 rpm, 7,500 rpm, and 2,500 rpm, respectively.

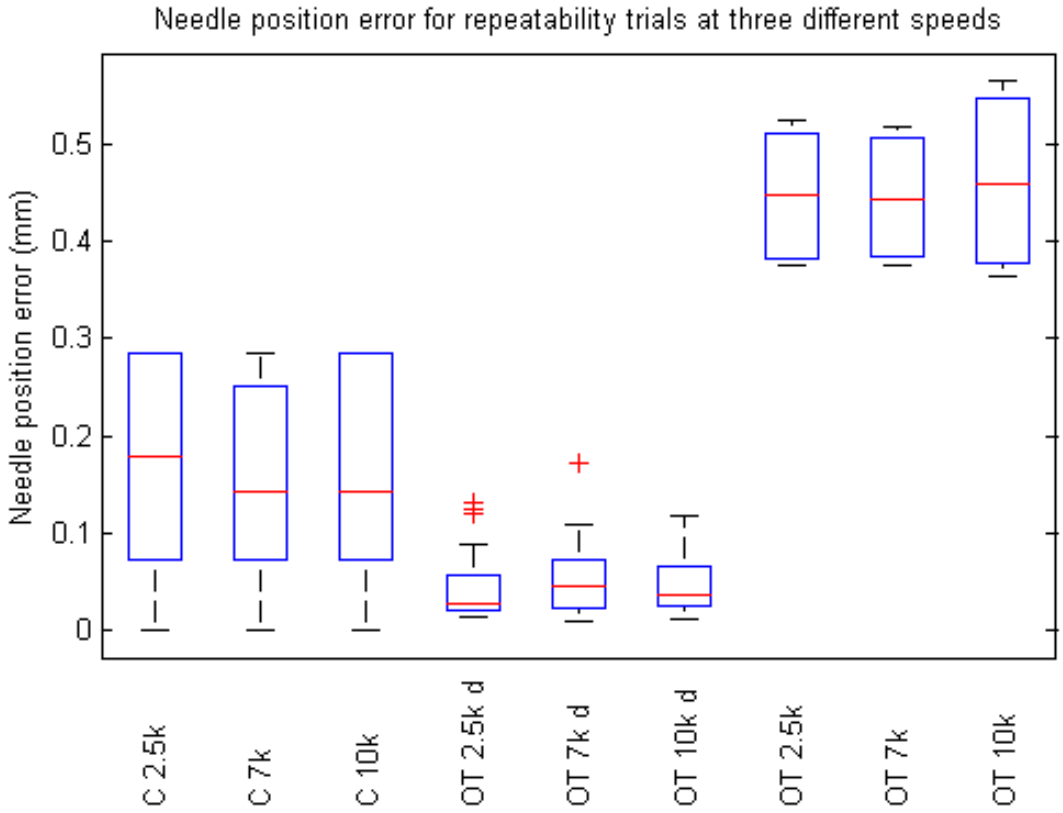

Figure 33: Boxplot of needle position error for repeatability trials at three different speeds.

For the repeatability trials at each speed, the optical tracking data had a greater measured mean and median than those obtained using the digital camera measurements. The Polaris optical tracker is susceptible to noise and jitter caused by reflections of the infrared light it uses for position tracking. These higher values are consistent through all motor speeds and for all trials, but do not agree with the visually determined accuracy measured from the image analysis of the images taken using the Sony NEX-5N digital camera.

In order to further evaluate these results, the difference between each individual trial of the repeatability trials from the optical tracker was calculated. The box plot of these values is also shown in Figure 33. These values are shown in the central 3 boxes, labeled with a “d” to denote difference measurements. These values show us that the noisy optical tracker measurements confirm that there is a very small range in the difference between consecutive movements to the same position. The mean and standard deviations for these values at 10,000 rpm, 7,500 rpm, and 2,500 rpm were 0.046 (0.029) mm, 0.056 (0.041) mm, and 0.046 (0.041) mm, respectively. These values tell us that the needle driver can repeatedly move the needle to within 60 microns (0.06 mm) of its intended position. This value is lower than the average error found from the image analysis trials and suggests that if we had another measurement device that wasn’t limited to pixel size limits to determine accuracy that we would measure a greater accuracy for the needle driver. For this reason, a digital caliper

accurate to 0.01 mm was ordered and further trials were undertaken to better evaluate the accuracy of the needle driving mechanism.

Further evidence of the necessity to test the accuracy of linear needle movement with a more accurate measurement device is presented in the scatter plot in Figure 34.

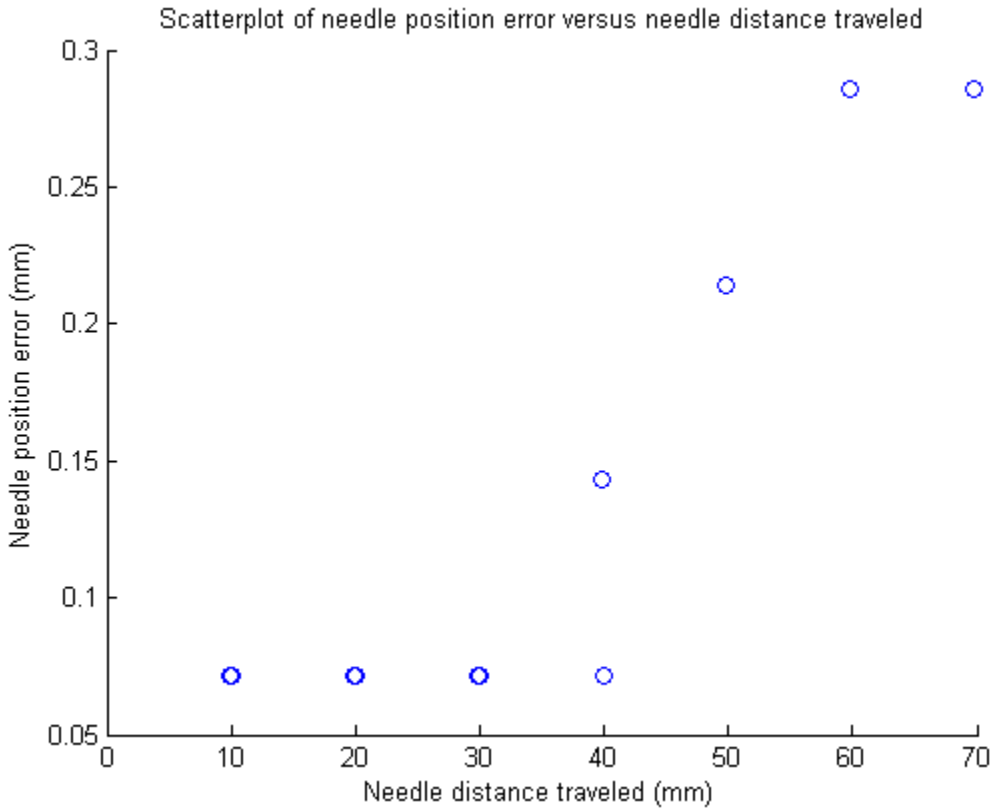

Figure 34: Scatter plot of needle position error vs needle distance traveled for the movement trials recorded using the Sony NEX-5N digital camera

The scatterplot above shows that there is a sudden jump in needle position measured after 40 mm. This is due to an increasing angle between the camera lens and the edge of the spindle nut which is used to measure the translational distance moved between consecutive images. A better experimental setup would have been to mount a different

digital camera centered on each 30 mm segment. This would provide for an accurate measurement ability over the entire movement range of the needle. The data obtained after 40 mm using the camera is biased and this demonstrates the need to conduct further trials using a more accurate linear measurement device.

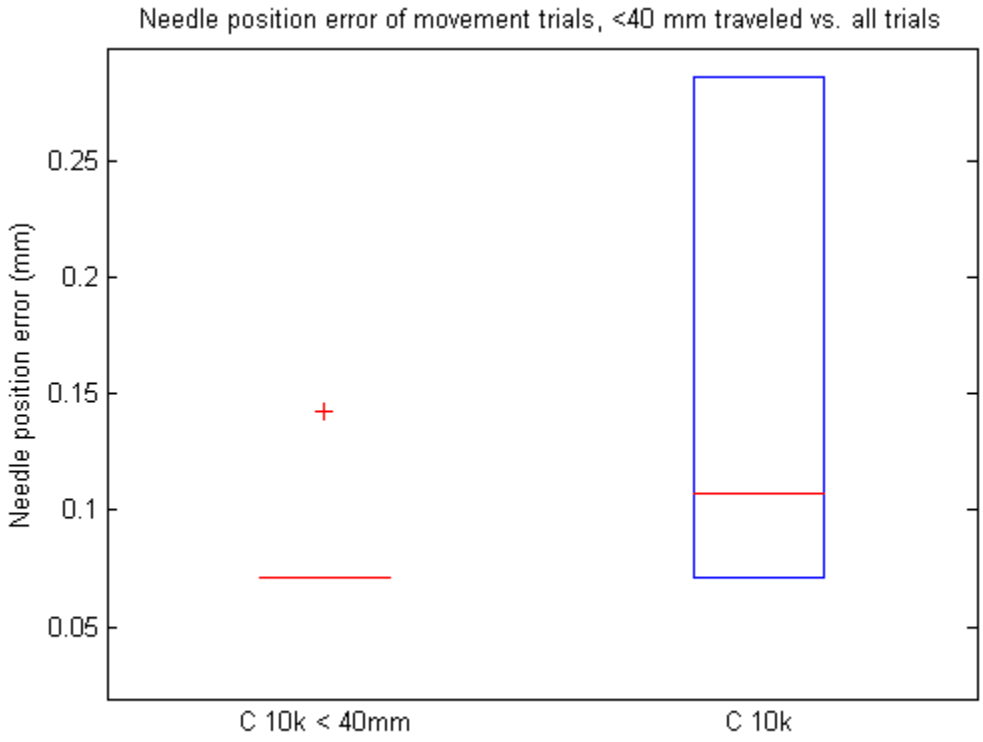

Figure 35: Boxplot of needle position error for movement trials comparing trials at less than 40 mm vs. all trials

The boxplot in Figure 35 shows the drastic reduction in both the variability and the median needle placement error when only the trials at less than 40 mm are compared to all trials. The data shows that the needle accuracy for movements less than 40 mm is accurate within 1 pixel (1 mm/14 = 0.0714 mm is the smallest possible error which can

be detected using the camera at this distance from the needle). It should be noted that all of the repeatability trials were at distances outside of this range, and thus had a bias which increased the magnitude of the measured error.

The data from the digital caliper trials are presented, alongside the data for the image analysis and optical tracker trials, in the tables in Appendix 1. The mean and standard deviations for the linear motion tests measured using the digital caliper are presented below in Table 6. A one-way ANOVA in MATLAB 2014a was used to compare the means of these four different trial types and a P-value of 0.9992 was found. Thus, there is no statistical difference between the mean errors measured in each test by the digital caliper. Thus, the needle driver has the same accuracy and precision regardless of its speed of operation.

Table 6: Linear motion testing results measured using digital caliper

Trial type	Mean (SD) (mm)
Movement trials @ 10,000 rpm	0.040 (0.020)
Repeatability trials @ 10,000 rpm	0.041 (0.024)
Repeatability trials @ 7,500 rpm	0.040 (0.024)
Repeatability trials @ 2,500 rpm	0.041 (0.019)

The boxplot in Figure 36 shows the median and interquartile range of the values obtained using the digital caliper. The data measured using the digital caliper are much more reliable than the data obtained from either the optical tracker or the image analysis

due to the formerly mentioned issues present in these measurement modalities. It should be noted, however, that all of these testing modalities have demonstrated the sub-millimeter accuracy of the linear needle driver developed in this thesis. Needle placement within 1 mm was deemed as clinically sufficient accuracy for this needle driving project.

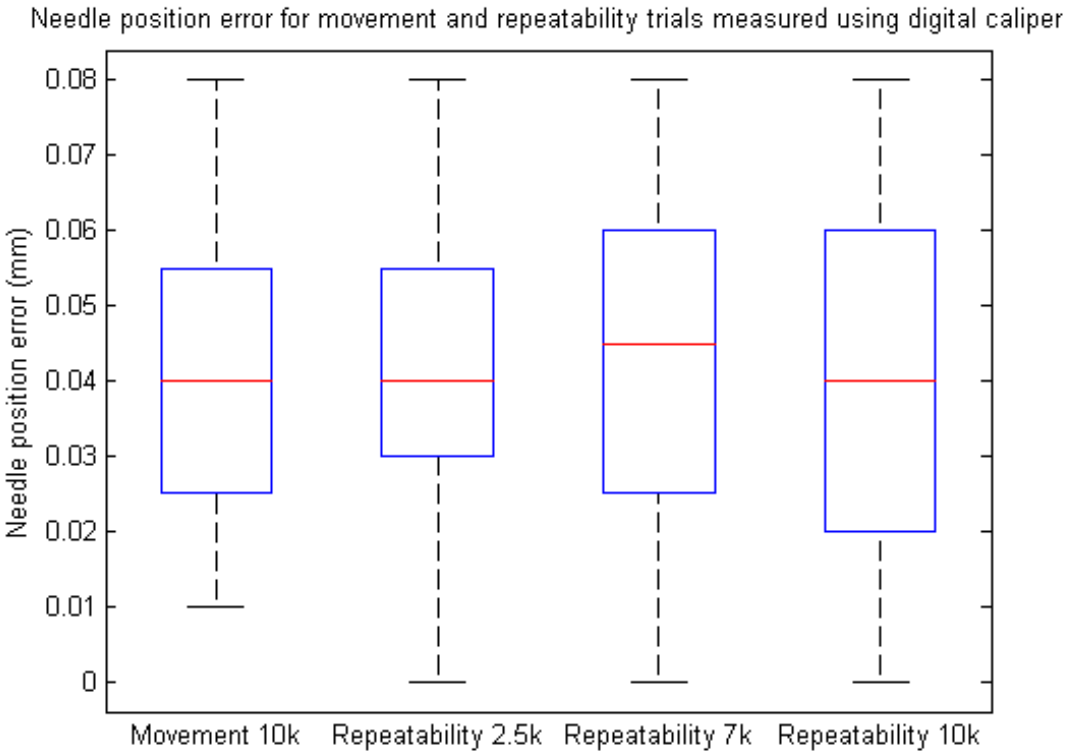

Figure 36: Boxplot of linear motion accuracy values measured using a digital caliper

After these linear motion trials were conducted, the complete system was mounted on the JACO robotic arm and a series of test blocks were performed. The needle was seen to enter the nerve but experimental measurements to quantify the accuracy of the complete system were not made. Figure 37 below was taken during the complete system testing and shows the complete needle insertion end effector mounted to a JACO robotic arm and the needle has been inserted into a nerve at a depth of 3.5 cm inside the ultrasound training phantom.

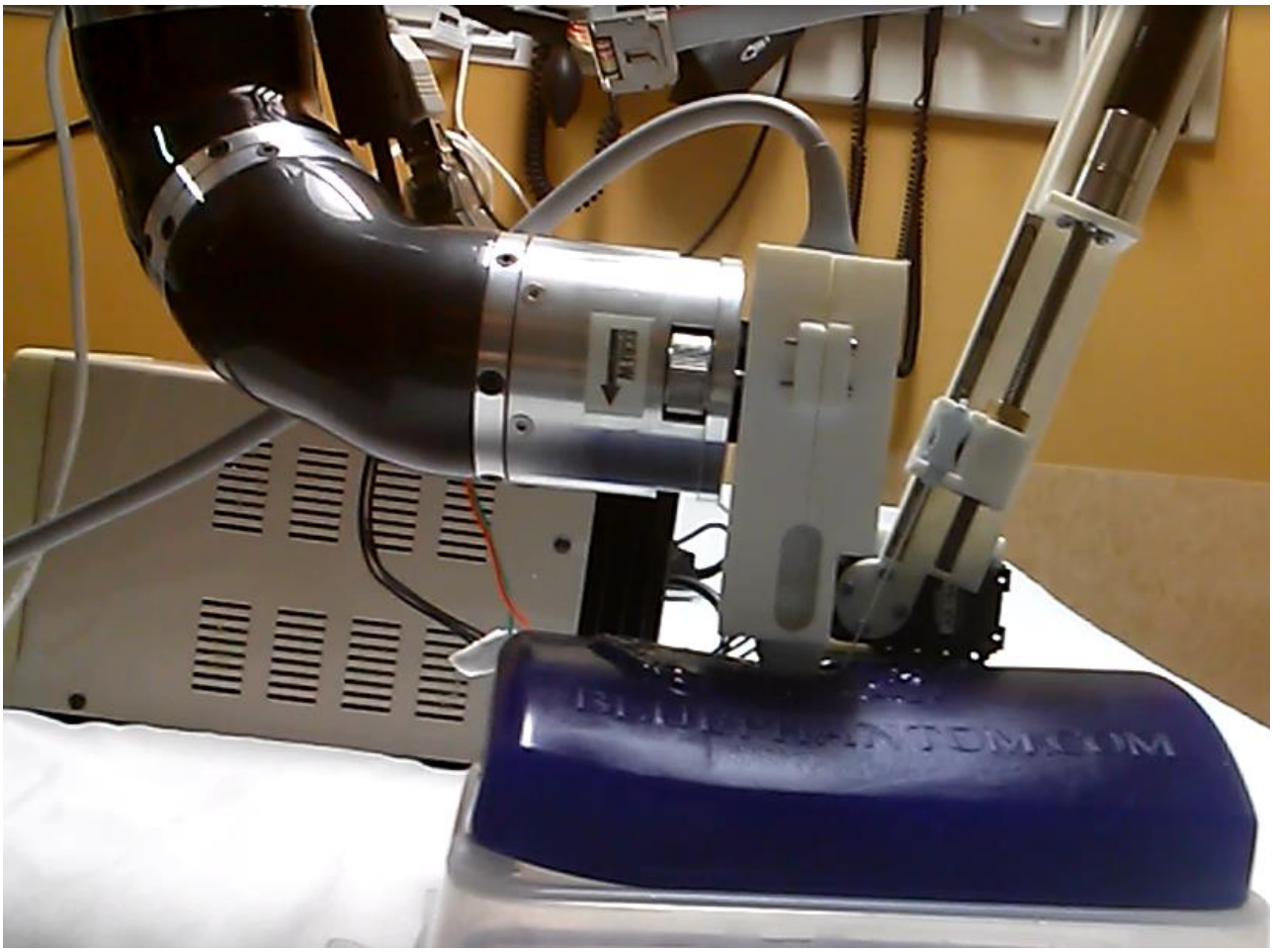

Figure 37: Complete system testing on ultrasound training phantom

Discussion and Conclusion

The Magellan robotic nerve block system was first developed and tested in 2012 on 13 patients (Hemmerling et al., 2013). These initial clinical tests demonstrated the feasibility of robot assistance for ultrasound-guided regional anesthesia. A study of the Magellan system on an ultrasound training mannequin showed that robot assistance could reduce the time it takes for novices to learn ultrasound nerve block needle guidance (J Morse et al., 2014).

The use of the Magellan system for these two studies demonstrated two weaknesses: the ultrasound probe had to be manipulated manually by another person and the needle could not be reliably driven in a straight line outside of a very small window of operation. The robotic needle insertion end effector developed in this thesis removes these two deficiencies from the system.

The linear motion testing conducted in this thesis and presented in the System Testing chapter has demonstrated the best-case accuracy of the needle driver is less than 0.1 mm, well below the 1-mm accuracy level determined as clinically relevant for needle placement for US-guided nerve blocks. This is a best-case measure of accuracy because it does not quantify important sources of needle deflection that occur during an actual needle insertion such as tissue deflection or deformation of the patient's tissue. Additional testing of the complete system is necessary in order to quantify the accuracy and precision of the rotation motor control algorithm. After this best-case analysis,

phantom testing is necessary in order to experimentally evaluate the control equations for the combined and complete system, as well as evaluate the accuracy and precision of the robotic needle driver in the presence of the largest sources of error: needle deflection caused by tissue and ultrasound-image registration errors.

When the components of this needle insertion end effector are miniaturized, they are planned to become part of a new handheld device for allowing nerve blocks to be performed single-handedly. An example of this conceptual device is shown in Figure 38.

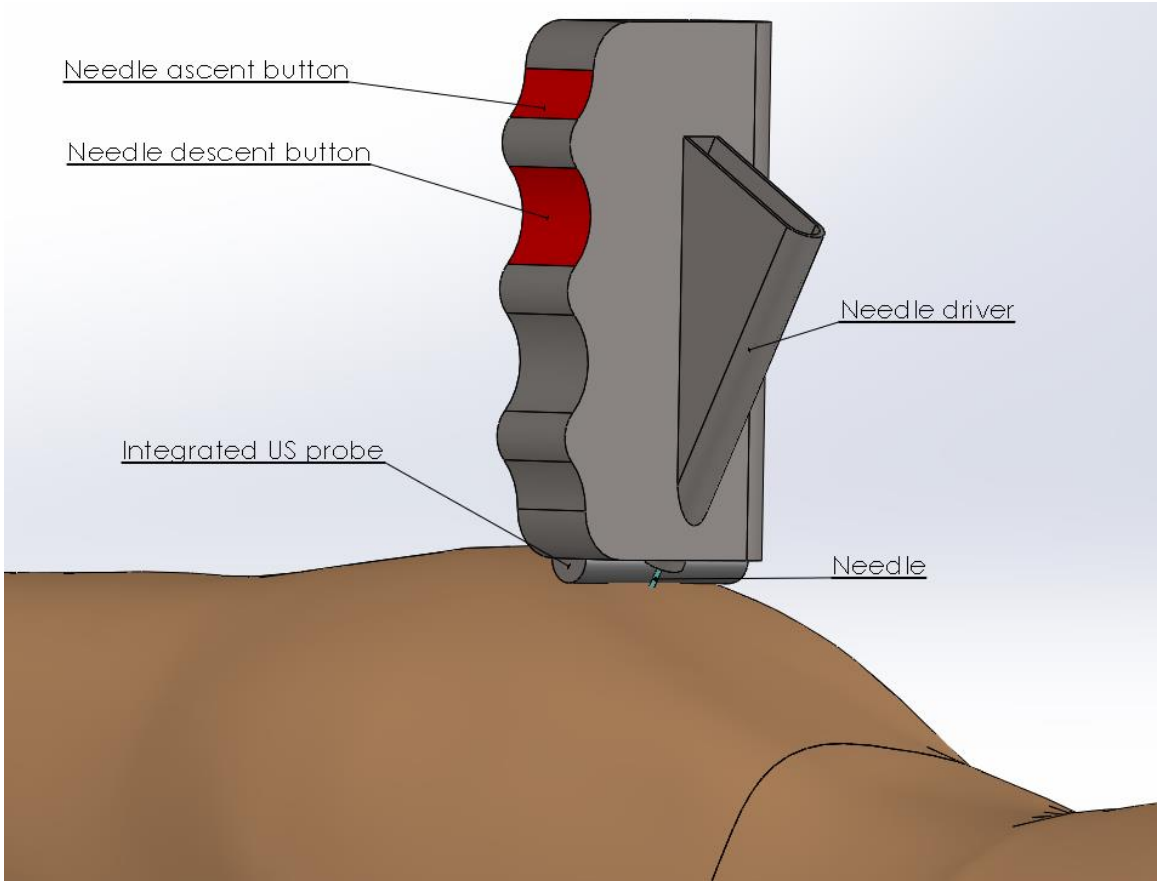

Figure 38: Conceptual image of single-handed nerve block device

In order for such a device to be created, the components used in the development of this needle driver must be miniaturized. The experimental results presented in this thesis outline that motorized control of the needle can provide for sub-millimeter accuracy in needle placement. The testing plan outlined for the future work of this robotic needle driver will necessarily need to be repeated in order to evaluate if the new, miniaturized single-handed needle driver maintains this high level of accuracy.

In addition to further testing, future work is necessary to create an intuitive graphical user interface for controlling this robotic needle driver and the JACO robotic arm. The control software can currently calculate the needle's position in relation to the US probe and this information could be used to display the location of the needle tip in the US video feed. This would eliminate the problem of needle visualization difficulty for anesthesiologists.

Before robotic assistance applications for anesthesia, such as the system developed in this thesis, can be approved by the United States Food and Drug Administration, much more engineering work is needed in order to improve their safety. Once sufficient engineering research has been conducted to improve the safety of robotic assistance systems, clinical trials will then be necessary to prove their effectiveness and justify the increased cost in their use.

The robotic needle driver presented in this thesis was demonstrated to have a clinically acceptable accuracy. When used in its current form with a robotic arm, the needle

insertion end effector allows for US-guided nerve blocks to be performed in a manner that reduces the problem of needle visualization and operator fatigue, both of which were identified as common issues for anesthesiologists performing nerve blocks. With further refinement and miniaturization, it may be possible for anesthesiologists to perform nerve blocks in a manner which eliminates several of the most common problems, while at the same time providing for a more accurate needle placement. Ultrasound guidance has improved important patient outcomes due to its ability to increase the accuracy of needle placement. Robot assistance, as provided by the needle insertion end effector developed for this thesis, has the potential to further improve needle placement accuracy and therefore continue to improve nerve block efficacy, increase block success rates, and provide longer block durations while also lowering the risk of complications.

Appendix 1: Tables of linear motion testing data

Table 7: Movement accuracy results for linear motion testing

		Camera		Optical Tracker		Digital Caliper
Trial #	Commanded position (mm)	Position (mm)	Error (mm)	Position (mm)	Error (mm)	Error (mm)
1	10	9.929	0.071	9.853	0.147	0.020
2	20	19.929	0.071	20.044	0.044	0.020
3	30	29.929	0.071	29.855	0.145	0.020
4	40	39.857	0.143	40.127	0.127	0.060
5	50	49.786	0.214	49.892	0.108	0.080
6	60	59.714	0.286	60.250	0.250	0.040
7	70	69.714	0.286	70.013	0.013	0.040
8	60	59.714	0.286	60.006	0.006	0.040
9	50	49.786	0.214	50.237	0.237	0.010
10	40	39.929	0.071	39.905	0.095	0.030
11	30	30.071	0.071	30.100	0.100	0.020
12	20	20.071	0.071	19.863	0.137	0.060
13	10	10.071	0.071	10.047	0.047	0.030
14	20	20.071	0.071	20.051	0.051	0.060
15	30	29.929	0.071	29.880	0.120	0.040
16	40	39.929	0.071	40.110	0.110	0.040
17	50	49.786	0.214	49.884	0.116	0.050
18	60	59.714	0.286	60.251	0.251	0.080
19	70	69.714	0.286	70.019	0.019	0.030
20	60	59.714	0.286	59.997	0.003	0.040

Table 8: Repeatability results for linear motion testing at 10,000 rpm

		Camera		Optical Tracker		Digital Caliper
Trial #	Commanded position (mm)	Position (mm)	Error (mm)	Position (mm)	Error (mm)	Error (mm)
1	50	49.929	0.071	49.435	0.565	0.050
2	50	49.929	0.071	49.454	0.546	0.010
3	50	49.929	0.071	49.443	0.557	0.060
4	50	49.929	0.071	49.446	0.554	0.080
5	50	49.929	0.071	49.452	0.548	0.010
6	50	50.000	0.000	49.460	0.540	0.040
7	50	49.929	0.071	49.458	0.542	0.060
8	50	49.929	0.071	49.456	0.544	0.050
9	50	49.929	0.071	49.452	0.548	0.010
10	50	50.071	0.071	49.459	0.541	0.060
11	60	59.714	0.286	59.622	0.378	0.040
12	60	59.786	0.214	59.624	0.376	0.030
13	60	59.786	0.214	59.628	0.372	0.060
14	60	59.714	0.286	59.630	0.370	0.080
15	60	59.714	0.286	59.620	0.380	0.020
16	60	59.714	0.286	59.630	0.370	0.000
17	60	59.786	0.214	59.622	0.378	0.060
18	60	59.714	0.286	59.622	0.378	0.040
19	60	59.714	0.286	59.622	0.378	0.030
20	60	59.714	0.286	59.635	0.365	0.020

Table 9: Repeatability results for linear motion testing at 7,500 rpm

		Camera		Optical Tracker		Digital Caliper
Trial #	Commanded position (mm)	Position (mm)	Error (mm)	Position (mm)	Error (mm)	Error (mm)
1	50	50.000	0.000	49.482	0.518	0.080
2	50	49.929	0.071	49.496	0.504	0.060
3	50	49.929	0.071	49.496	0.504	0.020
4	50	49.929	0.071	49.488	0.512	0.050
5	50	49.929	0.071	49.494	0.506	0.050
6	50	50.071	0.071	49.490	0.510	0.040
7	50	49.929	0.071	49.490	0.510	0.000
8	50	49.929	0.071	49.501	0.499	0.050
9	50	49.929	0.071	49.508	0.492	0.070
10	50	49.929	0.071	49.491	0.509	0.040
11	60	59.786	0.214	59.625	0.375	0.060
12	60	59.714	0.286	59.615	0.385	0.050
13	60	59.786	0.214	59.618	0.382	0.030
14	60	59.786	0.214	59.612	0.388	0.060
15	60	59.714	0.286	59.611	0.389	0.030
16	60	59.714	0.286	59.621	0.379	0.000
17	60	59.714	0.286	59.619	0.381	0.000
18	60	59.786	0.214	59.608	0.392	0.010
19	60	59.714	0.286	59.623	0.377	0.030
20	60	59.786	0.214	59.615	0.385	0.070

Table 10: Repeatability results for linear motion testing at 2,500 rpm

		Camera		Optical Tracker		Digital Caliper
Trial #	Commanded position (mm)	Position (mm)	Error (mm)	Position (mm)	Error (mm)	Error (mm)
1	60	59.786	0.214	59.615	0.385	0.080
2	60	59.714	0.286	59.625	0.375	0.050
3	60	59.714	0.286	59.625	0.375	0.030
4	60	59.786	0.214	59.616	0.384	0.060
5	60	59.714	0.286	59.603	0.397	0.060
6	60	59.786	0.214	59.618	0.382	0.000
7	60	59.714	0.286	59.618	0.382	0.030
8	60	59.714	0.286	59.618	0.382	0.040
9	60	59.714	0.286	59.618	0.382	0.040
10	60	59.786	0.214	59.624	0.376	0.040
11	50	49.857	0.143	49.503	0.497	0.060
12	50	49.929	0.071	49.490	0.510	0.020
13	50	49.929	0.071	49.486	0.514	0.040
14	50	49.929	0.071	49.490	0.510	0.030
15	50	49.929	0.071	49.477	0.523	0.040
16	50	49.929	0.071	49.492	0.508	0.070
17	50	50.000	0.000	49.496	0.504	0.040
18	50	49.929	0.071	49.484	0.516	0.010
19	50	49.929	0.071	49.475	0.525	0.050
20	50	50.000	0.000	49.480	0.520	0.030

References

Abolhassani, N., Patel, R., & Moallem, M. (2007). Needle insertion into soft tissue: A survey. *Medical Engineering & Physics, 29*(4), 413-431.

Abrahams, M., Aziz, M., Fu, R., & Horn, J.-L. (2009). Ultrasound guidance compared with electrical neurostimulation for peripheral nerve block: a systematic review and meta-analysis of randomized controlled trials. *Br J Anaesth, 102*(3), 408-417.

Badaan, S., Petrisor, D., Kim, C., Mozer, P., Mazilu, D., Gruionu, L., . . . Stoianovici, D. (2011). Does needle rotation improve lesion targeting? *The International Journal of Medical Robotics and Computer Assisted Surgery, 7*(2), 138-147.

Barrington, M. J., Wong, D. M., Slater, B., Ivanusic, J. J., & Ovens, M. (2012). Ultrasound-guided regional anesthesia: how much practice do novices require before achieving competency in ultrasound needle visualization using a cadaver model. *Reg Anesth Pain Med, 37*(3), 334-339. doi: 10.1097/AAP.0b013e3182475fba

Bassan, H. S., Patel, R. V., & Moallem, M. (2009). A novel manipulator for percutaneous needle insertion: Design and experimentation. *Mechatronics, IEEE/ASME Transactions on, 14*(6), 746-761.

Bergeles, C., Qin, L., Vartholomeos, P., & Dupont, P. E. (2012). Tracking and position control of an MRI-powered needle-insertion robot. *Conf Proc IEEE Eng Med Biol Soc, 2012*, 928-931.

Boctor, E. M., Webster III, R. J., Mathieu, H., Okamura, A. M., & Fichtinger, G. (2004). Virtual remote center of motion control for needle placement robots. *Computer Aided Surgery, 9*(5), 175-183.

Brewer, R. D., & Salisbury, J. K. (2010, 3-7 May 2010). *Visual vein-finding for robotic IV insertion.* Paper presented at the Robotics and Automation (ICRA), 2010 IEEE International Conference on.

Brinkman, W. M., Luursema, J. M., Kengen, B., Schout, B. M., Witjes, J. A., & Bekkers, R. L. (2013). da Vinci Skills Simulator for Assessing Learning Curve and Criterion-based Training of Robotic Basic Skills. *Urology*. doi: 10.1016/j.urology.2012.10.020

Burdette, E. C., Rucker, D. C., Prakash, P., Diederich, C. J., Croom, J. M., Clarke, C., . . . Webster III, R. J. (2010). *The ACUSITT ultrasonic ablator: the first steerable needle with an integrated interventional tool.* Paper presented at the Proc SPIE.

Bzostek, A., Schreiner, S., Barnes, A., Cadeddu, J., Roberts, W., Anderson, J., . . . Kavoussi, L. (1997). An automated system for precise percutaneous access of the renal collecting system. In J. Troccaz, E. Grimson & R. Mösges (Eds.), *CVRMed-MRCAS'97* (Vol. 1205, pp. 299-308): Springer Berlin Heidelberg.

Carabuena, J. M. (2013). The Learning Curve Associated with the Epidural Technique Using the EpisureTM AutoDetectTM Versus Conventional Glass Syringe: An Open-Label, Randomized, Controlled, Crossover Trial of Experienced Anesthesiologists in Obstetric Patients. *Anesthesia & Analgesia, 116*(1), 145-154.

Cleary, K., Watson, V., Lindisch, D., Taylor, R. H., Fichtinger, G., Xu, S., . . . Stoianovici, D. (2005). Precision placement of instruments for minimally invasive procedures using a “needle driver” robot. *The International Journal of Medical Robotics and Computer Assisted Surgery, 1*(2), 40-47.

Corral, G., Ibáñez, L., Nguyen, C., Stoianovici, D., Navab, N., & Cleary, K. R. (2004). Robot control by fluoroscopic guidance for minimally invasive spine procedures. *International Congress Series, 1268*, 509-514.

De Lorenzo, D., Koseki, Y., De Momi, E., Chinzei, K., & Okamura, A. M. (2013). Coaxial needle insertion assistant with enhanced force feedback. *IEEE Trans Biomed Eng, 60*(2), 379-389.

de Oliveira Filho, G. R. (2002). The construction of learning curves for basic skills in anesthetic procedures: an application for the cumulative sum method. *Anesth Analg, 95*(2), 411-416, table of contents.

de Oliveira Filho, G. R., Helayel, P. E., da Conceicao, D. B., Garzel, I. S., Pavei, P., & Ceccon, M. S. (2008). Learning curves and mathematical models for interventional ultrasound basic skills. *Anesth Analg, 106*(2), 568-573, table of contents. doi: 10.1213/ane.0b013e3181605412

Fichtinger, G., DeWeese, T. L., Patriciu, A., Tanacs, A., Mazilu, D., Anderson, J. H., . . . Stoianovici, D. (2002). System for Robotically Assisted Prostate Biopsy and Therapy with Intraoperative CT Guidance. *Academic Radiology, 9*(1), 60-74.

Fichtinger, G., Fiene, J. P., Kennedy, C. W., Kronreif, G., Iordachita, I., Song, D. Y., . . . Kazanzides, P. (2008). Robotic assistance for ultrasound-guided prostate brachytherapy. *Medical Image Analysis, 12*(5), 535-545.

Fischer, G. S., Iordachita, I., Csoma, C., Tokuda, J., DiMaio, S. P., Tempany, C. M., . . . Fichtinger, G. (2008). MRI-Compatible Pneumatic Robot for Transperineal Prostate Needle Placement. *Mechatronics, IEEE/ASME Transactions on, 13*(3), 295-305.

Fujii, M., Sugita, N., Ishimaru, T., Iwanaka, T., & Mitsuishi, M. (2013). A novel approach to the design of a needle driver with multiple DOFs for pediatric laparoscopic surgery. *Minimally Invasive Therapy & Allied Technologies, 22*(1), 9-16.

Gerard, I., & Collins, D. (2014). An analysis of tracking error in image guided neurosurgery. *International Journal of Computer Assisted Radiology and Surgery, 9*, (Suppl1):S93-S101.

Goffin, L., Gaetan, B., Martel, F., Nicolau, S., Gangloff, J., Egly, J., & Bayle, B. (2013). Design and in vivo evaluation of a robotized needle insertion system for small animals. *IEEE Trans Biomed Eng, 60*(8), 2193-2204.

Hanly, E. J., Marohn, M. R., Bachman, S. L., Talamini, M. A., Hacker, S. O., Howard, R. S., & Schenkman, N. S. (2004). Multiservice laparoscopic surgical training using the daVinci surgical system. *Am J Surg, 187*(2), 309-315. doi: 10.1016/j.amjsurg.2003.11.021

Hashizume, M., Yasunaga, T., Tanoue, K., Ieiri, S., Konishi, K., Kishi, K., . . . Fujie, M. (2008). New real-time MR image-guided surgical robotic system for minimally invasive precision surgery. *International Journal of Computer Assisted Radiology and Surgery, 2*(6), 317-325.

Heemskerk, J., van Gemert, W. G., de Vries, J., Greve, J., & Bouvy, N. D. (2007). Learning curves of robot-assisted laparoscopic surgery compared with conventional laparoscopic surgery: an experimental study evaluating skill

acquisition of robot-assisted laparoscopic tasks compared with conventional laparoscopic tasks in inexperienced users. *Surg Laparosc Endosc Percutan Tech, 17*(3), 171-174. doi: 10.1097/SLE.0b013e31805b8346

Hemmerling, T. M., Taddei, R., Wehbe, M., Cyr, S., Zaouter, C., & Morse, J. (2013). First Robotic Ultrasound-Guided Nerve Blocks in Humans Using the Magellan System. *Anesth Analg*. doi: 10.1213/ANE.0b013e3182713b49

Hemmerling, T. M., Taddei, R., Wehbe, M., Zaouter, C., Cyr, S., & Morse, J. (2012). First robotic tracheal intubations in humans using the Kepler intubation system. *Br J Anaesth, 108*(6), 1011-1016. doi: 10.1093/bja/aes034

Hemmerling, T. M., Wehbe, M., Zaouter, C., Taddei, R., & Morse, J. (2012). The Kepler intubation system. *Anesth Analg, 114*(3), 590-594. doi: 10.1213/ANE.0b013e3182410cbf

Hempel, E., Fischer, H., Gumb, L., Höhn, T., Krause, H., Voges, U., . . . Bock, M. (2003). An MRI-compatible surgical robot for precise radiological interventions. *Computer Aided Surgery, 8*(4), 180-191.

Hong, J., Dohi, T., Hashizume, M., Konishi, K., & Hata, N. (2004). An ultrasound-driven needle-insertion robot for percutaneous cholecystostomy. *Physics in Medicine and Biology, 49*(3), 441.

Ishimaru, T., Takazawa, S., Uchida, H., Kawashima, H., Fujii, M., Harada, K., . . . Iwanaka, T. (2013). Development of a Needle Driver with Multiple Degrees of Freedom for Neonatal Laparoscopic Surgery. *J Laparoendosc Adv Surg Tech A, 23*(7), 644-648.

Jienan, D., Dan, S., Petrisor, D., Mozer, P., Avila, R., Ibanez, L., . . . Cleary, K. (2008, 8-10 Oct. 2008). *Medical needle steering for lung biopsy: Experimental results in tissue phantoms using a robotic needle driver.* Paper presented at the BioInformatics and BioEngineering, 2008. BIBE 2008. 8th IEEE International Conference on.

Jimenez-Rodriguez, R. M., Diaz-Pavon, J. M., de la Portilla de Juan, F., Prendes-Sillero, E., Dussort, H. C., & Padillo, J. (2012). Learning curve for robotic-

assisted laparoscopic rectal cancer surgery. *Int J Colorectal Dis*. doi: 10.1007/s00384-012-1620-6

Ju, H., Zhang, J., An, G., Pei, X., & Xing, G. (2008). *A robot-assisted system for minimally invasive spine surgery of percutaneous vertebroplasty based on CT images.* Paper presented at the Robotics, Automation and Mechatronics, 2008 IEEE Conference on.

Kaul, S., Shah, N. L., & Menon, M. (2006). Learning curve using robotic surgery. *Curr Urol Rep, 7*(2), 125-129.

Kettenbach, J., Kronreif, G., Figl, M., Fürst, M., Birkfellner, W., Hanel, R., & Bergmann, H. (2005). Robot-assisted biopsy using ultrasound guidance: initial results from in vitro tests. *European radiology, 15*(4), 765-771.

Kobayashi, Y., Hamano, R., Watanabe, H., Hong, J., Toyoda, K., Hashizume, M., & Fujie, M. G. (2013). Use of puncture force measurement to investigate the conditions of blood vessel needle insertion. *Medical Engineering & Physics, 35*(5), 684-689.

Kobayashi, Y., Hong, J., Hamano, R., Okada, K., Fujie, M. G., & Hashizume, M. (2012). Development of a needle insertion manipulator for central venous catheterization. *Int J Med Robot, 8*(1), 34-44.

Kobayashi, Y., Onishi, A., Watanabe, H., Hoshi, T., Kawamura, K., Hashizume, M., & Fujie, M. G. (2010). Development of an integrated needle insertion system with image guidance and deformation simulation. *Computerized Medical Imaging and Graphics, 34*(1), 9-18.

Kokes, R., Lister, K., Gullapalli, R., Zhang, B., MacMillan, A., Richard, H., & Desai, J. P. (2009). Towards a teleoperated needle driver robot with haptic feedback for RFA of breast tumors under continuous MRI. *Medical Image Analysis, 13*(3), 445-455.

Kratchman, L. B., Rahman, M. M., Saunders, J. R., Swaney, P. J., & Webster III, R. J. (2011). *Toward robotic needle steering in lung biopsy: A tendon-actuated approach.* Paper presented at the Proc. of SPIE.

Krieger, A., Susil, R. C., Ménard, C., Coleman, J. A., Fichtinger, G., Atalar, E., & Whitcomb, L. L. (2005). Design of a novel MRI compatible manipulator for image

guided prostate interventions. *Biomedical Engineering, IEEE Transactions on, 52*(2), 306-313.

Kwoh, Y. S., Hou, J., Jonckheere, E. A., & Hayati, S. (1988). A robot with improved absolute positioning accuracy for CT guided stereotactic brain surgery. *Biomedical Engineering, IEEE Transactions on, 35*(2), 153-160.

Lau, S., Vaknin, Z., Ramana-Kumar, A. V., Halliday, D., Franco, E. L., & Gotlieb, W. H. (2012). Outcomes and cost comparisons after introducing a robotics program for endometrial cancer surgery. *Obstet Gynecol, 119*(4), 717-724. doi: 10.1097/AOG.0b013e31824c0956

Loser, M., & Navab, N. (2000). A New Robotic System for Visually Controlled Percutaneous Interventions under CT Fluoroscopy. In S. Delp, A. DiGoia & B. Jaramaz (Eds.), *Medical Image Computing and Computer-Assisted Intervention – MICCAI 2000* (Vol. 1935, pp. 887-896): Springer Berlin Heidelberg.

Masamune, K., Fichtinger, G., Patriciu, A., Susil, R. C., Taylor, R. H., Kavoussi, L. R., . . . Stoianovici, D. (2001). System for robotically assisted percutaneous procedures with computed tomography guidance. *Comput Aided Surg, 6*(6), 370-383.

Masamune, K., Kobayashi, E., Masutani, Y., Suzuki, M., Dohi, T., Iseki, H., & Takakura, K. (1995). Development of an MRI-compatible needle insertion manipulator for stereotactic neurosurgery. *Computer Aided Surgery, 1*(4), 242-248.

Maurin, B., Piccin, O., Bayle, B., Gangloff, J., de Mathelin, M., Soler, L., & Gangi, A. (2004). A new robotic system for CT-guided percutaneous procedures with haptic feedback. *International Congress Series, 1268*(0), 515-520.

Melzer, A., Gutmann, B., Remmele, T., Wolf, R., Lukoscheck, A., Bock, M., . . . Fischer, H. (2008). Innomotion for percutaneous image-guided interventions. *Engineering in Medicine and Biology Magazine, IEEE, 27*(3), 66-73.

Menon, M., Tewari, A., Baize, B., Guillonneau, B., & Vallancien, G. (2002). Prospective comparison of radical retropubic prostatectomy and robot-assisted anatomic prostatectomy: the Vattikuti Urology Institute experience. *Urology, 60*(5), 864-868.

Moran, M. E. (2003). Robotic surgery: urologic implications. *J Endourol, 17*(9), 695-708. doi: 10.1089/089277903770802209

Morse, J., Terrasini, N., Wehbe, M., Philippona, C., Zaouter, C., Cyr, S., & Hemmerling, T. (2014). Comparison of success rates, learning curves, and inter-subject performance variability of robot-assisted and manual ultrasound-guided nerve block needle guidance in simulation. *Br J Anaesth*, aet440.

Morse, J., Wehbe, M., Taddei, R., Cyr, S., & Hemmerling, T. M. (2013). Magellan: Technical Description of a New System for Robot-Assisted Nerve Blocks. *Journal of Computers, In press*.

Muntener, M., Patriciu, A., Petrisor, D., Mazilu, D., Bagga, H., Kavoussi, L., . . . Stoianovici, D. (2006). Magnetic resonance imaging compatible robotic system for fully automated brachytherapy seed placement. *Urology, 68*(6), 1313-1317.

Ohtsuka, T., Ninomiya, M., Nonaka, T., & Maemura, T. (2004). A new needle driver for minientry coronary artery bypass. *Heart Surg Forum, 7*(6), E559-561.

Okamura, A. M., Simone, C., & O'Leary, M. D. (2004). Force modeling for needle insertion into soft tissue. *Biomedical Engineering, IEEE Transactions on, 51*(10), 1707-1716.

Onogi, S., Gotoh, M., Nakajima, Y., Koyama, T., Tamura, Y., Kobayashi, E., . . . Yonenobu, K. (2009). Vertebral robotic puncture for minimally invasive spinal surgery: puncture accuracy evaluation for vertebral model. *Int J Comput Assist Radiol Surg, 4*(suppl 1), 121-122.

Onogi, S., Morimoto, K., Sakuma, I., Nakajima, Y., Koyama, T., Sugano, N., . . . Momoi, Y. (2005). Development of the needle insertion robot for percutaneous vertebroplasty *Medical Image Computing and Computer-Assisted Intervention–MICCAI 2005* (pp. 105-113): Springer.

Patriciu, A., Petrisor, D., Muntener, M., Mazilu, D., Schar, M., & Stoianovici, D. (2007). Automatic Brachytherapy Seed Placement Under MRI Guidance. *Biomedical Engineering, IEEE Transactions on, 54*(8), 1499-1506.

Ramani, A. P., Braasch, M., Botnaru, A., Lavers, A., Herrera, S., Nardi Pedro, R., & Monga, M. (2008). Evaluation of efficacy of four laparoscopic needle drivers. *Jsls, 12*(1), 77-80.

Ramsay, C., Pickard, R., Robertson, C., Close, A., Vale, L., Armstrong, N., . . . Soomro, N. (2012). Systematic review and economic modelling of the relative clinical benefit and cost-effectiveness of laparoscopic surgery and robotic surgery for removal of the prostate in men with localised prostate cancer. *Health Technol Assess, 16*(41), 1-313. doi: 10.3310/hta16410

Rashid, T. G., Kini, M., & Ind, T. E. (2010). Comparing the learning curve for robotically assisted and straight stick laparoscopic procedures in surgical novices. *Int J Med Robot, 6*(3), 306-310. doi: 10.1002/rcs.333

Renda, A., & Vallancien, G. (2003). Principles and advantages of robotics in urologic surgery. *Curr Urol Rep, 4*(2), 114-118.

Robotic-assisted minimally invasive surgery for gynecologic and urologic oncology: an evidence-based analysis. (2010). *Ont Health Technol Assess Ser, 10*(27), 1-118.

Schreiner, S., Anderson, J. H., Taylor, R. H., Funda, J., Bzostek, A., & Barnes, A. C. (1997). A system for percutaneous delivery of treatment with a fluoroscopically-guided robot. In J. Troccaz, E. Grimson & R. Mösges (Eds.), *CVRMed-MRCAS'97* (Vol. 1205, pp. 747-756): Springer Berlin Heidelberg.

Shah, S., Kapoor, A., Ding, J., Guion, P., Petrisor, D., Karanian, J., . . . Cleary, K. (2008). Robotically assisted needle driver: evaluation of safety release, force profiles, and needle spin in a swine abdominal model. *International Journal of Computer Assisted Radiology and Surgery, 3*(1-2), 173-179.

Sites, B. D., Spence, B. C., Gallagher, J. D., Wiley, C. W., Bertrand, M. L., & Blike, G. T. (2007). Characterizing novice behavior associated with learning ultrasound-guided peripheral regional anesthesia. *Reg Anesth Pain Med, 32*(2), 107-115. doi: 10.1016/j.rapm.2006.11.006

Sites, B. D., Spence, B. C., Gallagher, J. D., Wiley, C. W., Bertrand, M. L., & Blike, G. T. (2007). Characterizing novice behavior associated with learning ultrasound-

guided peripheral regional anesthesia. *Regional anesthesia and pain medicine, 32*(2), 107-115.

Stoianovici, D. (2001). URobotics—Urology Robotics at Johns Hopkins. *Computer Aided Surgery, 6*(6), 360-369.

Stoianovici, D., Cadeddu, J., Demaree, R., Basile, H., Taylor, R., Whitcomb, L., & Kavoussi, L. (1997). *A novel mechanical transmission applied to percutaneous renal access.* Paper presented at the ASME Dynamic Systems and Control Division.

Stoianovici, D., Cadeddu, J., Demaree, R., Basile, S., Taylor, R., Whitcomb, L., . . . Kavoussi, L. (1997). An efficient needle injection technique and radiological guidance method for percutaneous procedures. In J. Troccaz, E. Grimson & R. Mösges (Eds.), *CVRMed-MRCAS'97* (Vol. 1205, pp. 295-298): Springer Berlin Heidelberg.

Stoianovici, D., Cleary, K., Patriciu, A., Mazilu, D., Stanimir, A., Craciunoiu, N., . . . Kavoussi, L. (2003). AcuBot: a robot for radiological interventions. *Robotics and Automation, IEEE Transactions on, 19*(5), 927-930.

Stoianovici, D., Song, D., Petrisor, D., Ursu, D., Mazilu, D., Mutener, M., . . . Patriciu, A. (2007). “MRI Stealth” robot for prostate interventions. *Minimally Invasive Therapy & Allied Technologies, 16*(4), 241-248.

Stoianovici, D., Whitcomb, L., Anderson, J., Taylor, R., & Kavoussi, L. (1998). A modular surgical robotic system for image guided percutaneous procedures. In W. Wells, A. Colchester & S. Delp (Eds.), *Medical Image Computing and Computer-Assisted Interventation — MICCAI’98* (Vol. 1496, pp. 404-410): Springer Berlin Heidelberg.

Sun, D., Willingham, C., Durrani, A., King, P., Cleary, K., & Wood, B. (2006). A novel end-effector design for robotics in image-guided needle procedures. *The international journal of medical robotics + computer assisted surgery : MRCAS, 2*(1), 91-97.

Sviggum, H. P., Ahn, K., Dilger, J. A., & Smith, H. M. (2013). Needle Echogenicity in Sonographically Guided Regional Anesthesia Blinded Comparison of 4

Enhanced Needles and Validation of Visual Criteria for Evaluation. *Journal of Ultrasound in Medicine, 32*(1), 143-148.

Taylor, R. H., Funda, J., Eldridge, B., Gomory, S., Gruben, K., LaRose, D., . . . Anderson, J. (1995). A telerobotic assistant for laparoscopic surgery. *Engineering in Medicine and Biology Magazine, IEEE, 14*(3), 279-288.

Terayama, M., Furusho, J., & Monden, M. (2007). Curved multi-tube device for path-error correction in a needle-insertion system. *The International Journal of Medical Robotics and Computer Assisted Surgery, 3*(2), 125-134.

Tighe, P. J., Badiyan, S. J., Luria, I., Boezaart, A. P., & Parekattil, S. (2010). Technical communication: robot-assisted regional anesthesia: a simulated demonstration. *Anesth Analg, 111*(3), 813-816. doi: 10.1213/ANE.0b013e3181e66386

Tighe, P. J., Badiyan, S. J., Luria, I., Lampotang, S., & Parekattil, S. (2010). Robot-assisted airway support: a simulated case. *Anesth Analg, 111*(4), 929-931. doi: 10.1213/ANE.0b013e3181ef73ec

Tomaszewski, J. J., Matchett, J. C., Davies, B. J., Jackman, S. V., Hrebinko, R. L., & Nelson, J. B. (2012). Comparative hospital cost-analysis of open and robotic-assisted radical prostatectomy. *Urology, 80*(1), 126-129. doi: 10.1016/j.urology.2012.03.020

Tovar-Arriaga, S., Tita, R., Pedraza-Ortega, J. C., Gorrostieta, E., & Kalender, W. A. (2011). Development of a robotic FD-CT-guided navigation system for needle placement—preliminary accuracy tests. *The International Journal of Medical Robotics and Computer Assisted Surgery, 7*(2), 225-236.

Vartholomeos, P., Qin, L., & Dupont, P. E. (2011). *MRI-powered actuators for robotic interventions.* Paper presented at the Intelligent Robots and Systems (IROS), 2011 IEEE/RSJ International Conference on.

Voss, W. (2007). *A Comprehensible Guide to Servo Motor Sizing*. Greenfield, MA: Copperhill Media Corporation.

Walsh, C. J., Franklin, J., Slocum, A. H., & Gupta, R. (2011, Aug. 30 2011-Sept. 3 2011). *Design of a robotic tool for percutaneous instrument distal tip*

repositioning. Paper presented at the Engineering in Medicine and Biology Society,EMBC, 2011 Annual International Conference of the IEEE.

Waspe, A. C., Cakiroglu, H. J., Lacefield, J. C., & Fenster, A. (2006, Aug. 30 2006-Sept. 3 2006). *Design and Validation of a Robotic Needle Positioning System for Small Animal Imaging Applications.* Paper presented at the Engineering in Medicine and Biology Society, 2006. EMBS '06. 28th Annual International Conference of the IEEE.

Willis, D. L., Gonzalgo, M. L., Brotzman, M., Feng, Z., Trock, B., & Su, L. M. (2012). Comparison of outcomes between pure laparoscopic vs robot-assisted laparoscopic radical prostatectomy: a study of comparative effectiveness based upon validated quality of life outcomes. *BJU Int, 109*(6), 898-905. doi: 10.1111/j.1464-410X.2011.10551.x

Yang, B., Tan, U. X., McMillan, A., Gullapalli, R., & Desai, J. P. (2011). Design and Control of a 1-DOF MRI Compatible Pneumatically Actuated Robot with Long Transmission Lines. *IEEE ASME Trans Mechatron, 16*(6), 1040-1048.

Yanof, J., Haaga, J., Klahr, P., Bauer, C., Nakamoto, D., Chaturvedi, A., & Bruce, R. (2001). CT-integrated robot for interventional procedures: Preliminary experiment and computer–human interfaces. *Computer Aided Surgery, 6*(6), 352-359.

Zaky, S., Guirguis, M., & Nickels, T. (2013). Regional Anesthesia Techniques. *Perioperative Pain Management*.